Noise and Vibrations Analysis of Electrical Machines

Issah Ibrahim

Department of Electrical & Computer Engineering
McGill University
Montreal, Canada

December 2021

A thesis submitted to McGill University in partial fulfillment of the requirements for the degree of Doctor of Philosophy.

Abstract

Today's electrical machines are finding many applications in new environments where lower noise levels are demanded, especially in electric vehicles. It is, therefore, imperative that the designs must satisfy certain acoustic noise requirements.

In the past, experimental electric motors were developed in the early design process to assess their noise performance before full scale production. This approach could be an unpleasant experience for motor designers, as the mitigation solutions often needed substantial modification to their prototype models. These prototypes can be very expensive, and forcing in engineering changes to an existing machine can be a nightmare. For this reason, the use of computer software in noise and vibrations analysis has attracted a lot of attention in recent years.

This thesis uses computer-aided predictive techniques such as the finite element method to set the background for the computational discussions and exploration of some of the research gaps in the literature. It focuses on the interior permanent magnet synchronous motor due to its extensive application, particularly in the automotive industry.

In this work, the effect of non-sinusoidal current waveforms on the acoustic noise field of the electric motor drive has been analyzed. It is discovered that sampling the airgap space at different instants yields inconsistent electromagnetic force results. Therefore, this thesis proposes an efficient way of extracting the electromagnetic forces in the airgap space to account for very critical harmonics that may be ignored in conventional techniques such as the single-time sampling. It also defines two new acoustic quantities to accurately estimate the resulting acoustic noise for different switching frequencies of the power electronic circuit.

Also, since the thermal behaviour of the electric motor is mostly linked to the losses that result from the current supply system, the analysis incorporates the role of temperature in defining the acoustic field of the electric motor by adding an extra model to the existing subsystem models in the noise calculation process. It reveals that elevating the operating temperature levels significantly exacerbates the acoustic noise problems of the machine. The thermal excitation modified the electromagnetic, the structural and the acoustic subsystem models.

Finally, the thesis addresses the computational burden associated with setting up multiphysics simulation frameworks for the assessment of acoustic noise. Here, surrogate models are introduced as possible replacements of the time-consuming finite element simulations.

Résumé

Les machines électriques d'aujourd'hui se trouvent dans de nouveaux environnements où les demandes exigent un niveau sonore abaissé, particulièrement dans les véhicules électriques. Il est donc impératif que les demandes sonores soient satisfaites pendant la conception.

Autrefois, les machines expérimentales étaient construites tôt dans le processus de développement pour évaluer leurs caractéristiques acoustiques. Ce processus pouvait être désagréable pour les concepteurs, car les modifications requises demandaient souvent des changements substantiels aux prototypes. Ces prototypes sont souvent dispendieux, et les changements faits sur une machine existante sont difficiles. Pour ces raisons, l'utilisation de logiciels d'analyses acoustique et des vibrations a attiré beaucoup d'attention au cours des dernières années.

Cette thèse utilise des outils assistés par ordinateur comme la méthode des éléments finis pour établir la fondation pour les discussions et explorations des lacunes de la littérature. Elle se concentre sur les moteurs synchrones à aimant permanent intérieur dû à leur variété d'utilisations, particulièrement dans le secteur automobile.

Dans ce travail, l'effet de formes d'onde de courant non sinusoïdale sur le champ de bruit acoustique des moteurs était analysé. Il était découvert qu'en échantillonnant l'entrefer à des moments différents retourne des forces électromagnétiques incohérents. Cette thèse propose donc une manière efficace d'extraire les forces électromagnétiques dans l'entrefer qui prend en compte les harmoniques critiques que les méthodes traditionnelles, comme l'échantillonnage à temps unique, pourraient manquer. Elle défini aussi deux nouvelles quantités acoustiques pour estimer avec précision le bruit résultant de divers fréquences de commutation dans les électroniques de puissance.

De plus, parce que le comportement thermique d'un moteur électrique est lié aux pertes résultant de la système d'alimentation de courant, l'analyse inclut le rôle de la température en définissant le champ de bruit du moteur en ajoutant un modèle supplémentaire aux modèles de sous-systèmes existants dans le processus de calcul acoustique. Il est révélé que de monter la température d'opération considérablement vient exacerber les problèmes acoustiques de la machine. Les changements thermiques ont modifié les modèles de sous-systèmes électromagnétiques, structurels, et acoustiques.

Finalement, la thèse vient adresser la charge de calcul associée avec l'initialisation du cadre pour la simulation multi-physique du champ de bruit. Ici, les modèles de substitution

sont introduits comme remplaçants possibles des calculs chronophages comme la méthode des éléments finis.

Dedication

All I ever wanted in this life was to make my grandmother very happy and proud. That is all I ever wished for! So, today I dedicate my highest academic accomplishment, my doctoral thesis, to Hajia Bintu Seidu (AD 1926—2011) of blessed memory.

Rest in peace, Hajia Bintu! I made it!

Acknowledgments

I wish to express my utmost gratitude to my research advisor, Prof. David A. Lowther, who does the work of ten men, yet, enjoys every bit of it. His passion for ideas, his formidable knowledge and his balance between academic life and everything else has been inspirational. He has been my bastion, mentor and guardian through this epoch-making journey. It would not have been possible without him. Thank you DAL!

I would like to acknowledge my colleagues: Mr. Arbaaz Khan, Dr. Vahid Ghorbanian, Dr. M. H. Mohammadi and Dr. Rodrigo Pedrosa, an Assistant Professor in the Computer Science department at the Federal University of Ouro Preto in Brazil. Their immense support, insightful ideas, perspectives and artful encouragement have brought me to this watershed moment of my life.

The following people deserve thanks for agreeing to be part of the thesis defense committee: Prof. François Boufard, Prof. M. Kokkolaras, and Prof. Dennis Giannacopoulos, all at the Electrical and Computer Engineering department, not forgetting Prof. Odile Liboiron-Ladouceur who chaired the defense, and the Pro-Dean, Prof. Pierre Lachapelle. Their painstaking review of my work, their comments, their criticisms and their suggestions were very useful in the final redaction of this thesis.

I would also like to offer my special thanks to the non-teaching staff at the ECE department, especially Melanie Gorman, secretary extraordinaire, for preparing most of the paper works.

Finally, I am forever indebted to my family and numerous friends in the diaspora, whose contribution, in any shape or form, have brought my doctoral experience to an expected end, and those outside who refreshingly have no idea what this thesis is all about.

We are like dwarfs astride the shoulders of giants. We see more, and things that are more distant, than they did, not because our sight is superior or because we are taller than they, but because they raise us up, and by their great stature add to ours.

Bernard of Chartres, 1130 AD

Contents

List of Figures

List of Tables

List of Acronyms

1D, 2D, 3D	One, Two, Three Dimensional
EPA	Environmental Protection Agency
NIDCD	National Institute on Deafness and Other Communication Disorders
NIHL	Noise-Induced Hearing Loss
TTS	Temporary threshold shift
PTS	Permanent threshold shift
WHO	World Health Organization
PEL	Permissible Exposure Limit
I-INCE	International Institute of Noise Control Engineering
EC	Engineering control
ISO	International Organization for Standardization
IEC	International Electrotechnical Commission
NIOSH	National Institute for Occupational Safety and Health
NASA	National Aeronautics and Space Administration
OSHA	Occupational Safety and Health Administration
MSHA	Mine Safety and Health Administration
emf	Electromotive force
IM	Induction machine
IPMSM	Interior permanent magnet synchronous machine
NVH	Noise, Vibration, and Harshness
GCD	Greatest Common Divisor
BEM	Boundary-element method
FEM	Finite element method
FDM	Finite difference method

FEA	Finite element analysis
CAE	Computer-aided engineering
CAD	Computer-aided design
GUI	Graphic user interface
EM	Electromagnetic
FFT	Fast fourier transformation
FR	Frequency response
DFR	Direct frequency response
MFR	Modal frequency response
AML	Automatically Matched Layer
AFPM	Axial-flux permanent magnet
SPM	Surface-mounted permanent magnet
DPMSM	Disk permanent magnet synchronous machine
PMDC	Permanent magnet DC
SRM	Switched reluctance motor
PWM	Pulse-width modulation
CEMLab	Computational Electromagnetics Research Laboratory
NEMA	National Electrical Manufacturers Association
DoE	Design of experiment
LHS	Latin hypercube sampling
TDMP	Temperature-dependent material properties
MPO	Multi-physics performance objective
MTPA	Maximum torque per ampere
MTPV	Maximum torque per volts
FW	Flux-weakening
IQR	Inter-quartile range
MTS	Multiple-time sampling
THD	Total harmonic distortion
DOP	Design and optimization problem
SM	Surrogate model
MEC	Magnetic Equivalent Circuit
GSM	Global surrogate model
LSM	Local surrogate model

EMS	Electromagnetic subsystem
STS	Structural subsystem
ACS	Acoustic subsystem
MSE	Mean Squared Error
RMSE	Root Mean Squared Error
MAE	Mean Absolute Error
MAPE	Mean Absolute Percentual Error
MAX	Maximum Absolute Error
TT	SM training time
L_1	Standard linear regression model
L_2	Interactions linear regression model
L_3	Robust linear regression model
L_4	Stepwise linear regression model
T_1	Fine tree regression model
T_2	Medium tree regression model
T_3	Coarse tree regression model
SMV_1	Linear support vector machine
SMV_2	Quadratic support vector machine
SMV_3	Cubic support vector machine
SMV_4	Fine gaussian support vector machine
SMV_5	Medium gaussian support vector machine
SMV_6	Coarse support vector machine
GP_1	Squared exponential gaussian process regression model
GP_2	Matern 5/4 gaussian process regression model
GP_3	Exponential gaussian process regression model
GP_4	Rational quadratic gaussian process regression model

List of Symbols

T	Period of vibration
f	Frequency of vibration
λ	Wavelength of vibration
c	Speed of sound wave
dB	Decible: unit of sound wave
k_f	Coefficient dependent on the shape of fan blade
ρ	Density of a medium
v_{bl}	Circumferential speed of fan blade
D_{bl}	Diameter of fan blade wheel
B_r	Rotor magnetic flux density
B_s	Stator magnetic flux density
α	Angular distance from the origin of the coordinate system
v	Stator magnetic flux density space harmonic
μ	Rotor magnetic flux density space harmonic
p	Pole pairs
P_r	Radial magnetic force wave
r	Mode number or order or rank of the radial force wave
P_{mr}	Amplitude of the r^{th} order radial force wave
ω	Angular frequency
μ_0	Vacuum permeability constant
Z_s	Total number of stator slots
f_r	frequency of the r^{th} order radial force
f_p	Rotating frequency of the rotor
f_m	m^{th} modal frequency

E	Young's modulus
R_m	Mean stator radius
δ_m	Mass addition factor for displacement
F_nr	r^{th} Fourier series amplitude fo the radial force
f_sm	m^{th} mode of the stator natural vibrations
ζ_m	m^{th} harmonic damping factor
P_S	Sound power in Watts
n_p	Number of rotor poles
P_SL	Sound power level in dB
P_ref	Reference sound power in Watts
L_p	Sound pressure level in dB
$[M_\mathrm{s}]$	Stator mass matrix
$[B_\mathrm{s}]$	Stator damping matrix
$[K_\mathrm{s}]$	Stator stiffness matrix
$\{P_\mathrm{s}\}$	Forcing vector
$\{\dot{u}_\mathrm{s}\}$	Stator vibration
$\{\phi\}_\mathrm{i}$	i^th modeshape
F_n	Normal component of electromagnetic force
F_t	Tangential component of electromagnetic force
V_s	Supply voltage
I_s	Stator current vector
F	Magnetomotive force
ϕ_s	Stator flux
ϕ_r	Rotor flux
Γ_em	Electromagnetic torque
R_s	Winding resistance
f_sw	Switching frequency
σ	Standard deviation
R	Range of sound power level
I_d	d-axis current
I_q	q-axis current
L_d	d-axis inductance
L_q	q-axis inductance

γ	Current advance angle
λ_{s}	Stator flux linkage
λ_{d}	d-axis component of flux linkage
λ_{q}	q-axis component of flux linkage
λ_{s}	Stator flux linkage
λ_{m}	PM flux linkage
δ	Load angle
ξ	Saliency ratio
I_{ch}	Characteristic current
ω_{e}	Electrical frequency
m_{a}	Amplitude modulation index
m_{f}	Frequency modulation index
f_1	Fundamental frequency
B_{n}	Normal magnetic flux density
B_{t}	Normal magnetic flux density
$\mathrm{P}_{\mathrm{SL}}^{\mathrm{i}}$	Sound pressure level at i^{th} time instant
$\mathrm{P}_{\mathrm{SL}}^{\mathrm{avg}}$	Average sound pressure level
$\mathrm{P}_{\mathrm{SL}}^{\mathrm{rip}}$	Ripple sound pressure level
R_{r}	Real system response
R_{f}	Response produced by high-fidelity model
R_{sm}	Response produced by surrogate model
P	Number of input variables
R	Correlation matrix
N	Sample evaluation speed
R^2	Coefficient of Determination

Chapter 1

Introduction

1.1 Fundamentals of Vibration, Sound and Noise

Any body that has *elasticity* and *mass* can vibrate. According to Gieras et al. [3], vibration can be defined as a limited reciprocating motion of a particle of an elastic body in alternately opposite directions as a consequence of a forced or unforced disturbance from the body's equilibrium position. A plot of the vibrations against time can be a curve of considerable complication. But the reciprocating motion, in a general sense, is assumed to be periodic, i.e., a motion which repeats itself in all its particulars after a certain interval of time, called the *period* of the vibration. The harmonic motion of a simple pendulum is used as an illustration in Fig. 1.1. Here, the maximum value of the displacement x_0 is called the *amplitude* of the vibration. The period, designated by the symbol T, is measured in seconds; and its reciprocal is the frequency f of the vibration. The unit of frequency is *cycles per second*, although Hertz is popularly used in honor of the German Physicist Heinrich Rudolf Hertz. Thus, a 500 Hz waveform will have a period of 0.002s. The distance between consecutive corresponding points of the same phase on the waveform, such as two adjacent crests, or troughs, or zero crossings, is called a *wavelength*. A wavelength is often denoted by the symbol λ. The higher the frequency of the vibration, the shorter the wavelength and vice versa.

The mechanical vibrations of a body are interpreted as sound if the frequencies at which they occur fall in our audible range. The audible range describes the range of frequencies that can be heard by an organism. The generally accepted standard hearing range for human beings is from 20 Hz to 20 kHz, although there is considerable variation between

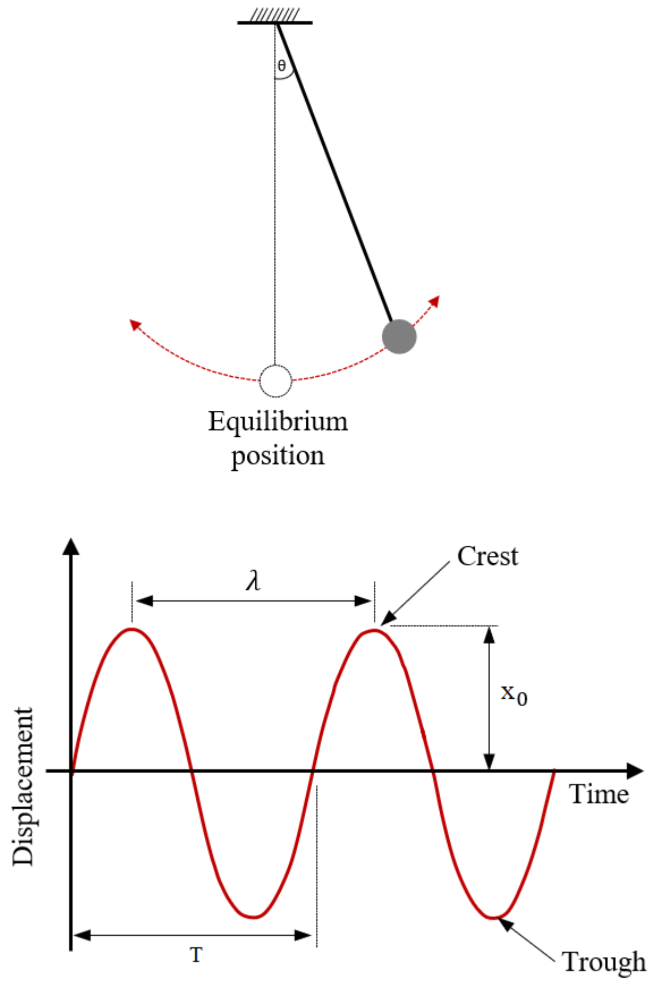

Fig. 1.1 The oscillations of a simple pendulum

individuals. The sensitivity of our ear varies significantly over this bandwidth, but it is hypersensitive between 1000 Hz and 5000 Hz [1]. As frequencies fall below 1 kHz and rise above 5 kHz, our hearing mechanism reduces or attenuates the sound level that we hear. Most of this text deals with audible sound waves, although in the broadest sense, the definition of sound includes both infrasound and *ultrasound* waves. Refer to Appendix A.1 for detailed explanation of the types of sound waves.

Sound travels through a medium with a finite speed. The speed depends on the elasticity and density of the propagating medium. Generally, sound travels fastest through solids and slowest through gases. For example, sound travels at 344 ms^{-1} in air; it travels at 1550

ms^{-1} in water (4.3 times faster than in air); and at 5120 ms^{-1} in iron (about 15 times faster than in air). In a vacuum, with an absence of matter, sound does not propagate. Other factors, such as the humidity levels or temperature, also influence the propagation speed of sound. Given the speed of a sound wave, we are able to calculate λ at a certain f by using the relation $\lambda = \frac{c}{f}$, where c is the speed of sound. Sound can also experience difficulties passing from one medium to another as each medium imposes a resistance called *impedance*, which can vary in strength. Therefore, a sound wave that propagates easily through air may be difficult to perceive in water, as the latter has a high impedance.

Sound is measured in *decibels*. The dB scale is a logarithmic scale that compares either the measured power, pressure or intensity of sound to the reference sound level. For mathematically inclined readers, note that the use of a logarithm was chosen to reflect how our sensitivity to changes in loudness varies with baseline intensity. This reveals something absolutely fundamental about the mammalian nervous system, and how it is designed to detect relative changes in the environment rather than absolute quantities [11].

Typically, when it comes to sound, the baseline quantity is the quietest vibration that the average normal-hearing adult can detect at 1 kHz, which historically was measured as being 20 μPa. This corresponds to 0 dB. This value, although it has been the subject of scientific debate, is still being referenced since it was first reported by Fletcher and Munson in 1933 [2]. Appendix A.2 gives a detailed explanation of decibels and sound level calculations.

From a Physics standpoint, there is no difference between noise and sound, as both are vibrations. The difference is in the perception of the listener. For example, rock music can be pleasurable sound to one person and an annoying noise to another. In either case, it can be hazardous to a person's hearing if the sound is loud and if they are exposed long and often enough. But the terms *noise* and *sound* can be used somewhat interchangeably, although we often ascribe a negative connotation to noise and consider it a little more unpleasant and disruptive to human hearing [12]. Hence, in its simplest definition, noise can be said to be an unwanted sound.

1.2 Effect of Noise Pollution on Public Health

Studies have shown that noise pollution is responsible for most of the world's health issues. Harmful levels of noise can affect the human body mainly in three different ways: physical, physiological and psychological. Physiological effects of noise pollution adversely affect health such as heightened blood pressure, fatigue and increased stress levels. Most industrial workers regularly exposed to high noise levels have higher cases of nausea, headaches, argumentativeness, changes in mood and anxiety, and insomnia. Also, many studies have shown that children with chronic exposure to noise have cognitive problems. Psychologically, noise can cause distractions, loss of concentration and annoyance which can be just as disruptive as physiological effects on the quality of life.

Physical effects of noise pollution are direct effects on a person's health such as hearing loss. Any reduction in the normal ability to hear is referred to as "hearing loss". Most experts agree that exposure to sound exceeding certain levels, e.g., more than 85 dB is potentially dangerous and can lead to Noise-Induced Hearing Loss (NIHL). To give the reader an idea of the noise levels generated by various sources, Fig. 1.2 presents the different dB levels and everyday sounds that mostly produce those intensity levels.

NIHL is the most common occupational disease in the US Military [13]. It can be either temporary or permanent depending on the noise intensity level and the duration of exposure. With a temporary hearing loss, normal hearing will usually return after a rest period away from all sources of intense or loud noise. This temporary decrease in hearing ability is called a Temporary Threshold Shift (TTS), because the level at which sound can be heard has been raised. TTS occurs when hair cells in the inner ear have been bent by vibrations and need time to bounce back. Permanent Threshold Shift (PTS), is the result of hair cell or nerve destruction within the cochlea. Once these important parts of hearing are destroyed, they can never be restored or regenerated. PTS can range from slight impairment to nearly total deafness. To better understand TTS and PTS, an overview of the anatomy of the human ear is presented in Appendix A.3. Tinnitus is also associated with NIHL. This is a condition described as the perception of sound, often buzzing, ringing, or hissing, in the absence of external stimuli. This takes away the opportunity for the person to experience quietness, which can be very distressing.

The gradual progression of NIHL may be less dramatic than an injury resulting from a workplace accident, but it is a significant and permanent handicap for the affected individual. The WHO estimates that 10% of the world's population is exposed to dangerous noise levels on daily basis. About 5% of these people suffer from NIHL [14]. Loss of hearing denies people sensory experiences that contribute to the quality of their lives. For some, loss of hearing may impede their ability to be gainfully employed. This tragedy is preventable.

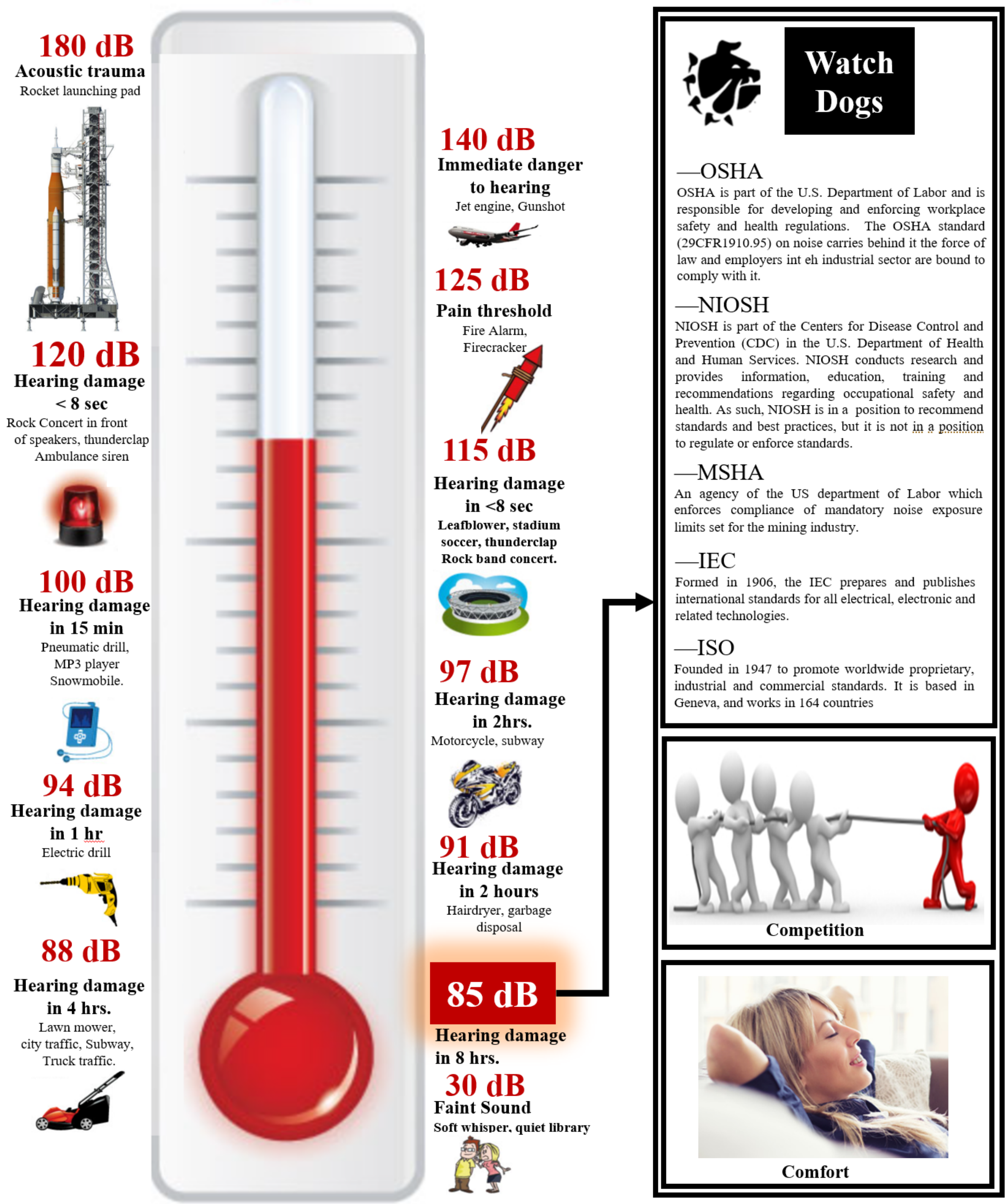

Fig. 1.2 The noise thermometer [1]

1.3 Noise Level Regulation and Standardization

In most countries, governments have issued legislation to regulate the amount of noise permitted to occur as a result of different activities such as industry, construction work, and community activities. The goal of such legislation is to create a salubrious “soundscape”, where noise pollution is brought down to innocuous levels in order to reduce NIHL-related health issues in the population.

For example, in the United States, the Department of Labor added a safety regulation on industrial noise exposure to the Walsh Healey Act in May 1969 [2], which set out a time-weighted average limit of 90 dB of noise exposure over an 8-hour shift. In the United Kingdom, the Health and Safety at Work Act (1974) gives the worker the right to promote and develop measures to ensure his health and safety at work. It proposed that the permissible exposure limit (PEL) should not exceed 85 dB. In Canada, a new regulation (O. Reg. 381) came into effect in 2016. It requires employers to protect workers from overexposure to noise. If workers are exposed to levels above 85 dB, the employer must consider using engineering and administrative controls to reduce noise at the source or along the path to the worker. Where engineering or administrative controls cannot be implemented or while such controls are being put in place, the employer can also consider providing workers with hearing protection devices such as earplugs, earmuffs and so on.

Many other governments worldwide have similar agencies that enforce laws to limit the release of noise pollutants into the environment. Table 1.1 (I-INCE, 1997) characterizes the permitted noise exposure limit requirements for some selected countries, and the year such laws were promulgated. EC is the Engineering Control dB levels for each jurisdiction.

The ability to assess the noise level to investigate whether there is a risk of NIHL present, or that any regulation has been violated or both, means that the noise level must be measured. However, the measurement procedure may depend on the type of noise being assessed. All measurements made on the same type of noise situation, e.g. industrial noise, must be made the same way, otherwise measurements will be incomparable. This calls for standardization of measurement procedures. International standardization boards such as the ISO and the IEC are tasked with such compliance responsibility. They enforce standards on the noise levels emitted by rotating electrical machines. For example, ISO R1680-1970 [15] standard specifies the following: the number of measurement positions around the machine, the type of mounting, the operating conditions, and the type of noise

Table 1.1 Worldwide Legislation on Noise Levels

Jurisdiction	PEL(8-hr avg.)[dB]	Exchange Rate [dB]	EC [dB]
Argentina, 2003	85	3	85
Australia, 2000	85	3	85
Brazil, 1992	85	5	85
Canada, 1991	87	3	87
Chile, 2000	85	3	-
China, 1985	85	3	85
Colombia, 1990	85	5	85
European Union, 2003	87	3	85
Finland, 1982	85	3	85
France, 1990	85	3	-
Germany, 1990	85	3	90
Hungary,1991	85	3	90
India, 1989	90	-	85
Israel, 1984	85	5	85
Italy, 1990	85	3	85
Mexico, 2001	85	3	85
Netherlands, 1987	80	3	85
New Zealand, 1995	85	3	85
Norway, 1982	85	3	-
Spain, 1989	85	3	90
Sweden, 1992	85	3	85
United Kingdom, 1974	85	3	90
United States, 1969	90	5	90
Uruguay, 1988	85	3	85
Venezuela, 1999	85	3	-

measurement equipment; and also, it gives recommendations on the limits of vibration severity. The ISO collaborates with the standards organizations of 164 member countries, which means that all of its members are required to abide by ISO R1680-1970. The IEC 61672-2013 [16] standard, also provides generic PEL standards for its affiliates worldwide.

Aside from the hardline PEL policies enacted by these parastatal agencies to reduce noise emission levels, there are also soft calls through awareness programs such as "Buy Quiet" in the US, for example, to promote the selection and purchase of low-noise machinery and equipment. NIOSH and NASA are involved in a number of efforts to promote and facilitate the implementation of Buy-Quiet programs. These programs provide incentives to purchase quieter products. As a result, many individuals, companies and even some government entities are motivated to seek out and demand low-noise products.

In response to this paradigm shift, electrical machine manufacturers have began to make reduced noise a marketing feature. This move has witnessed massive investments in developing, testing, and selling of less noisy machines that meet the ever-growing comfort requirement of the general public in recent times, as well as the regulatory statutes.

1.4 Acoustic Noise of Electrical Machines

Electrical machines are encountered in almost all areas of human activity, and they are by far the major contributors to noise pollution in all regions of the world. The acoustic noise produced by electrical machines depends on several factors such as the type of electrical machine, the loading, the operating condition, the maintenance culture and so on. Therefore, to begin the study of the acoustic field around the electrical machine, it is imperative to clearly understand the basic principles of rotating machines, the major components that play key roles in acoustic noise generation, the various types of electrical machines, their characteristics and applications. Appendix A.4 provides a brief discussion on the types of electrical machines and how they achieve rotational motion to equip the reader with the fundamental knowledge to understand the rest of this document. It must be mentioned that the interior permanent magnet synchronous motor (IPMSM) has been selected as the working example, and this thesis treats the IPM motor from an application point of view. Therefore, emphasis is given more to the electromagnetic, structural and acoustic performances than to the design of the electric motor itself.

Over the past decades, a lot of research has been done to better understand the provenance and the composition of the acoustic field around an electrical machine. The consensus has been that the acoustic field is a cumulative effect of several noise sources. The type of acoustic noise is identified by the origin of the vibrations that initiated it. In general, three (3) main sources of acoustic noise have been identified in an electrical machine. They include the following: aerodynamic vibrations and noise, electromagnetic vibrations and noise, and mechanical vibrations and noise [3]. In electric motor drives where power electronic converters are connected to the electric motor to control the speed, electromagnetic noise can further be separated into *Magnetic* and *Electronic* sources. Fig. 1.3 presents a summary of the origin and the types of acoustic noise in a typical electrical machine.

In the following, the most important aspects of the aerodynamic and mechanical sources of vibration and noise have been reviewed. The electromagnetic noise, which is the main focus of this thesis and the most dominant component of the total acoustic noise in most small and medium-sized electrical machines, will be discussed in detail in the next chapter.

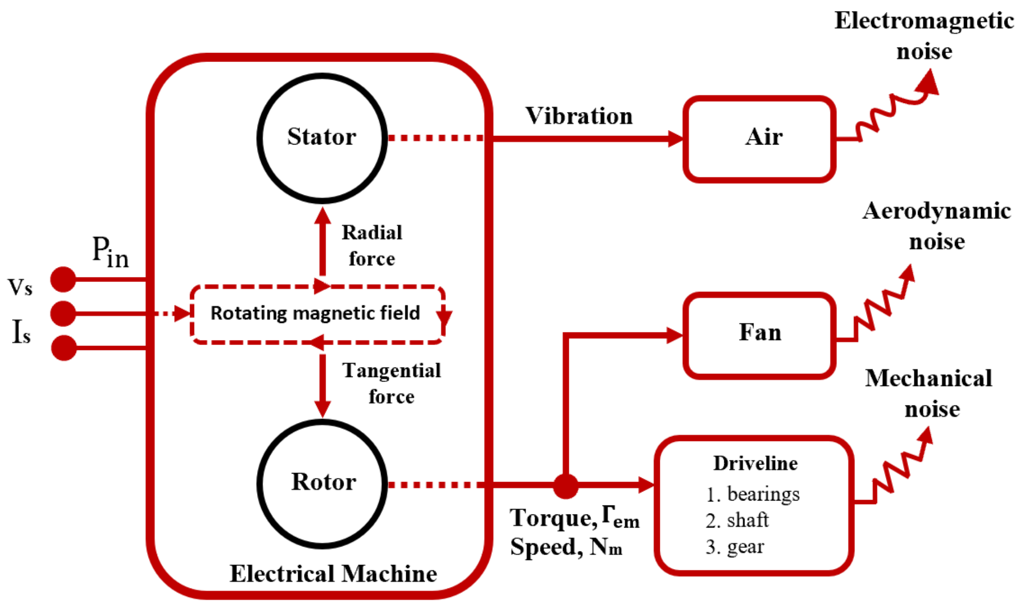

Fig. 1.3 Classification of noise in electrical machines

1.4.1 Aerodynamic vibration and noise

The basic source of aerodynamic noise is the motor cooling fans that create air flow turbulence while rotating. In non-sealed electric motors, the noise of the internal fan is emitted through the vents. In totally enclosed electric motors, the noise of the external fan dominates the acoustic field. The acoustic power of turbulent noise produced by a fan is given by (1.1) [17], where k_f is a coefficient dependent on the fan shape, ρ is the specific density of the cooling medium, c is the speed of sound, v_{bl} is the circumferential speed of the blade wheel and D_{bl} is the diameter of the blade wheel. The sound power level due to the fan is calculated by dividing (1.1) by P_0=10^{-12} W, and putting the result into (A.1). For example, for $k_f = 1$, $\rho = 1.88$ kgm^{-3}, c=344 ms^{-1}, v_{bl}=15 ms^{-1}, and D_{bl}=0.2 m, the aerodynamic sound power level is P_{SL}=75.9 dB.

$$P_S = k_f \rho \left(\frac{v_{bl}}{c} \right)^6 D_{bl}^2 \tag{1.1}$$

According to the spectral distribution of the fan noise, there is broadband noise (100 Hz to 10 kHz) and siren noise (tonal noise). The siren effect is a pure tone being produced as a result of the interaction between fan blades, rotor slots or rotor axial ventilation ducts and stationary obstacles. Siren noise can be eliminated by increasing the distance between the impeller and the stationary obstacle. Aerodynamic noise usually becomes the most important acoustic contributor at high speeds. In general, electric motors that are operated beyond 120,000 RPM are mostly rich in acoustic noise of aerodynamic origin [18].

Several solutions exist to reduce their contribution to the overall emitted noise. One of the most interesting solutions is the use of liquid cooling [3]. Despite eliminating fan-originated noise, aerodynamic losses still contribute to noise radiation. However, since this physical phenomenon involves fluid dynamics and has a fairly low overall contribution in liquid-cooled designs, aerodynamic noise is not addressed in the scope of this thesis.

1.4.2 Mechanical vibration and noise

The defects in some parts or components of the electric motor can cause operational aberrations such as moving parts rubbing together or colliding. These physical interactions between parts and/or components can provoke resonance in the motor structure, thereby amplifying the mechanical vibrations. Mechanical vibrations and related noise are mainly due to bearings, their defects, journal ovality, sliding contacts, bent shaft, joints, and rotor imbalance. The rotor should be precisely balanced as it can significantly reduce the vibration. The rotor imbalance causes rotor dynamic vibration and eccentricity which in turn results in noise emission from the stator, rotor, and rotor support structure.

Both sleeve and rolling bearings are used in electrical machines. The sound power of sleeve bearings is lower than that of rolling bearings. The vibration and noise produced by sleeve bearings depends on the roughness of sliding surfaces, the lubrication, the stability and whirling of the oil film in the bearing, the manufacturing process, the quality and the installation. The sound power of rolling bearings depends on the accuracy of bearing parts, the mechanical resonance frequency, the running speed, the lubrication conditions, the tolerances, the alignment, the load, and the presence of foreign materials [19].

In general, mechanically-induced acoustic noise due to bearings increases with speed but its frequency is too low to create significant noise issues in the electrical machine, unless the bearing is faulty. Also, proper manufacturing practice, calibration and alignment of the machines is assumed so the mechanical sources are not addressed in this thesis.

1.5 Literature Review on Acoustic Noise of Electrical Machines

Conceptually, acoustic noise can be studied by modeling an electrical machine as consisting of three (3) coupled sub-systems: an electromagnetic subsystem (EMS), a structural subsystem (STS) and an acoustic subsystem (ACS) [20]. Fig. 1.4 shows how electrical energy is converted into acoustic energy in an electrical machine. The modeling equations can be expressed as (1.2), where matrix [A] is the coupling between the fluid and structure degrees of freedom at the wet interface, subscripts s and f represent the partitions of the structure and the fluid degrees of freedom respectively. The [M], [B], and [K] are the distributed mass, damping and stiffness matrices. The notation $\{P\}$ denotes the forcing vector applied to the degrees of freedom, while u_s and p are the resulting displacements representing the stator vibrations and that of the fluid respectively. Briefly, the electromagnetic model is evaluated to determine $\{P_s\}$ that are responsible for provoking $\{\dot{u}_s\}$. Then, the structural model calculates the stator vibrations due to the electrical excitation. Lastly, a connected acoustic model uses the stator vibrations to excite the the surrounding air to produce pressure fluctuations $\{P_f\}$ which are translated as acoustic noise.

To calculate this complex multi-physics problem, each subsystem in Fig. 1.4 can be modeled either by analytical or numerical means. A combination of both analytical and numerical methods have also been used extensively in the literature. Appendix A.5 discusses the analytical and the numerical methods of predicting acoustic noise in detail.

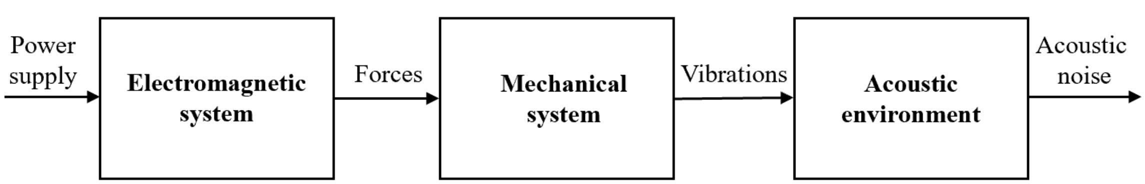

Fig. 1.4 Conversion of electrical energy into acoustic energy in machines.

$$\begin{bmatrix} \mathrm{M_s} & 0 \\ -\mathrm{A}^{\mathrm{T}} & \mathrm{M_f} \end{bmatrix} \begin{Bmatrix} \ddot{\mathrm{u}}_{\mathrm{s}} \\ \ddot{\mathrm{p}} \end{Bmatrix} + \begin{bmatrix} \mathrm{B_s} & 0 \\ 0 & \mathrm{B_f} \end{bmatrix} \begin{Bmatrix} \dot{\mathrm{u}}_{\mathrm{s}} \\ \dot{\mathrm{p}} \end{Bmatrix} + \begin{bmatrix} \mathrm{K_s} & \mathrm{A} \\ 0 & \mathrm{K_f} \end{bmatrix} \begin{Bmatrix} \mathrm{u_s} \\ \mathrm{p} \end{Bmatrix} = \begin{Bmatrix} \mathrm{P_s} \\ \mathrm{P_f} \end{Bmatrix} \tag{1.2}$$

Before the early 1970s, very little was known on the subject of vibrations and noise of electrical machines due to a lack of engineering importance [21]. The world at that time, relied heavily on the works of pioneers like Jordan [22], Yang [2] and others to study the acoustic noise behavior of electrical machines. Since then, many scholars such as Gieras, Timar et al. [3], [19] over the past few decades have expanded the boundary of knowledge and made strides in this area. Improving the existing works and investigating possible solutions to emerging acoustic noise problems is still an active research topic in the design and optimization of electrical machines. This section briefly discusses how acoustic noise of electrical machines is modeled as a multi-physics problem, and uses the understanding to review the current state-of-the-art research works as a basis to develop a plan for the rest of this thesis.

1.5.1 A discussion of some selected publications

Besnerais et al [23], proposed an analytical method to predict the vibration response of variable-speed induction machines. Their method is based on the analytical expression of the static deflections of an equivalent ring of the stator core, which is scaled to consider the effect of stator's natural frequencies. Their method is able to produce the vibration response for a wide range of operating conditions, but since the model is based on the analytical model, its applicability and modularity are limited to specific applications. Rakib [24] also attempted to predict and convert radial displacement to sound power using analytical equations. The limitation of his work was in the formulation of the analytical equations, which was based on simple mechanics. That was not sufficient to represent the overall motor assembly. Also, the effects of the end bells were neglected. These effects could be quite significant according to [25]. Similarly, an analytical model is established in [26]. By using this model, a quick prediction of acoustic noise is achieved.

The authors in [27] established a multiphysics simulation platform to evaluate the noise of a PMSM.The radial force harmonics delivered by the electromagnetic field analysis are exported to an integrated 3-dimensional FE software to calculate the noise. Dos Santos et al [28], and [29] developed a finite-element model to evaluate the vibrations and noise level of an SRM. However, the effects of windings, enclosure and end cover were ignored by both authors. Wang [30] and Torregrossa [25] realized the importance of structural intricacies and simulated a full structural model to improve accuracy of results. In addition, [25] individualized constituent parts to illustrate the variations in modal frequencies. Reference [31] presented a comprehensive experiment to clarify the influence of various structural parts, such as the rotor, and end-shields on the modal frequencies of the induction motor. Daesuk [32] also studied the noise behavior of PMSMs by using the model proposed by Wang in [31].

In [33], the excitation force harmonics, the factored eigenmodes and their corresponding frequencies were fed into an acoustic boundary-element solver to predict the noise behavior of the motor. The authors in [34] used simple structural equations originally proposed by Jordan in [21] to estimate the magnetic noise. Jordan's equations date back to the 1950s. A similar analytical approach is adopted by [35] to superpose the noise contributions of harmonic forces to estimate the global magnetic noise. In [36], [37], and [38], the analytical model and the numerical model are combined to produce accurate results in the electromagnetic and structural parts, and faster prediction of noise in the acoustic field. The exciting forces and modal parameters are obtained from the finite-element simulations, while vibrations and noise are calculated using the equations in [39]. Reference [40] proposed a frequency-domain vibration analysis method for the electric machines, which is based on the modal decomposition of the magnetic force field, combined with the classical mode superposition method. The proposed method enables the fast reanalysis of the vibration response of electric machines at various operating conditions without the necessity to re-evaluate the frequency response FEA at every operating condition.

In [41], the authors studied the inverter effect, on the acoustic behavior of the double-sided Axial-Flux Permanent Magnet machine (AFPM). A few modal frequencies within the audible frequency range were considered. The study reveals a connection between the inverter effect and the most critical harmonics. In [42], a numerical prediction model for vibration and noise of axial flux motors is presented. The procedure developed is capable of considering the influence of both fundamental and high-order electromagnetic forces acting on the surface of stator teeth. Mostafa et al. [43] studied the origin and formation of radial forces in the SPM motor. A simple structural equation proposed in [44] is presented to establish a relationship between the harmonic force orders and stator deformation amplitudes. McDevitt [45], carried out a similar study on the induction motor using the finite-element method. Both authors were interested in the effect and contribution of the zeroth-order force wave (i.e., the dc component). Garvey et al. [46] studied the vibrational sensitivity of the stator to tangential force excitation at the tooth tip by simulating a frequency sweep of force waves through the frequencies of interest. In [47], the finite-element method is used to investigate the contribution of the magnet and the effects of the pole-arc factor on vibrations and noise of a disk permanent-magnet synchronous machine (DPMSM). A similar approach is presented in [48], in which the axial force analysis is used as a guideline to noise control. Song et al. [49] optimized the switching frequency of an inverter-fed Axial-Flux PM motor to reduce noise levels and machine losses.

Ennassiri et al. used several numerical methods in [50] to study fully-coupled and weakly-coupled multiphysics models for evaluating acoustic noise. The authors in [51] adopted the modal superposition method discussed in [50] to analyze the acoustic behavior of a DSFPM generator. FE simulations are used in [52] to compared the noise levels of two SRMs with different winding arrangements. A similar comparison is done in [53]. Dajaku [54] presented analytical models to study the radial forces and the vibration modes of the PM motor for different winding configurations and rotor topologies. [55],and [56] simulated different machine topologies to compare their radial forces. In [57], [58], [59], [60], the PM motor with concentrated windings is shown to be more susceptible to low-frequency resonant vibrations.

In [61], a detailed vibroacoustic assessment was conducted with the aim to achieve a proper understanding of the noise generation and propagation mechanism in PMSMs. It was found that a relationship between the current profiles and vibro-acoustics exists. The frequencies of radial force harmonics and mode characterization of the motor were studied in [62]. It shows that the radial force harmonics with the lowest mode number can lead to large vibrations. The influence of the frame on the natural frequencies and acoustic noise emission in an SRM was analyzed in [63]. The results show that the effect of thickness of the frame on the natural frequencies is more pronounced than that of the cooling ribs.

In [35], a universal framework for modeling acoustic noise of electric motor drives is presented. The simulated acoustic spectrum using this method is validated against measurements. [64] analyzed the influence of PWM strategies on the acoustic noise, which revealed that the PWM is critical only when the acoustic noise is dominated by the magnetic force. Furthermore, an experimental procedure was also presented to study the vibro-acoustic behavior of the electric motor with high frequency harmonic currents [65]. The ‘impulse response' method has been reported in many research papers. By exciting the stator with an impulse signal (a unit force wave), one can extract the entire frequency domain information of the system. In [66],[67] and [68], the modal properties of the stator are obtained by impulse response instead of modal testing, and then vibrations and noise are calculated by loading the force into the center of the teeth surface.

1.5.2 Exploring the research gaps in literature

Since 1970, the finite element method discussed in Appendix A.5 has been applied to rotating electrical machines to improve upon the fidelity of their subsystem models for performance analysis including acoustic noise calculations [69]. For electromagnetic modeling, it is shown that the majority of the works on noise calculations are focused on sinusoidally-excited models. However, modern inverters-driven electrical machines provide pulsed voltage to the stator windings. Hence in the real world, electrical machines are mostly supplied with current waveforms that are not purely sinusoidal. Although non-sinusoidal current is known to enrich the harmonic content of the electromagnetic forces responsible for acoustic noise [3], there is still a lack of information in the literature.

Aside from increasing the harmonic amplitudes of the electromagnetic forces, non-sinusoidal current excitation can also result in power losses in the electrical machine [70]. For long running hours, the losses in the machine can be quite significant which can result in serious thermal issues if there are no proper thermal insulation and cooling management in place. But as mentioned earlier, when modeling acoustic noise, the electrical machine is represented as coupled electromagnetic, structural, and acoustic subsystems. Although this approach has been widely adopted in the literature, it fails to account for possible fluctuations in the operating temperature conditions due to the power losses resulting from non-sinusoidal excitation of the stator winding. For this reason, the coupled subsystems must be modified to include a thermal model to account for the effects of temperature on the output noise of the electrical machine. A survey of the literature, however, reveals that not much work has been done in this area.

Finally, numerical models such as the finite element method have proven to be the most effective and widely used means of evaluating the acoustic noise of electrical machines. But the approach can be time-consuming, especially when simulating very complex electrical machines. For this reason, adding an extra model, i.e., the thermal model, will further exacerbate the simulation time, particularly during optimization where thousands of electrical machines must be assessed for their acoustic performance. Therefore, it is imperative to find an alternative means of achieving similar results predicted by the numerical models while reducing the associated computational cost at the same time. A surrogate model appears to be the most appropriate candidate for this task and its application in engineering design is gradually gaining popularity. However, not much is known about their mimicking effectiveness when it comes to predicting the acoustic noise.

Table 1.2 uses a list of some of the published works from the past ten years to explore the gaps in the literature and the emerging research direction of noise and vibrations analysis of electrical machines. The grey areas point the reader to the research areas that are by no means mature and need more effort. Therefore, this thesis addresses some of the issues related to these areas and is predicated on an in-depth discussion of the following topics:

- The impact of non-sinusoidal excitation on the acoustic noise of electrical machines;
- The effect of including thermal models in the acoustic noise calculation framework;
- Exploring alternative prediction models to potentially replace the finite element method.

1.6 The Objective of this Thesis

The general goal of this research is to propose a robust methodology for modeling and analyzing acoustic noise using data-driven simulations, while addressing the pertinent gaps highlighted in the literature. These simulations aim at supporting decision making processes during the design phase. The model's accuracy is essential to ensure, but the solution time/cost must also be taken into consideration.

It is important to note that in this thesis, the focus and studies are emphasized on the Interior Permanent Magnet Synchronous Motor for mostly electric vehicle applications. However, the developed models can be extended to analyze other electrical machines such as Induction Motors, Switched Reluctance Motors and Synchronous Reluctance Motors.

1.6.1 Original contributions

The research presented in this thesis gave rise to a number of original contributions to augment the existing body of knowledge. Some of the contributions were shared with an international audience through peer-reviewed conference publications, presentations and journal articles. References [71]-[72], were taken from some parts of Chapter 3 and Chapter 5 of this thesis, and are already published in the *IEEE Transactions on Magnetics*. The major contributions are summarized below.

- Proposed a sampling technique to extract electromagnetic forces from the airgap space, and added two new sound metrics to quantify acoustic noise arising from the non-sinusoidal excitation of the stator winding. Some parts of these contributions appeared in reference [71]. See the manuscript below.
  - I. Ibrahim, M. H. Mohammadi, V. Ghorbanian, and D. A. Lowther, "Effect of pulse-width modulation on electromagnetic noise of interior permanent magnet synchronous motors", in *IEEE Transactions on Magnetics*, vol.55, no. 10, pp. 1-5, 2019.
- Proposed and validated an alternative solution to the computationally-intensive multi-physics simulation process associated with acoustic noise prediction. Again, some parts of this contribution have been used in reference [72]. See the manuscript below.
  - I. Ibrahim, Rodrigo Silva, M. H. Mohammadi, V. Ghorbanian, and D. A. Lowther, "Surrogate-based acoustic noise prediction of electric motors", in *IEEE Transactions on Magnetics*, vol. 56, no. 2, pp. 1-4, 2020.
- Incorporated thermal models in the multiphysics simulation framework. This accounted for the role of temperature in the acoustic noise performance of the machine.

1.6.2 Outline of Thesis

The thesis is divided into six chapters. Chapter 2 navigates the reader through the causes of acoustic noise in electrical machines and a systematic illustration of how the coupled multi-physics problem is formulated using commercial software packages. The rest of the chapters use the multi-physics system-level simulation framework established in Chapter 2 to address some of the research challenges identified in the literature.

In Chapter 3, the effect of non-sinusoidal excitation of the stator winding is studied for different current waveforms. Here, the acoustic fields around different parametric variations of the Interior Permanent Magnet Synchronous Motor are explored to analyze the impact of the switching frequency of the power electronic circuit connected to the motor. It is a known fact that depending on the quality of the current waveform supplied to the stator winding, the power losses (due to hysteresis and eddy current) in the electric motor can be quite significant. These energy losses are dissipated in the form of heat energy. In the likely event that these losses are too high, they can cause thermal issues in the electric motor. In Chapter 4, an additional model, i.e., a thermal model, is added to the existing subsystem models to account for the impact of temperature rise in the acoustic noise calculation process. This is then used to establish a correlation between acoustic noise and the operating temperature of the electrical machine.

In Chapter 5, the computational cost associated with coupling multiple subsystems in order to achieve the desired acoustic noise objective has been addressed. The Surrogate Models (the alternative to the Finite Element Method) presented in this thesis rely on their ability to emulate the output of very complex finite element simulation codes with the ultimate goal of expediting the design process while maintaining a reasonable level of trade-off between the accuracy of the predicted noise and the solution time.

Lastly, Chapter 6 presents a general discussion to recapitulate the importance, and the major accomplishments of this thesis. It also discusses the author's plans for future works.

1.6.3 Contributions from Collaborators

The contributions of the authors included on the manuscripts associated with some portions of this thesis, particularly chapters 3 and 5 are highlighted below.

- **Chapter 3** is the expanded version of I. Ibrahim, M. H. Mohammadi, V. Ghorbanian, and D. A. Lowther, "Effect of pulse-width modulation on electromagnetic noise of interior permanent magnet synchronous motors," in *IEEE Transactions on Magnetics*, vol. 55, no. 10, pp. 1-5, 2019. Here, I. Ibrahim conceived the sampling approach, and proposed two new acoustic noise quantities to augment the existing analytical equations in the literature. He also performed all the multi-physics simulations and wrote the manuscript. D. A. Lowther reviewed the simulation results and edited the final manuscript. M. H. Mohammadi and Vahid Ghorbanian contributed equally by providing the circuit design specifications for modeling the power electronic drive. The power electronic drive circuit only provided the input current waveforms needed to address the acoustical challenges related to the electric motor itself. Therefore, the design of the power electric drive circuit was not the primary focus.

- **Chapter 4**, however, is not linked to any of the manuscripts mentioned above. I. Ibrahim conceived and executed the entire project with guidance from D. A. Lowther.

- **Chapter 5** is an extended version of I. Ibrahim, Rodrigo Silva, M. H. Mohammadi, V. Ghorbanian, and D. A. Lowther, "Surrogate-based acoustic noise prediction of electric motors," in *IEEE Transactions on Magnetics*, vol. 56, no. 2, pp. 1-4, 2020. Here, I. Ibrahim proposed the idea of incorporating Surrogate Models in the noise calculation process with the ultimate goal of replacing the time-consuming finite element simulations. Rodrigo Silva advised on the selection and suitability of the Surrogate Models to implement. But the actual implementation including writing the simulation codes, fine-tuning the models, validation, testing and writing of the manuscript draft were performed by I. Ibrahim. Vahid Ghorbanian, M. H. Mohammadi, and D. A. Lowther redacted the final manuscript.

Table 1.2 Summary of Research Publications

Reference Number	Electromagnetic Subsystem		Structural Subsystem	Thermal Subsystem	Acoustic Subsystem	Alternative Model
	SIN	PWM				
[10]	X		-		-	X
[18]	X		X		X	
[19]	X		X		X	
[20]	X		X		X	
[21]	X		X		X	
[22]	X		X		X	
[23]	-	X	X		X	
[24]	X		X		X	
[25]	X		X		X	
[27]	X		X		X	
[28]	X		X		X	
[29]	X		X		X	
[30]	-	X	X		X	
[31]	X		X		X	
[32]	X		X		X	
[33]	X		X		X	
[34]	X		X		X	
[35]	X		X		X	
[36]	X		X		X	
[37]	X		X		X	
[39]	X		X		X	
[40]	X		X		X	
[41]	X		X		X	
[42]	X		X		X	
[43]	-	X	X		X	
[44]	X		X		X	
[45]	X		X		X	
[46]	X		X		X	
[47]	X		X		X	
[48]	X		X		X	
[49]	X		X		X	
[50]	X		X		X	
[51]	X		X		X	
[52]	X		X		X	
[53]	X		X		X	
[54]	X		X		X	
[55]	-	X	X		X	
[56]	X		X		X	
[57]	X		X		X	
[58]	X		X		X	
[59]	X		X		X	
[60]	X		X		X	
[61]	X		X		X	
[62]	X		X		X	
[64]	X		X		X	
[65]	-	X	X		X	
[66]	X		X		X	
[67]	X		X		X	
[68]	X		X		X	
[69]	X		X		X	
[70]	X		X		X	
[78]	X		X		X	
[79]	X		X		X	
[81]	X		X		X	
[82]	X		X	X	X	
[91]	X		X		X	
[103]	-		-		-	X
[122]	-		-		-	X
[123]	X		X		X	
[127]	X		X		X	

Chapter 2

Electromagnetic Vibration and Noise

Any mechanical assemblage which vibrates in the air can produce acoustic noise. Acoustic noise is the consequence of the excitation of a mechanical system by electromagnetic forces. For small- and medium-sized electrical machines, especially those rated below 15 kW, the total sound power is dominated by electromagnetically-induced acoustic noise [24]. It is quite often the case that one or more of the natural frequencies of the electrical machine is not far away from the frequencies of the electromagnetic forces. When this happens, the stator radial deflections can amplify dramatically. The effects are dangerous deformations in the stator core, and high tonality vibrations. When the mechanical vibrations exceed a certain threshold, usually above 1000 Hz, it propagates in the surrounding air and generates acoustic noise [3]. Fig. 2.1 (a) illustrates how the radial and tangential forces excite the stator tooth of a surface-mounted permanent magnet synchronous motor. The general mechanism of acoustic noise emission in the electrical machine is portrayed in Fig. 2.1 (b).

The acoustic noise emanating from aerodynamic and mechanical sources can be mitigated even after the electrical machine has been manufactured. For electromagnetically-induced acoustic noise, any abatement measure will require design engineers to modify the magnetic performance of the machine. Also, design engineers must be able to assess the natural frequencies of the stator and the rotor so that appropriate winding or structural designs can be arranged to give a mismatch of the frequencies of the important exciting force waves and the natural frequencies of the machine. Either pursuit can be very costly for an existing machine. Hence, electromagnetically-induced acoustic noise output must be addressed during the digital prototyping stage since mitigation is nearly impossible once the machine has been manufactured. For this reason, electromagnetic noise has commanded a lot of research attention in the design and optimization of electrical machines.

This section reviews electromagnetic forces (Maxwell forces, Laplace forces, and Magnetostrictive forces) as the possible cause of electromagnetic vibrations and acoustic noise, and the dynamic response of the machine structure when agitated by these electromagnetic forces. It focuses more on understanding how the radial magnetic forces are formed from the air gap magnetic flux density harmonics, the characteristics of the radial force waves and how they interact with the machine structure to cause stator radial vibrations.

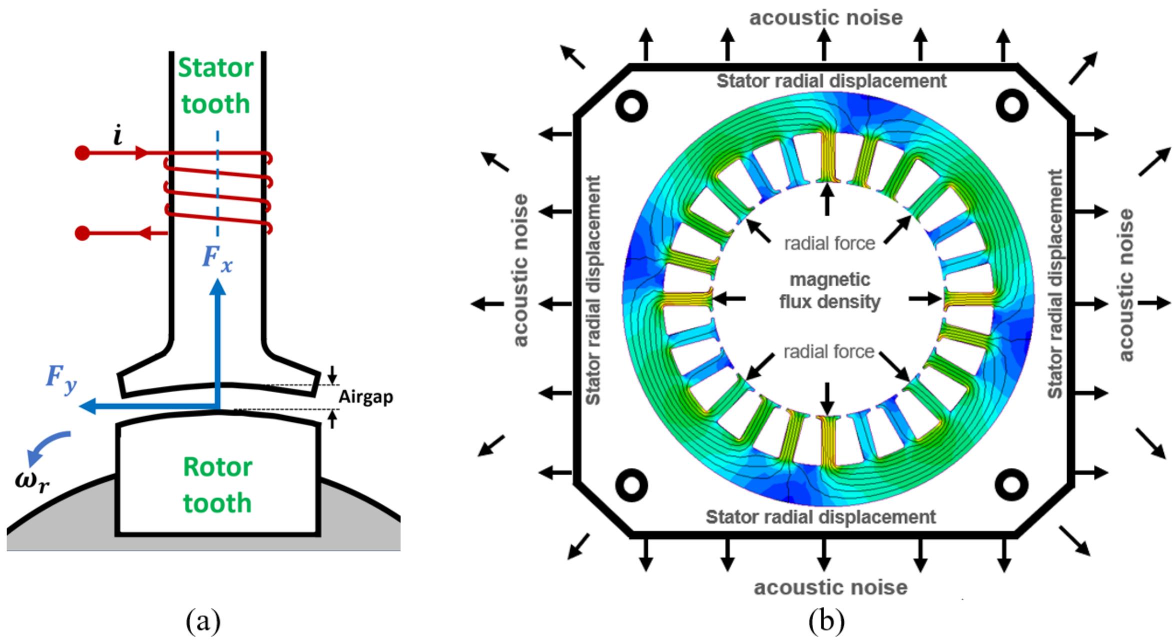

Fig. 2.1 (a) Radial force (F_x) and Tangential force (F_y) on pole-tooth pair (b) Mechanism of electromagnetic vibration and noise of electrical machines.

2.1 Electromagnetic Forces

2.1.1 Maxwell Forces

The electromagnetic forces that act on the stator or rotor surface are popularly referred to as *Maxwell forces*. These forces are responsible for the radial and tangential vibrations in the electrical machine. Hence, this family of forces can be resolved into two components: *radial* and *tangential* forces. Much of the vibrations and acoustic noise is generated by virtue of the radial component acting normally on the stator teeth. The tangential component of the force causes torque ripple and can sometimes contribute to the vibrations of the stator. In most cases, this component is ignored because under standard operating conditions, the average radial force far exceeds that of the average tangential force. The magnetic permeability of the ferromagnetic core is much higher than that of the air gap. So, the magnetic flux lines are practically normal to the stator and rotor cores. Hence, the tangential component of the flux is much smaller than the radial component and can be neglected [73]. In IMs, where the air gap is very small, the field is almost purely radial [36]. However, Garvey et al. reported in [46] that for very large motors, tangential forces can have a significant impact on the noise emission.

2.1.2 Laplace Forces

These electromagnetic forces act on the stator and rotor windings. The Laplace forces can initiate vibrations in the stator coils, which can potentially lead to insulation breakdown and short circuit problems. Fortunately, these forces are the least of our worries because a suitable selection of insulating materials can eliminate the effects of Laplace forces.

2.1.3 Magnetostrictive Forces

Magnetostriction is the change of physical dimensions and crystal structure of a ferromagnetic material in response to changing its magnetization. This phenomenon is another cause of vibrations and noise, but it is more prominent in power transformers [3]. The contribution of magnetostrictive forces to the total noise field around the electrical machine is still a subject of scientific debate. But experimental results presented in [74], and the author's experience in the NVH area, affirm that there is no need to model magnetostrictive effects to account for acoustic noise issues in rotating electrical machines.

2.1.4 Radial Magnetic Forces

The radial magnetic force is the main cause of electromagnetic vibrations and acoustic noise in electrical machines. These force waves are produced by the air gap magnetic flux density harmonics. The stator flux and the rotor flux constitute the total air gap magnetic flux. For a typical poly-phase electrical machine fed with a balanced sinusoidal current system, the magnetic flux density contributions can be expressed by (2.1a) and (2.1b), where B_s

and B_r are the stator and rotor magnetic flux densities, α is the angular distance from the origin of the coordinate system, v and μ are the stator and rotor magnetic flux density space harmonics, and p is the number of pole pairs. The causes of the flux harmonics are:

- spatial magnetomotive force harmonics due to the nonsinusoidal distribution of stator and rotor windings [75];
- harmonics in the air gap permeance, which depends on the following factors: the number of stator slots and rotor poles [76], [77]; the geometry of the slots and teeth in the stator as well as the rotor [77], [20]; and the saturation in the iron core [78].
- harmonic currents in the stator windings [75].

The radial magnetic force distribution in the air gap can be described as a superposition of a series of rotating force waves. Each force wave is identified by a frequency, a spatial harmonic mode (in some literature, it is often referred to as a *rank* or an *order*, an amplitude, a phase angle and a rotation direction [10]. The space and time distribution of a single radial force per unit area can be expressed by (2.1c). Here, P_r is the radial magnetic force wave, $r = 0, 1, 2, \ldots$ are the corresponding modes of the force wave, P_{mr} is the amplitude of the r^{th} order radial force wave, and $\omega=2\pi f$ is the angular frequency. ϕ_r is the phase angle. The P_{mr} of the radial force wave of the r^{th} order in (2.1c) depends on the space harmonics, B_v and B_μ, participating in its production.

$$B_s(\alpha, t) = \sum_{v=1}^{n} B_v \cos(vp\alpha \pm \omega t) \tag{2.1a}$$

$$B_r(\alpha, t) = \sum_{\mu=1}^{n} B_\mu \cos(\mu\alpha \pm \omega t) \tag{2.1b}$$

$$P_r(\alpha, t) = P_{mr} \cos(r\alpha - \omega_r t + \phi_r) \tag{2.1c}$$

Because the radial magnetic forces are formed from the self- and mutual interactions between B_v and B_μ, they can be divided into three (3) fundamental groups: (1) Radial forces that are excited by the stator harmonics of the same order; (2) Radial forces that are excited by the product between stator and rotor harmonics (Generally, acoustic noise is mostly caused by radial forces in this group); and (3) Radial forces that are excited by the rotor harmonics of the same order. Table 2.1 shows the characteristics of the three main groups of the radial magnetic forces, where μ_0 is the vacuum permeability constant, Z_s is the total number of stator slots, and k = 0, 1, 2, 3,...is an integer.

Table 2.1 Classification of Radial Magnetic Forces

	Origin	Amplitude	Order	Velocity
1	Excited by the stator harmonics of the same order	$\frac{B_{m\upsilon}^2}{4\mu_0}$	$2\upsilon p$ $2(\upsilon p \pm kZ_s)$	2ω
2	Excited by product between stator and rotor harmonics	$\frac{B_{m\upsilon}B_{m\mu}}{2\mu_0}$	$(\upsilon \pm \mu)p$ $(\upsilon \pm \mu)p + 2kZ_s$	$2\omega(\upsilon \pm \frac{\mu}{p})$
3	Excited by the rotor harmonics of the same order	$\frac{B_{m\mu}^2}{4\mu_0}$	$2\mu p$ $2(\mu p \pm kZ_s)$	$2\omega_\mu$

The notion of mode number has been extended to characterize how the harmonics of the radial force evolve along the air gap of electrical machines. Physically, r is a circumferential wave number which describes the spatial frequency of a periodic quantity, generally along the air gap of the electrical machine or along the stator teeth. It also corresponds to the number of maxima and number of minima of the wave along the air gap. The use of modes is very useful when analyzing electromagnetic vibrations and noise of electrical machines because resonance does not only depend on the coincidence or nearness of the electromagnetic excitation frequency and the natural frequency of the stator system, but it also depends on the match between structural modes and the magnetic force mode shape (described by the wave number). The idealized shapes of the radial force for modes r = 0 to r = 5 are given in Fig. 2.2. These shapes are also called *vibration modes*.

Briefly, vibration mode r = 0 represents a uniformly distributed radial magnetic pressure around the stator periphery which changes periodically with time. This is also called the *breathing* mode and can be compared to a cylindrical vessel with a variable equidistant internal over-pressure. For r = 1, also called *beam bending* mode, the radial pressure produces a single-sided magnetic pull on the rotor. Vibration modes r = 2, 3, 4, 5..., result in wave-shaped deflections of the stator core.

It is worth mentioning that the breathing mode represents the equivalent dc component of the vibration modes, and because of its shape, it has very little contribution from the acoustic noise viewpoint. It must be added that the most important force waves are those

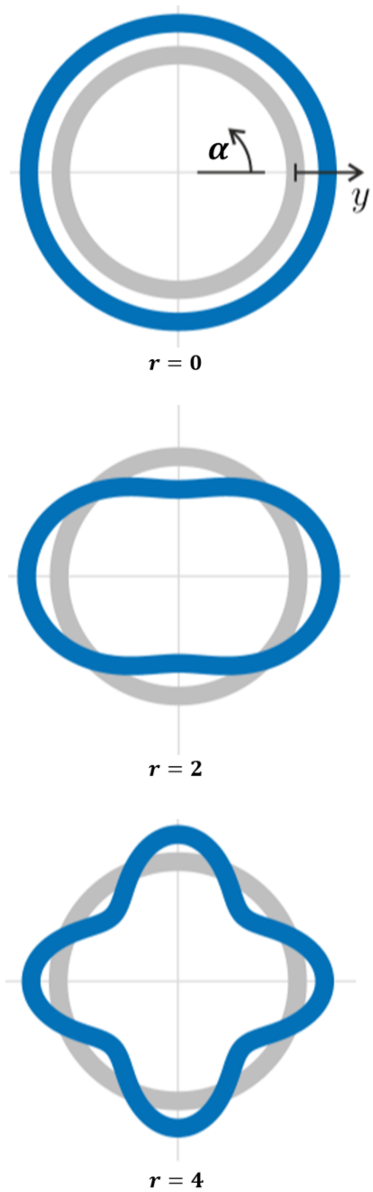

Fig. 2.2 Deformation of stator core by space distribution of radial forces [2]

which satisfy the following conditions:

- the amplitude of the force waves are large, compared with other force waves;
- the mode number r values are low, e.g. less than 10 in most cases.

A higher force amplitude would cause a larger vibration amplitude to emit more noise. The second condition is based on the fact that the deformation of the stator core is an inverse function of the fourth power of the mode number r [3]. Therefore, the lower mode numbers contribute the most to stator core vibrations. In permanent magnet machines, the most dominant mode number is generally equal to the greatest common divisor (GCD) of the slot-pole number. For synchronous motors, the frequencies of r are linearly dependent on the rotor speed and on the number of pole pairs, i.e., $f_r=2rpf_p$, where p is the number of pole-pairs, and f_p is the rotating frequency of the rotor [79].

2.2 Mechanical Behavior of the Stator

As discussed earlier, the electromagnetic force acting on the core of the stator may produce troublesome noise and vibration, especially when the frequencies of the exciting forces are equal or near to the natural frequencies of the machine concerned. This can be represented by the lumped parameter model with N degrees of freedom given in (2.2a), where $[M_s]$, $[B_s]$, $[K_s]$, $\{P_s\}$ and $\{\dot{u}_s\}$ are the same symbols as defined in Chapter 1.5.

To measure the acoustic capacity of an electrical machine, design engineers must be able to assess the natural frequencies of the stator. Briefly, natural frequencies are the frequencies at which a structure naturally tends to vibrate without any forced disturbance. If any of these frequencies are excited, resonance occurs and the structural vibrations are amplified significantly. Each natural frequency is associated with a uniquely deformed shape called the *modeshape*. The natural frequency and its corresponding modeshape is an indication of how a structure will respond to dynamic loading. The two quantities depend on the structural properties, i.e., the geometry and the material, and the boundary constraints. If the structural properties change, the natural frequencies also change, but the modeshapes may not necessarily change. However, if boundary constraints change, then the natural frequencies and the modeshapes both change. Understanding the modeshapes can be very useful in locating the best points to install accelerometers during stator vibration measurements. An experiment to study the natural behavior of the machine is known as Modal Analysis. Theoretically, modal analysis is performed by solving (2.2a) for free vibrations, i.e., without the damping matrix and the external forces. Hence, (2.2a) reduces to (2.2b). By assuming a harmonic solution of the form in (2.2c), (2.2b) becomes an eigenvalue problem of the form in (2.2d), where $\{\phi\}_i$ and ω_i represent the i^{th} modeshape and the natural circular frequency of the stator respectively. Equation (2.2d) is satisfied if neither the eigenvector nor the determinant of the matrix part is zero. The first case, i.e., eigenvector equal to zero, corresponds to a trivial solution, which is of no interest. The second case provides the natural frequencies.

$$[\mathrm{M_s}]\{\ddot{u}_s\} + [\mathrm{B_s}]\{\dot{u}_\mathrm{s}\} + [\mathrm{K_s}]\{u_\mathrm{s}\} = \{\mathrm{P_s}\} \tag{2.2a}$$

$$[\mathrm{M_s}]\{\ddot{u}_\mathrm{s}\} + [\mathrm{K_s}]\{u_\mathrm{s}\} = 0 \tag{2.2b}$$

$$\{u_\mathrm{s}\} = \{\phi\} \sin \omega t \tag{2.2c}$$

$$([\mathrm{K_s}] - \omega_\mathrm{i}^2[\mathrm{M_s}])\{\phi\}_\mathrm{i} = 0 \tag{2.2d}$$

The earliest known methods for calculating the natural frequencies of a stator of the single-ring type can be credited to Den Hartog in 1928; later, Jordan in 1957; Frohne in 1959 and Üner in 1964 introduced the effects of shear, rotary inertia, teeth and winding into the calculation; Voronetskii in 1956 and Lubcke in 1956 presented methods that added experimentally determined factors to the classic formula; and Pavlovsky in 1968 treated the stator as a single thick ring loaded with teeth and winding configuration and derived numerical tables calculating the natural frequencies [2]. The analytical models of the early days did not guarantee a good accuracy of the calculation since the stator system is a complex structure which consists of a laminated stack with yoke and teeth, a winding distributed in slots, encapsulation, and a frame. Nowadays, finite-element analysis tools such as Simcenter 3D [80] are being sought after as the most competent computational tools for solving complex elasticity and structural analysis problems in the field of engineering and other disciplines.

2.3 Computer-Aided Design of Electrical Machines

The development of low-noise electrical machines means that the acoustic noise characteristics of the electrical machine must be known in the early virtual prototyping stage before it reaches the final design stage. To formulate the acoustic noise problem, the CAD models which include the electromagnetic, the structural and the acoustic subsystems of a real electrical machine can be built using a finite element software. It must be emphasized that although three CAD models must be developed conceptually, it is also possible to use either one or two models in most cases depending on the capability of the software package available. For example, if the user has access to commercial software packages such as MotorSolve or MAGNET and NX Nastran, only two CAD models are needed. The electromagnetic model can be realized using either MotorSolve or MAGNET, while NX Nastran handles the structural and acoustic aspects simultaneously. However, some software packages are integrated with a wide range of FEA solvers which makes it possible to use only one CAD model in a fully-coupled multiphysics simulation. The CAD design process of the electrical machine using the finite element method is summarized in the next section of this document.

2.3.1 The finite element design process

The procedure for developing the CAD models is the same for all types of electrical machines. The process begins with the electromagnetic modeling, where the general design specifications of an actual electric motor must be defined. This includes the material properties, the dimensions of the electric motor, the number of stator slots and rotor poles, the type of winding layout, the rated voltage, the rated motor speed and so on. After setting the design specifications, the motor geometry is sized to obtain its first virtual prototype. Sizing accounts for the electrical, magnetic and thermal loadings of the motor. Cooling requirements are also considered but this, however, is application dependent. For example, the rated current density of the interior permanent magnet synchronous motor prototype used in this thesis is set based on natural cooling, that is, less than 5 A/mm^2.

Next, the user interacts with the simulation object to evaluate the performance of the developed model. This preliminary simulation is to test the accuracy of the CAD model. However, if performance requirements are not met, the model is fine-tuned by modifying the initial parameters and the process may be repeated several times until the final design satisfies the target requirements. The general guideline for creating the electromagnetic CAD model of any electrical machine regardless of the type, the topology and the application, is summarized in Fig. 2.3.

Some of the software packages are equipped with a vast array of machine geometries in their library, e.g., MotorSolve has a wealth of machine geometries in its database, others will require the user to build the geometry from scratch. The latter is often not very convenient for the novice user. However, the interoperable nature of these finite element packages permits CAD geometries developed in one software GUI to be accessed in another software GUI. The structural model can be realized by modifying the imported electromagnetic geometry from MotorSolve to include the housing, the flanges, the support unit and so on.

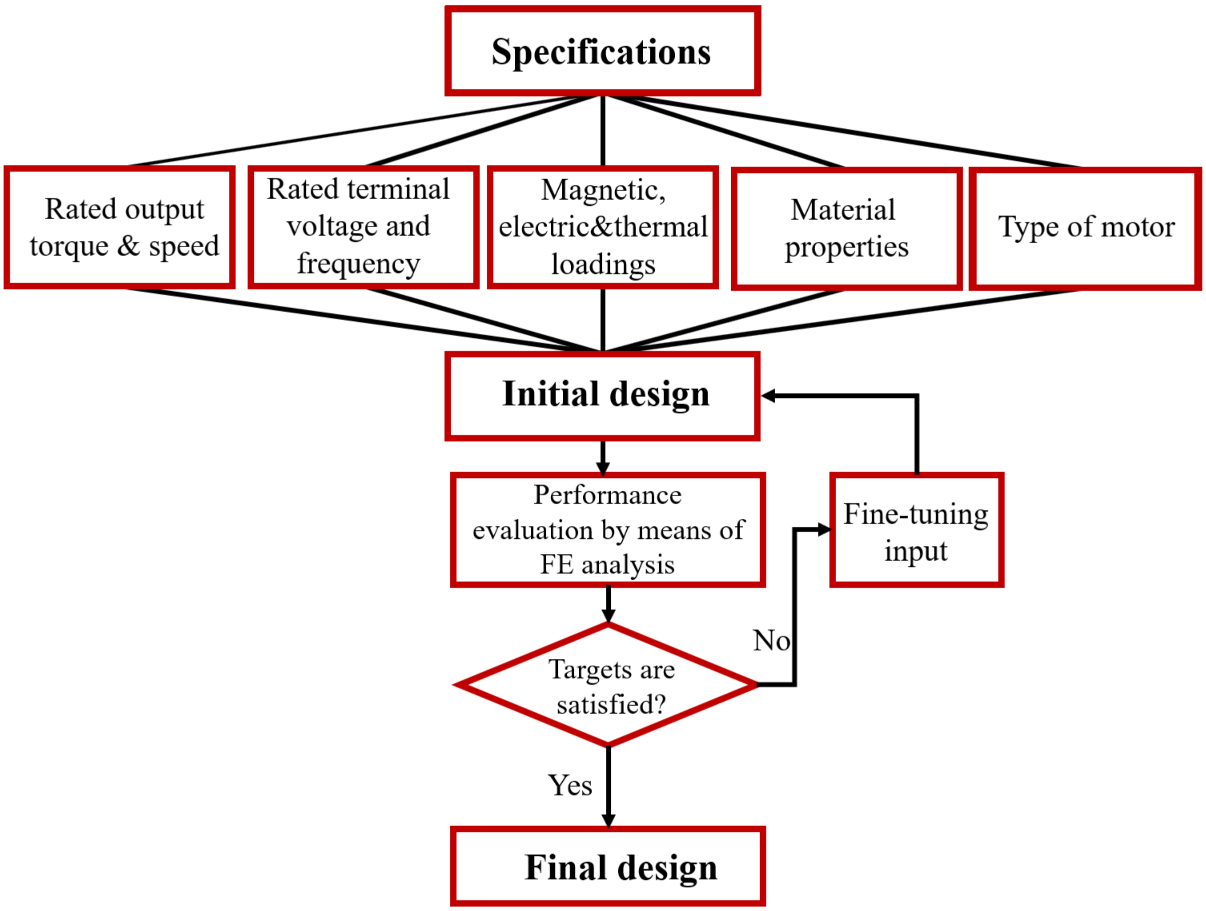

Fig. 2.3 Machine design process.

2.4 FEM Prediction of Acoustic Noise of Electrical Machines

This section uses the finite element method to discuss the steps involved in evaluating the acoustic field around the electrical machine. The procedure for predicting acoustic noise is the same for every kind of electrical machine. In this case study, a 4Pole 24Slot interior permanent magnet synchronous motor has been chosen as the working example. The electromagnetic model of this motor is shown in Fig. 2.4 (a). The structural model is presented in Fig. 2.4 (b). Table 2.5 summarizes the design specifications. The permanent magnet synchronous motor is covered extensively in Appendix A.4. The multi-physics FE simulation path to achieving the acoustic results is delineated in Fig. 2.5, where the electromagnetic and structural models are represented by the source model and the target mesh respectively.

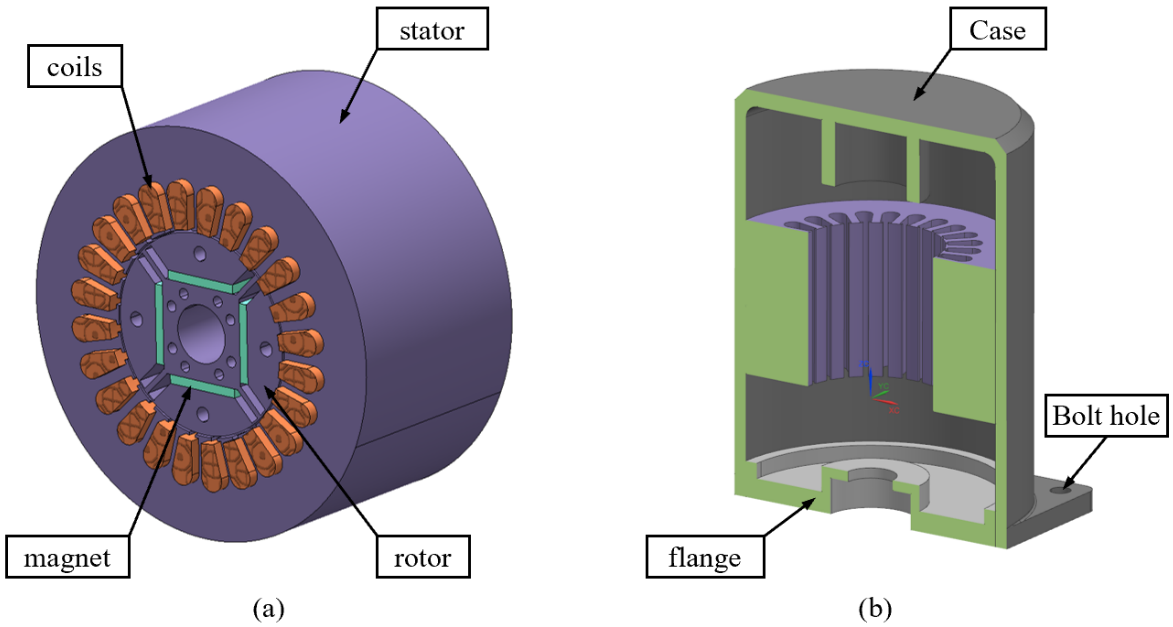

Fig. 2.4 A 4Pole 24Slot Interior Permanent Magnet Synchronous Motor (a) Electromagnetic model (b) Structural model.

Table 2.2 MOTOR DESIGN PARAMETERS

Design parameter	Value	Unit
Number of rotor poles	4	-
Number of stator slots	24	-
Rotor inner diameter	20	mm
Rotor outer diameter	55.00	mm
Stator outer diameter	100.00	mm
Stator stack length	60.0	mm
Stator back-iron thickness	5.40	mm
Stator tooth width	5.44	mm
Stator tooth-tip thickness	0.83	mm
Slot-opening width	1.9	mm
Air gap thickness	0.50	mm

Table 2.3 Acoustic Properties

Design parameter	Value	Unit
Fluid medium	air	-
Speed of sound (air medium)	344	m s^{-1}
Mass density (air medium)	1.225	kg m^{-3}

Table 2.4 Electromagnetic Properties

Design parameter	Value	Unit
Rated current	10	A
Rated voltage	42	V
Core material	M-19 29 Ga	-
PM material	NdFeB 32/27	-
Coil material	Copper	-

Table 2.5 Mechanical Properties

Design parameter	Value	Unit
Rated motor speed	1800	RPM
Young's modulus	190	GPa
Poisson's ratio	0.3	-
Mass density of core	7650	kg m^{-3}

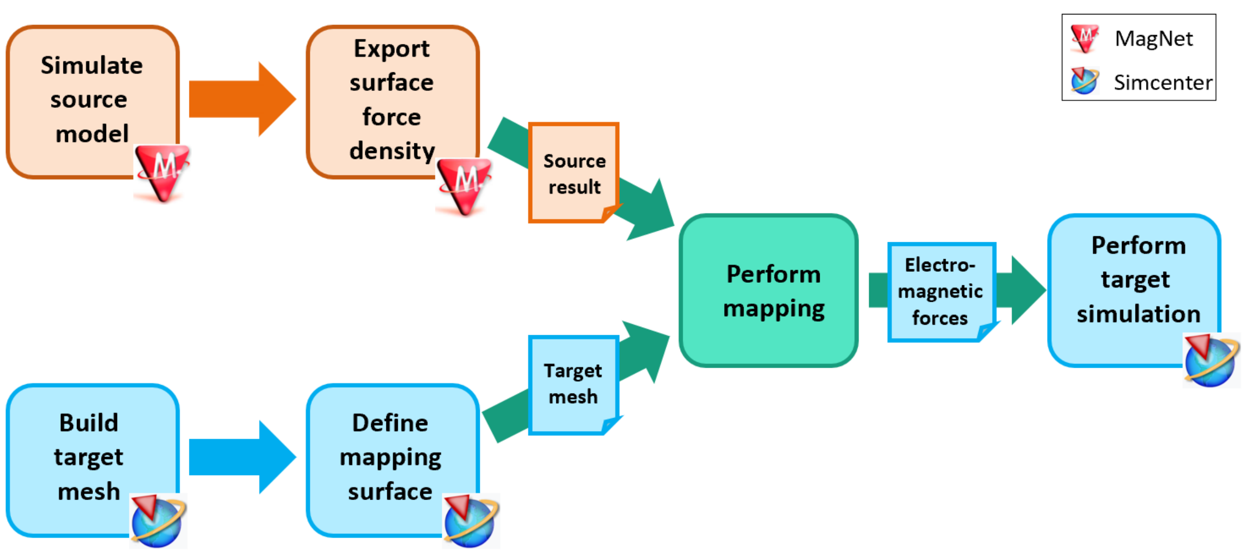

Fig. 2.5 Procedure for simulating electromagnetic-induced vibrations.

2.4.1 Electromagnetic Modeling

Once the source model in Fig. 2.5 is fine-tuned to meet operating conditions, a transient 3D with motion solver can be selected. The choice of a 2D or a 3D solver is motivated by the computational budget allocated to the task and the anticipated accuracy of the simulation results. Then, an EM-field analysis is performed per mechanical cycle of the motor for a fixed sinusoidal current. For 1000 time steps per cycle, it took 10 minutes on an Intel Xeon E5-1650 processor (6 cores, 3.5 GHz, 32 GB RAM) workstation to simulate the full model. Next, the transient field results are sampled to evaluate the nodal forces on the surface mesh. The nodal forces excite vibrations of the structure.

To transfer the electromagnetic force load onto the structural target mesh, the stator surface mesh which contains the nodal forces on it must be exported to Simcenter 3D via an appropriate file extension format. Then, the nodal forces of all 1000 time steps are mapped to the target mesh. To ensure that the exact node of the target mesh is excited by its corresponding nodal force from the source, it is necessary to have a one-to-one mapping which means that the surface elements of the source mesh and the target mesh must use the same nodes. This can be achieved by using the mesh-mating capability in Simcenter 3D. It must be emphasized that vibration analysis such as frequency response and acoustic simulations are performed in the frequency domain. However, the nodal forces on the EM surface mesh are given as complex data in the time domain. Hence, a Fast-Fourier Transform is applied to convert the electromagnetic forces into the frequency domain. The FFT of the transient electromagnetic forces is performed for all surface nodes of the target mesh.

2.4.2 Structural Modeling

Prior to performing frequency response analysis (FR) on the target model, the usual first step in any vibrations problem is to study the behavior of the structure under unforced conditions. Running a modal analysis on the structure defined by the coupled equations of motion in (2.2a) helps to compute accurately and understand the frequency response results, especially when the oscillatory excitation approaches the natural frequency. The procedure for performing modal analysis has been articulated in Section 2.2.

Briefly, frequency response analysis is used to calculate the response of a structure to steady-state oscillatory excitation such as the electromagnetic forces of rotating electrical machinery. For a structure under periodic excitation, as in the case of the target mesh in Fig. 2.5, FR calculates the response of the target mesh by performing the structural analysis and changing a real transient domain into a static frequency domain using the magnitude and the frequency of the oscillatory loading, which is sinusoidal in nature. In its simplest case, the load is defined as having a particular amplitude at a specific frequency. Linear superposition of all single oscillation responses at each exciting frequency leads to the full response. The computed responses are usually vibrations, i.e., displacements, and accelerations, of the nodes as well as forces and stresses of the elements.

Most FEA software offer two main FR approaches: Direct Frequency Response Analysis (DFR) and Modal Frequency Response Analysis (MFR). In DFR, structural response is computed at discrete excitation frequencies by solving the set of coupled matrix equations of motion in 2.2a. The MFR, however, uses mode shapes of the structure to reduce and decouple the equation of motion when modal or no damping is used. Because the mode shapes are typically computed as part of characterization of the structure, MFR is a natural extension of structural modal analysis. The MFR form of the equation of motion can be solved faster than the DFR because the numerical solution is typically the solution to a set of smaller uncoupled single degree-of-freedom systems. Once the individual modal responses are computed, physical responses are computed as the summation of the modal responses. For this reason, larger models, in general, may be solved more efficiently with MFR. For small models with a few excitation frequencies, DFR may be the most efficient because it solves the equations without first computing the vibration modes. The direct method is typically more accurate than the modal method because it does not perform mode truncation but rather explores all the vibration modes of the electric motor within the audible frequency range.

2.4.3 Acoustic Modeling

To accurately evaluate the sound emitted by the IPM motor, a competent acoustic model must be developed. The finite element method uses one of two ways to achieve this objective. One way is to separately model the fluid mesh, and then apply the vibratory response of the stator structure as input to the acoustic mesh. The other way is to model the acoustic fluid around the existing stator structure so that the coupling between the fluid and structure can be used to map structural results (i.e., displacement, velocities, accelerations) into the acoustic mesh. The latter is more precise, realistic and offers deeper insight and has been applied to analyze the acoustic field around the IPM motor by following the steps described below.

Step I: Defining acoustic mesh elements

To simulate the exterior noise of the IPM motor, the process for generating the mesh that represents the acoustic fluid domain differs from the process for generating a mesh for EM and structural analysis. The acoustic meshes need to meet a different set of requirements. Typically, EM and structural meshes are too refined for acoustics analyses. Because the acoustic fluid can be very large, many mesh elements are required to adequately discretize the fluid domain. To ensure that the solve times are not too long, the acoustic mesh is optimized based on the input frequencies for the analysis. A direct relationship exists between the element size and the maximum forcing frequency which influences the selection of an optimal element size for acoustics analyses. The expression in (2.3) can be used to define the appropriate acoustic element size. In general, the element size should have the following attributes:

- Small enough to accurately mesh all regions of the model that are acoustically important. The element size in regions that are particularly critical to the analysis can be refined.
- Small enough to ensure the overall accuracy of the solution. For example, the element size should be fine enough to represent the distribution of vibration on the surface of the body.
- No larger than a certain fraction of the acoustic wavelength for the maximum frequency of interest. In general, a minimum of six elements per wavelength offers a reasonable compromise between solution accuracy and the overall size of the mesh.

$$\text{Element size} = \frac{\text{Speed of sound in the fluid medium}}{[\text{Max. frequency} \times \text{Elements per wavelength}]} \tag{2.3}$$

Step II: Defining fluid volume and non-reflecting boundary

Before defining the envelope that bounds the exterior acoustic fluid in Fig. 2.6, a 2D skin mesh is generated and wrapped around the 3D structural mesh which contains the nodal force load. This helps to derive an appropriate acoustic mesh from the existing structural mesh. The exterior fluid domain is defined using a convex 2D mesh. This mesh corresponds to the outer boundary of the fluid domain. The convex mesh surrounds the structural mesh, but it is not associated with the geometry itself. Hence, the convex mesh is not updated if the underlying geometry is modified. A convex mesh must be offset from the structural mesh to create the space for the fluid domain. The amount that the convex mesh is offset from the structural mesh affects the size of the fluid mesh. Ideally, the mesh should be large enough to accommodate a fluid mesh that is at least one or two elements deep in all directions from the structural mesh, but not large enough to prolong the solve time.

Next, a 3D fluid mesh is created to fill the air gap between the inner surface of the convex mesh and the outer skin mesh by discretizing the air component with 3D tetrahedral elements. Then, a special type of layer that acts like an acoustic absorber is created on the fluid surface. This layer is called an Automatically Matched Layer or AML. The AML boundary condition uses a reflectionless artificial layer that absorbs outgoing waves regardless of their frequencies and angle of incidence. The AML surface needs to be convex so that modal behavior between parts of a structure can be accounted for. The thickness of the AML determines its absorptive capacity. The use of AML obviates the need to use infinite planes to model a situation where the sound-radiating structure is located on a hard surface, such as the concrete floor of a semi-anechoic chamber.

Step III: Defining field points

A microphone mesh is also known as a field point mesh. Conceptually, microphones are sensors placed at locations to output acoustic quantities such as sound power, and sound pressure. You can request acoustic results on arbitrary locations exterior or interior to the fluid. These locations can be defined with 1D, 2D, or 3D microphone mesh. The microphone locations can be on any of the following:

- Exterior to the convex AML boundary;
- Interior to the convex AML boundary;
- On the convex AML boundary.

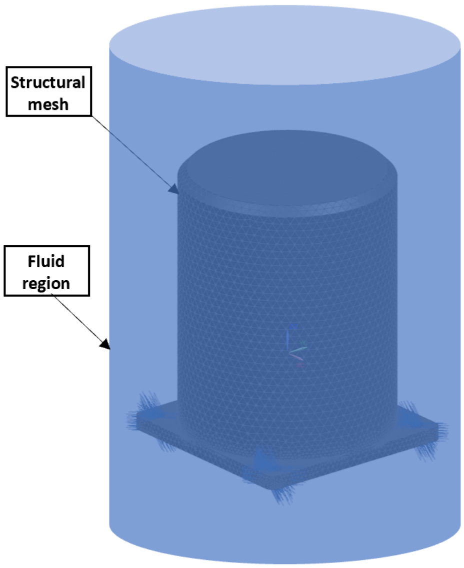

(a)

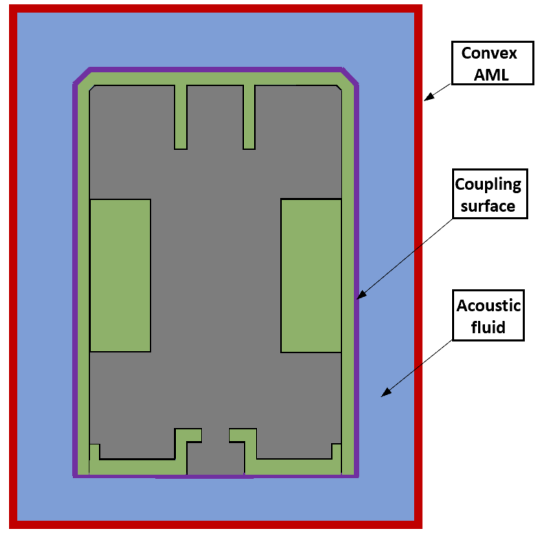

(b)

Fig. 2.6 (a) Acoustic fluid around IPM motor (b) A 2D schematic view.

When a microphone mesh is interior or on the AML, FEA solver interpolates the results from the fluid grids to the microphone location. However, when the microphone mesh is exterior to the AML, FEA solver uses the pressure and velocity on the AML and a boundary integral, to compute the results at the exterior microphone locations. 2D virtual microphones have been used in this thesis to capture the acoustic response at selected grid locations.

Step IV: Simulating the Acoustic Model Setup

The vibro-acoustic coupling interface given in (1.2) can be defined in one of two ways:

- **Two-way (strong) coupling**: That is, the vibration of the structure excites the fluid which in turn causes pressure loading on the structure.
- **One-way (weak) coupling**: Here, the effect of the fluid on the structure is assumed to be negligible. However, the vibration of the structure on the fluid is assumed to be significant.

Once step I to step III have been accomplished, the coupling between the fluid mesh and the structural mesh is defined in the simulation object. For electrical machines, the cynosure is the translation of the vibration on the stator structure into an acoustic signal. The rebound effect of pressure loading due to the fluid on the stator, however, is a subject of little significance in exterior acoustics. Hence, one-way coupling is selected in the simulation object. Then, a 3D vibro-acoustic solver is selected to simulate the one-way coupled model setup for the forcing frequency range of interest.

2.4.4 Results and Discussion

The models in Fig. 2.7 visualize the discretization and the flux density color map of the solved electromagnetic model. Fig. 2.8 shows the evolution of the electromagnetic force wave in the time domain. The normal components F_n and the tangential component F_t of the electromagnetic force wave in the frequency domain are presented in Fig. 2.9 for the first 100 modes. It is demonstrated in Fig. 2.9 that the most prominent harmonics of F_n are equal to the multiples of the number of poles, i.e., 4, 8, 12,... and so on. This trend applies to F_t harmonics as well with mode 4 being the most dominant component in the harmonic spectrum. For permanent magnet synchronous motors, the most dominant mode in the harmonic spectrum can be recognized by the GCD of the number of stator slots and the number of rotor poles. The zeroth mode is the DC component, which is not excited for the sinusoidal case. It is worth bringing to the fore that although the magnitude of F_t is negligible for all modes, it has been accounted for in the calculation. In most research works, F_t is often ignored due to its imperceptible impact on acoustic noise for small- and medium- sized motors, especially electrical motors rated below 1500 W.

Fig. 2.10 shows the modal analysis results for the first three (3) vibration modes of the 4Pole 24Slot interior permanent magnet motor. The 3D structural modal analysis has been realized using 36000 tetrahedral mesh elements. It took 10 minutes on the same workstation (Intel Xeon E5-1650 processor, 6 cores, 3.5 GHz, 32 GB RAM) to calculate the first 50 modes. Increasing the number of modes results in a more accurate structural representation of the motor, but concomitantly increases the computational burden. Since the normal hearing range for humans is between 20 Hz and 20 kHz, it is possible that not all of the computed modes are required. At a minimum, all the modes whose frequencies lie within the audibility range must be retained in the frequency response analysis.

The DFR results of the IPM motor are presented in Fig. 2.11. The 3D structural mesh is displayed in Fig. 2.11 (a) with fixed constraints applied to the base of the housing. Fig.

2.11 (b)-(d) displays the deformation of the motor at selected forcing frequencies, i.e., 120 Hz, 1000 Hz and 3200 Hz respectively. It is demonstrated from the color map in Fig. 2.11 (d) that the first vibration mode of the motor structure is most excited at a 3200 Hz forcing frequency. The vibrations at two (2) different locations on the case are visualized in Fig. 2.11 (e)-(f). Here, vibrations at the nodes are amplified due to the resonance phenomenon. It is also shown that resonance still occurs beyond 20 000 Hz. However, these vibrations are not perceived by the human ear because they are outside the audibility range.

The acoustic field around the IPM motor has been analyzed in Fig. 2.12. Here, the sound pressure levels have been requested from two 2D microphones. See Fig. 2.12 (a) for microphone locations. Microphone 1 is located on the AML and microphone 2 is situated 0.5 m away from the AML. The acoustic outputs from both microphones are illustrated in Fig. 2.12 (b)-(c) for the most sensitive frequency spectrum. It is demonstrated that the RMS value of L_p reading on microphone 1 is higher than the RMS value of L_p reading on microphone 2. That is, 54.8 dB and 28.6 dB respectively. The two RMS values corroborate the fact that as you move farther away from the radiating surface, L_p diminishes.

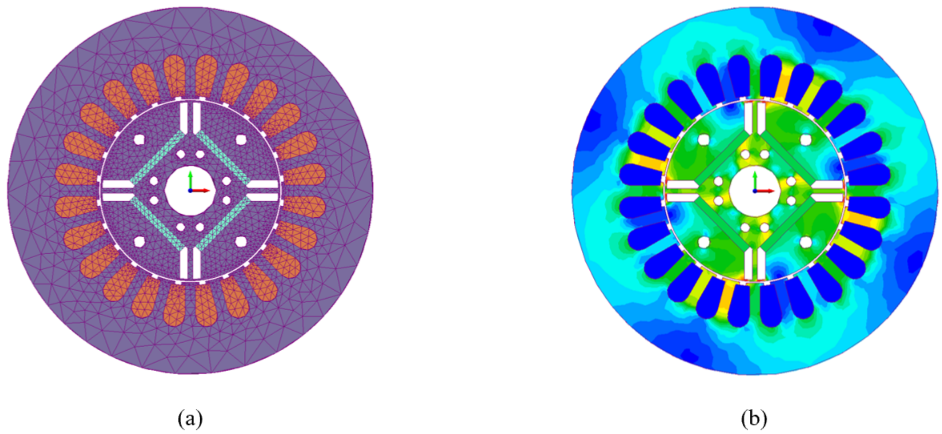

Fig. 2.7 (a) Stator 2D mesh in MAGNET (b) magnetic flux distribution.

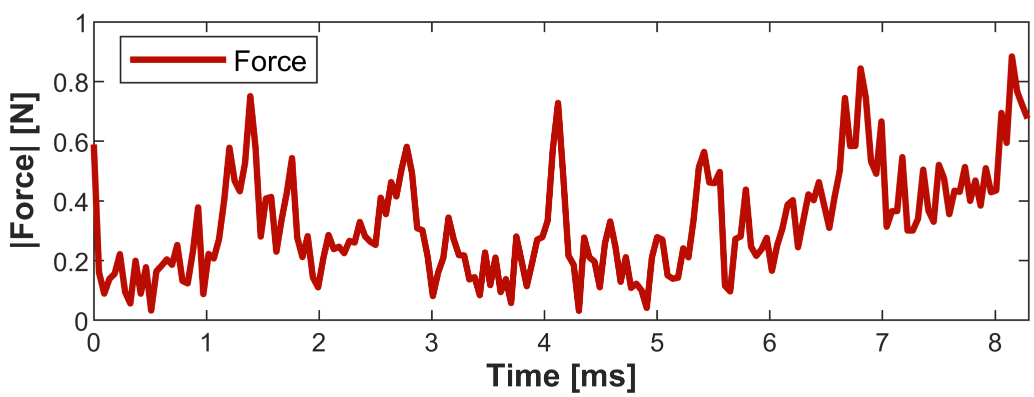

Fig. 2.8 Force vs. Time

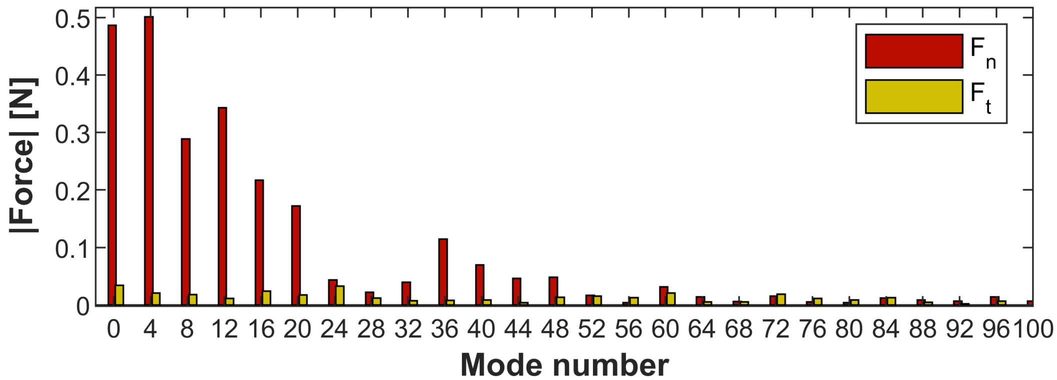

Fig. 2.9 Fast-Fourier Transformation (FFT) Analysis.

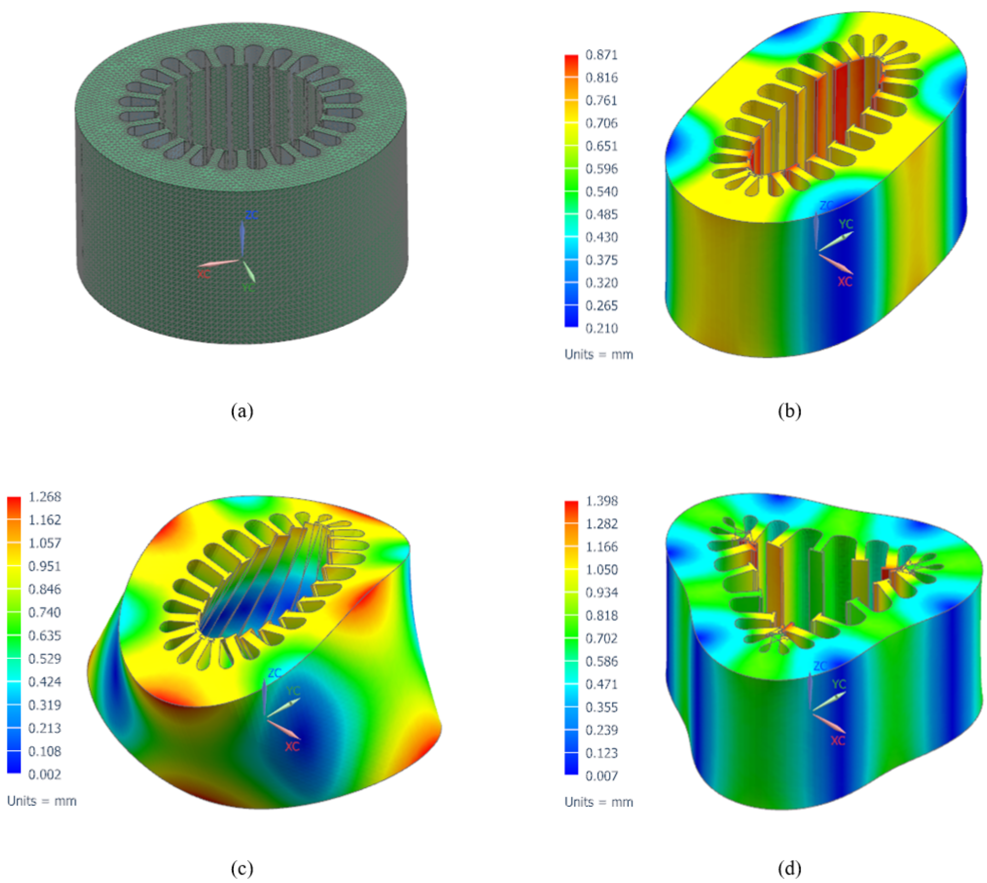

Fig. 2.10 4Pole 24Slot IPMSM Modal Analysis Results (a) Stator 3D Mesh (b) Mode 1 (3170 Hz) (c) Mode 2 (5401 Hz) (d) Mode 3 (8939 Hz).

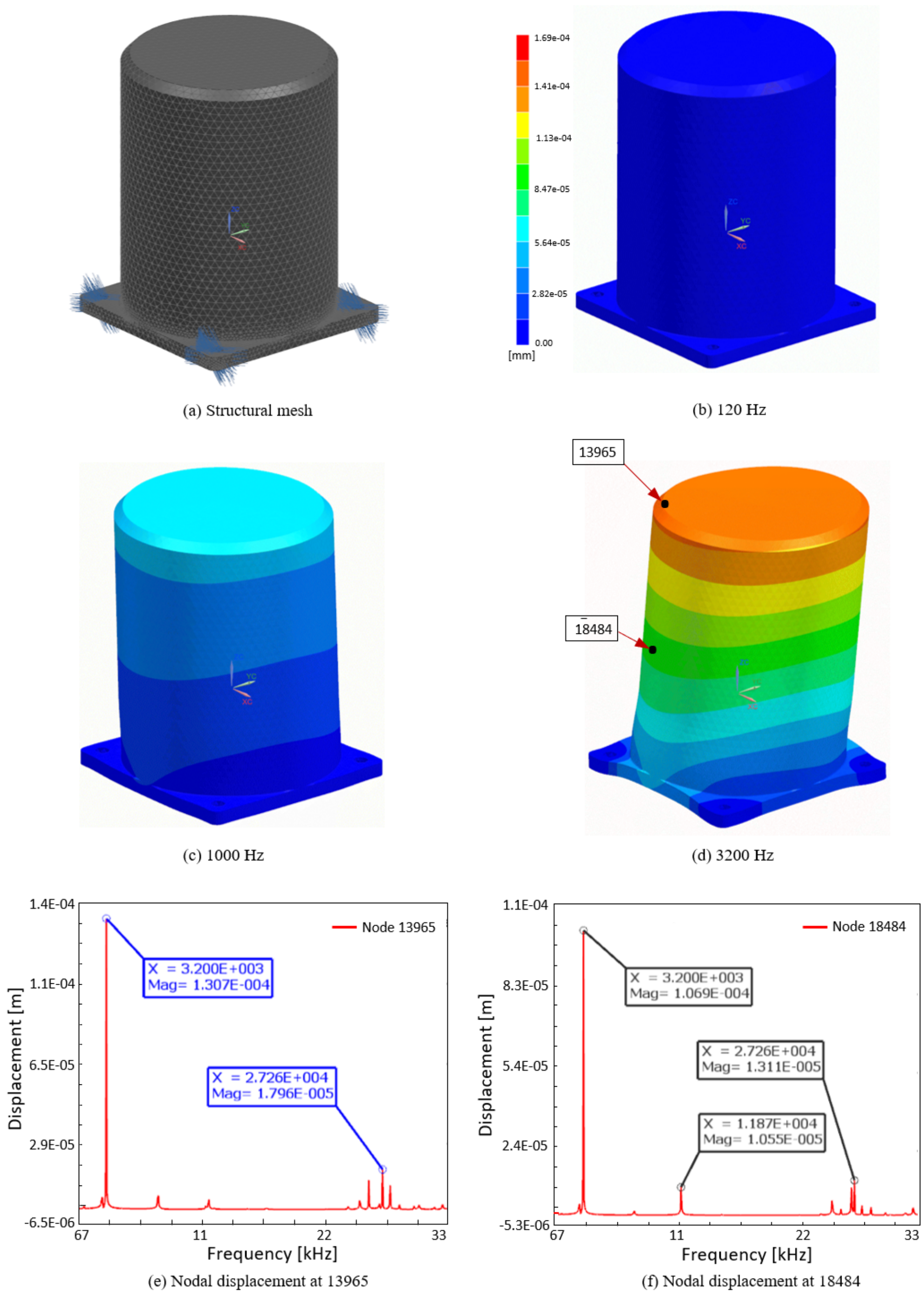

Fig. 2.11 (a) Target mesh (b) Motor deformation at 120Hz (c) Deformation at 1kHz (d) Motor deformation at 3.2kHz (e) Node 13965 vibration at 3.2kHz forcing frequency (f) Node 18484 vibration at 3.2kHz forcing frequency.

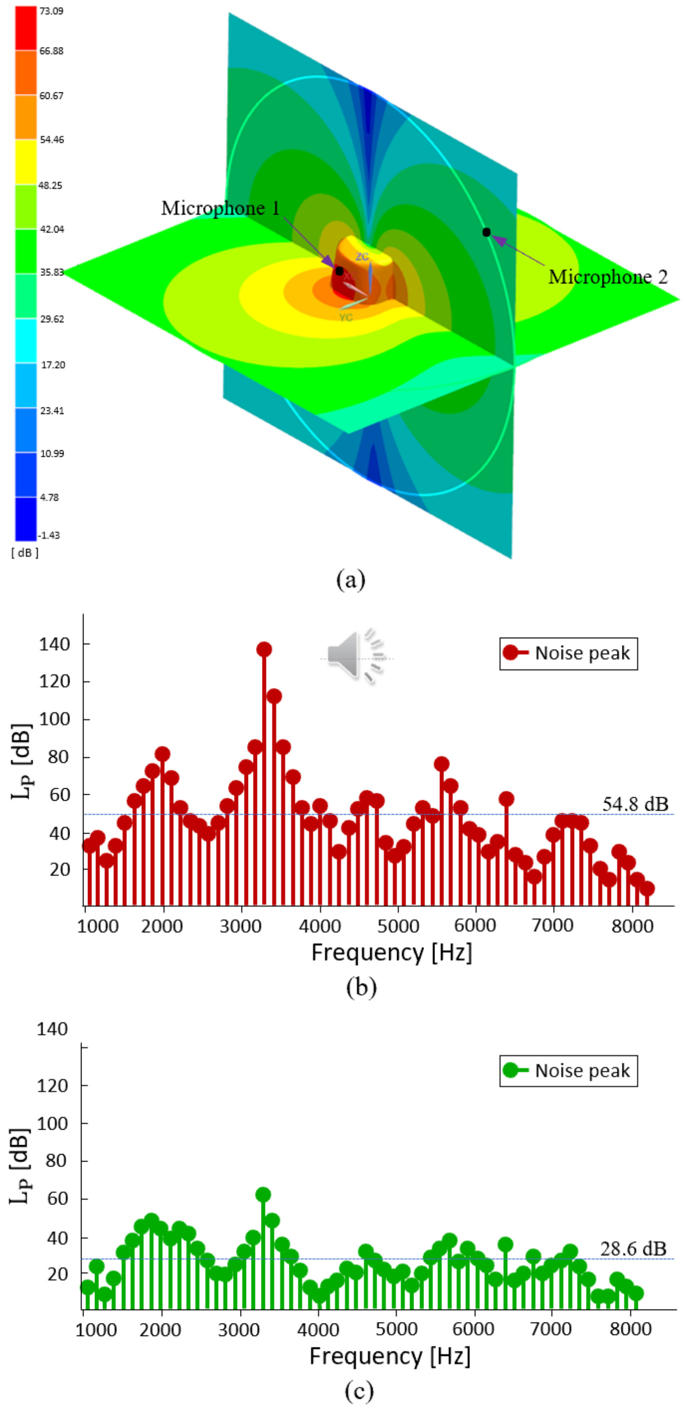

Fig. 2.12 (a) Acoustic field around the IPM motor (b) Sound pressure levels at microphone location 1 (c) Sound pressure levels at microphone location 2.

2.5 Summary of Modeling Challenges

Electrical machine noise has been studied extensively by a lot of researchers, and although the BEM and the FEM numerical techniques seem to work well in the literature, there are quite a number of software limitations for it to be applied in practice. For example, the calculated noise is almost always lower than the measured noise even at very low speeds. This is because we mostly focus on the low order harmonics. The noise measured experimentally gives the total noise due to all harmonics. The accuracy of the predicted acoustic noise depends not only on how accurate the model is, but also how accurate are the input data, e.g. level of current unbalance, influence of magnetic saturation, and higher time harmonics of the input current. These are sometimes difficult to predict. Other pertinent issues worth mentioning are discussed under the following headings:

2.5.1 Electromagnetic limitations

As the main source of acoustic noise, the electromagnetic forces must be calculated at all points on the stator by the finite element software. Meanwhile, the force waves are continually rotating. This makes it very difficult to accurately transfer the forces onto the structural mesh. Even the most accurate finite element programs introduce a lot of errors in these force calculations. Plus, the forces are usually calculated analytically in the post-processor module based on the magnetic flux density.

Several methods of handling the electromagnetic forces have been discussed in the literature. In [52],[42],[25], and [81], the electromagnetic force is equivalent to a single concentrated force exerted at the center of each stator tooth. However, the actual force is a non-uniformly distributed force. Because the concentrated equivalent method changes the distribution characteristics of the electromagnetic force wave, it induces extra error in the magnitude of the loaded force. According to the sampling theorem, the maximum electromagnetic force order that can be considered by the concentrated equivalent method is given by $n = \frac{Z}{2}$, where Z is the number of stator teeth for the interior-rotor machine. This means that the concentrated equivalent method ignores the force with a higher spatial order. In [82], the force interpolation method is used, but the approach is crippled by its inability to capture the non-uniformity in the force distribution. The calculation is improved by using the nodal force transfer method [83] which maps the electromagnetic mesh directly onto the structural mesh to preserve the uneven distribution of the electromagnetic force.

2.5.2 Structural limitations

The calculation of the mass and stiffness matrices seem trivial in FEM. However, the physical properties of the materials used in electrical machine design may not be known. The anisotropy of laminations, internal stresses caused by manufacturing, and the change in stiffness due to temperature variations cannot be modelled. Instead, the laminated stator core is modeled as a solid block. The copper coils are modeled as solid bars inside the slots with two rings added on both ends of the solid copper bars to account for the end windings. See Fig. 2.13 below for the conceptual models of the stator core and the coil system.

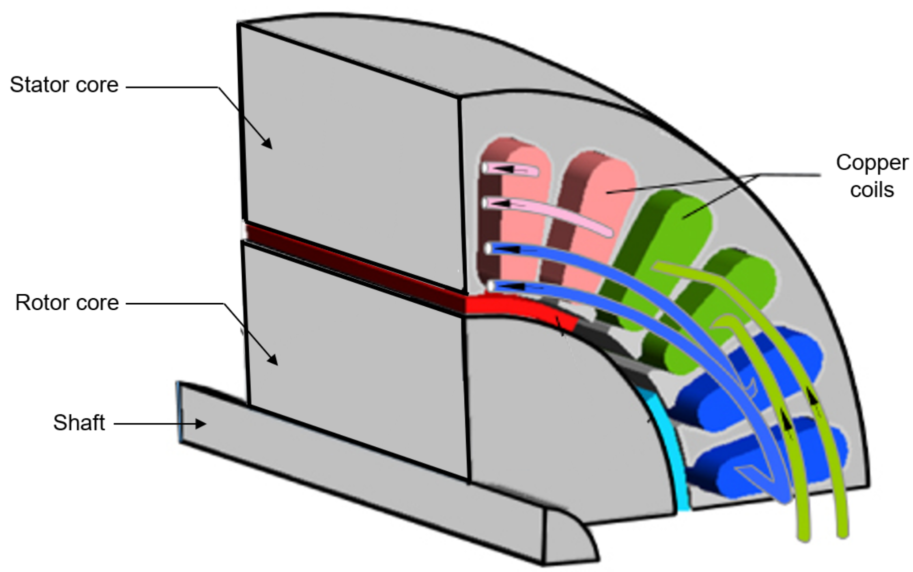

Fig. 2.13 Finite element models of the stator and coils [3]

At present, the best method to estimate the natural frequencies of the stator is to use numerical modal analysis. This is the only technique that can account for, with reasonable accuracy, the end bells, housing, rotor structure, mounting and so on. The natural frequencies and the vibration behavior of an electrical machine are significantly reliant on every part of the assembly and the way the machine is attached to the support system. Modeling the subtle nuances of the machine and applying the exact boundary conditions to capture the actual attachment circumstance can be very difficult, if not impossible.

Damping is also a major uncertainty factor when studying electromagnetically-induced noise of electrical machines. Briefly, damping means the ability of the structure to absorb vibrational energy due to internal friction. When an exciting force is equal or close to one of the natural frequencies of a structure, the amplitude of vibration is determined by the damping capacity of the structure. Therefore, it is necessary to consider the damping in calculating the amplitude of vibration. The damping matrix $[B_s]$ cannot be calculated theoretically. So, to obtain good values for the damping, one needs to use an experimental setup that is excited by various harmonic forces for estimating the frequency behavior of individual materials used in the structure. Unfortunately, these tests are difficult and expensive to perform. In FEA software packages, damping can be imposed as a constant damping value, or enforced as modal damping for each structural mode of the stator or rotor. This way, the results of an experimental modal damping analysis can be used in the simulation. Based on the author's experience, modal damping can vary from 0.5% to 4%. An average value of 2% is recommended in NVH simulation software packages.

2.5.3 Acoustic limitations

Computer-aided noise prediction is a powerful tool in the design and analysis of electrical machines. However, the quality of noise prediction depends greatly on the accuracy of the inputs. In particular, one challenge has always been obtaining the accurate electromagnetic force distribution when the input current system is non-sinusoidal.

In the past, machines were usually driven from either a DC or a sinusoidal AC supply. Recent developments in power electronics has provided more flexibility in the control of machines but at a cost of the supplies often being non-sinusoidal. The impact of non-sinusoidal supply waveforms on the multi-physics and acoustic performance of an electrical machine has been little investigated. The objective of the next chapter is to investigate the impact of such supplies on the acoustic performance of an electrical machine.

Chapter 3

Effect of Non-Sinusoidal Excitation on Acoustic Noise of Electric Motors

This chapter investigates the acoustic noise performance of the electrical machine when the electromagnetic model is excited with a non-sinusoidal current waveform as a result of a 3-phase pulse-width modulated (PWM) voltage source. Here, the machine is analyzed using the semi-analytical method discussed in Chapter 2. It is demonstrated that sampling the air gap space at a single time instant, which has been the routine procedure in the literature, can produce inaccurate acoustic noise values, especially when the motivation is to compare the emitted sound levels of two or more electrical machines.

To thoroughly understand the acoustic noise behavior of the electrical machine, this chapter proposes a time-instant sweep approach, referred to in this thesis as Multiple-Time Sampling (MTS) over the electrical period as an alternative to better analyze the emitted noise, regardless of the type of current waveform being fed into the stator winding. Additionally, two new acoustic quantities, i.e., Average Sound Power and Ripple Sound Power, have been introduced to accurately quantify the acoustic noise levels for varying switching frequencies of the power electronic drive circuit connected to the electrical machine.

The chapter is organized as follows: Section 3.1 discusses the motivation behind this work; Section 3.2 presents a brief description of the 4Pole 12Slot Interior Permanent Magnet Synchronous Motor as the reference model for this thesis; Section 3.3 discusses how the reference model is parameterized to vary the stator-rotor geometry of the electric motor across the design space; Section 3.4 uses the Latin hypercube sampling technique to build a design space with a reasonable number of coverage that offers enough detail without too much computational cost; Section 3.5 points the reader to the initial design and simulation assumptions that have been formulated to support the proposed methodology; Section 3.6 reviews the fundamental principles behind the power electronic drive system, where the Field-Oriented Control (FOC) scheme is implemented; Section 3.7 evaluates the multi-physics performance objectives and the effectiveness of the proposed MTS approach; Finally, Section 3.8 presents the multiphysics simulation results for discussion.

3.1 Introduction

Nowadays, pulse-width modulation is the most efficient way of controlling the speed of an electric motor. PWM operates like a switch which constantly cycles ON and OFF to regulate the amount of voltage across the terminals of the electric motor. The process of switching the device from one state to another is called *modulation*. When a switch is OFF there is practically no current, and when it is ON power is being transferred to the electric motor. This ON-OFF pattern can simulate voltages in between fully ON and OFF by changing the portion of the time the signal spends ON versus the time that the signal spends OFF. The duration of ON time is called *pulse width*. The term *duty cycle* describes the proportion of on time to the period (T) of time. Duty cycle is expressed in percentage. A low duty cycle corresponds to low power, because the power is off most of the time. A 100% duty cycle means that the power is fully on. In other words, the wider the pulsewidth, the more average voltage applied to the motor terminals, and the stronger the magnetic flux inside the armature windings. See Fig. 3.1 for a typical PWM waveform.

In the past, variable speed motor drives (such as a sewing machine motor) were controlled by implementing a rheostat connected in series with the motor to adjust the amount of current flow. It was an inefficient scheme, as this also wasted power as heat in the resistor element of the rheostat. While the rheostat was one of several methods of controlling power, a low cost and efficient power switching method was needed to drive motors for fans, pumps, and robotic servos etc.

The PWM technique emerged as a solution for controlling the amount of power delivered to an electric motor without dissipating power unnecessarily. However, PWM excitation causes an additional heating of motors, a large part of which can be attributed to iron loss. Worse, the pulsed voltage applied directly to the stator windings induces unpleasant audible noise in the electric motor. The output voltage and output current of PWM converters are non-sinusoidal. In other words, they contain higher time harmonics due to the switching operation. The shape of the PWM signal, the switching frequency and the modulation technique, all have considerable influence on acoustic noise. They can cause high tonality vibrations and acoustic noise that can be very disturbing to the human ear [3].

As mentioned earlier, the acoustic noise field around an electric motor is a cumulative effect of aerodynamic, mechanical and electromagnetic noise. Electromagnetically-induced noise, which is the most dominant component, is directly related to the power supply. Therefore, the type of current system that is fed to the stator windings can greatly influence the acoustic noise behavior of the electric motor.

To elucidate this point, a sinusoidal current and a non-sinusoidal current of equal RMS values have been used to excite the stator windings of the 4Pole 12Slot IPM motor. The results are presented in Fig. 3.2. At a glance, it is patently clear that the amplitude of the electromagnetic forces increased considerably for non-sinusoidal excitation with concomitant high tonality stator vibrations for the studied frequency range. For this reason, a noiseless electric motor fed with a pure sinusoidal current could become very noisy when supplied with a non-sinusoidal current waveform due to the switching phenomenon of the inverter circuit.

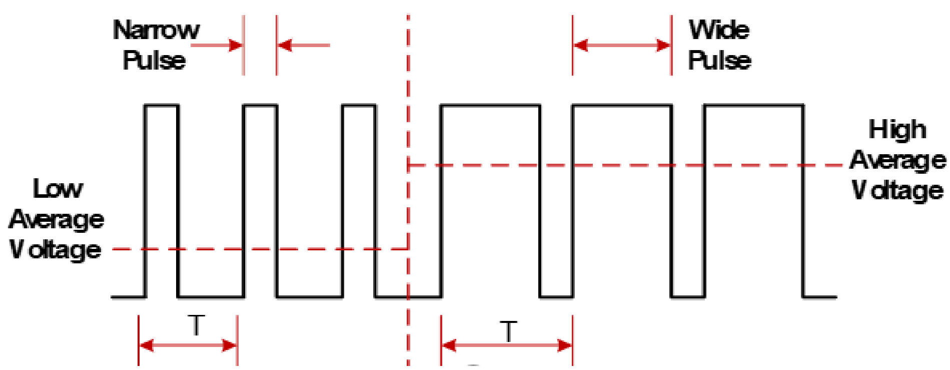

Fig. 3.1 Pulse-width modulated waveform.

PWMs have been studied extensively. However, their effect on noise has been mostly restricted to the drive's switching operation, with very little consideration of their interaction with the electrical machine itself. While previous works suggest that connecting filters to the inverter output terminals can remedy the PWM noise [84], not all the harmonics can be eliminated. Hence, there is still the possibility of having problematic harmonics

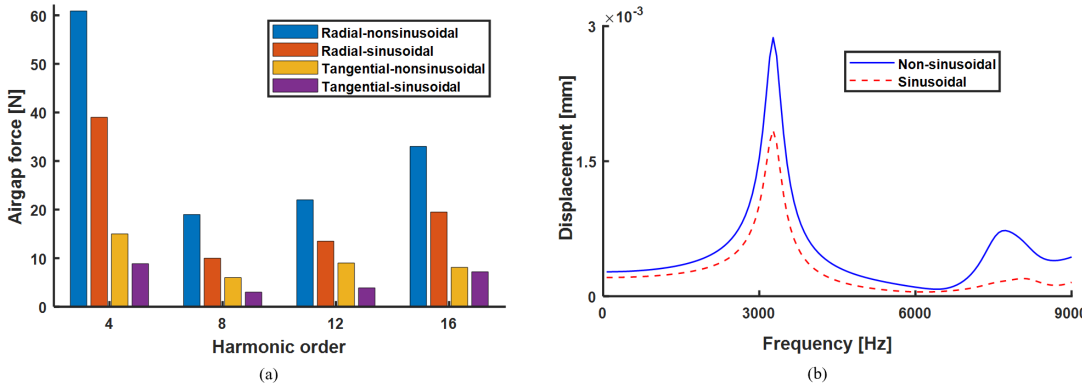

Fig. 3.2 Sinusoidal vs non-sinusoidal excitation (a) Electromagnetic force harmonics (b) Vibration response at selected node on the stator surface.

that can adversely influence the acoustic noise characteristics of the electric motor. In general, acoustic noise is caused by the least residual harmonics, which cannot be absorbed by output filters. Also, most investigated works have focused on sinusoidal cases. For a PWM-driven machine, only a few references exist in the literature. In [64], a full vibro-acoustic evaluation of the PM machine was conducted, where the current profiles and the acoustic quantities were related to a single design. Fang's work in [85] characterized a similar behavior of a PWM-controlled powertrain with focus on the gear meshing forces. The authors in [86] examined an inverter-fed induction motor and studied the influence of the coupling environment.

3.2 The Reference Model: A 4Pole 12Slot Interior Permanent Magnet Synchronous Motor

PMSMs have been widely used as the driving core in electric vehicle applications due to their high-power density and high efficiency. This chapter and beyond, focuses on a custom-built 4Pole 12Slot Interior Permanent-Magnet Synchronous Motor. This working prototype, displayed in Fig. 3.3, is available at the CEMLab [87]. The design specifications are provided in Table 3.1. The motor has an output power rating of 275 W which perfectly fits into the category of electrical machines whose electromagnetic noise component dominates the acoustic field [24]. The motor is rated with a Class A insulation material which means that the motor must not be operated beyond 105°C, otherwise the insulation system can breakdown [88]. For this reason, the maximum operating temperature is limited to 100°C. See NEMA's recommendation for selecting the appropriate insulation materials. The list is provided in Appendix C.2.

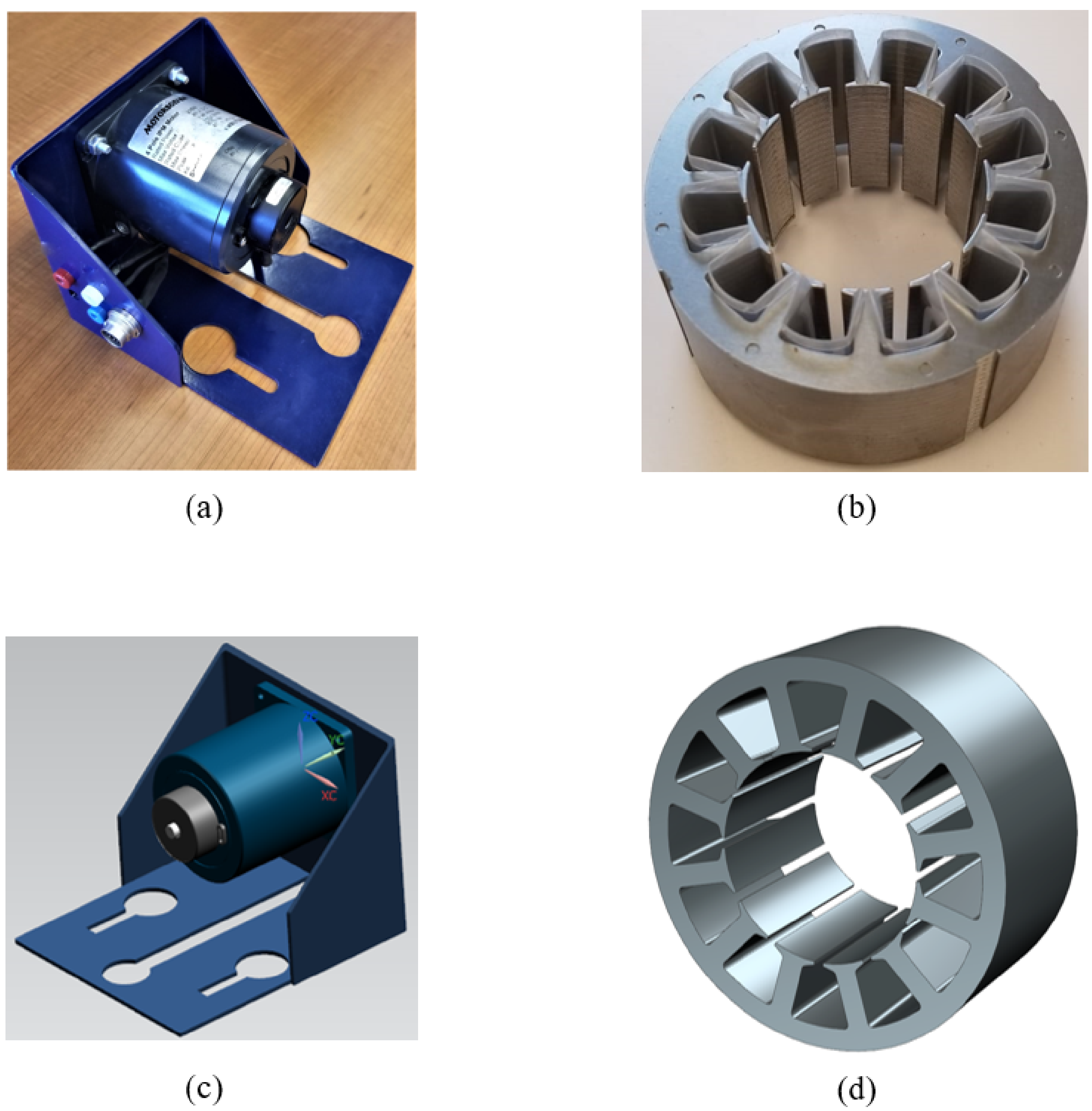

Fig. 3.3 A 4Pole 12Slot IPMSM: Actual model (a, b), CAD model (c, d).

Table 3.1 Design Information

Parameter	**Value**
Number of poles	4
Number of slots	12
Supply voltage	42 V
Rated current	7.85 A
Rated speed	1000 RPM
Core material	M-19 26 Ga
PM material	NdFeB 32/16
Coil material	Copper: 100 % IACS
Rotor core mass	0.225 kg
Rotor magnet mass	0.0627 kg
Stator core mass	0.446 kg
Stator winding mass	0.364 kg
Rotor inner diameter	11 mm
Rotor outer diameter	40.00 mm
Stator outer diameter	75.00 mm
Stack length	34.0 mm
Back-iron thickness, x_1	4.40 mm
Tooth width, x_2	4.44 mm
Tooth-tip thickness, x_3	0.63 mm
Slot-opening width, x_4	0.19 mm
Airgap thickness, x_5	0.50 mm
Magnet offset, x_6	8.40 mm
Magnet orientation, x_7	25°
Magnet thickness, x_8	3.00 mm
Magnet width, x_9	10.25 mm
Magnet top gap width, x_{10}	1.20 mm
Winding Connection type	Y (star)
Winding phase resistance	0.138 Ωm
Coil fill factor	41.50%
Coil separator thickness	0.50 mm
Number of turns	28
Turn length	186 mm
End winding outer diameter	65.20 mm
End winding height	19.50 mm
End winding resistance	0.0876 Ω
End winding inductance	43.71 H

3.3 Parameterization of the CAD Geometry

Once the CAD models of the 4Pole 12Slot IPM motor have been created using the design process delineated in Chapter 2.3, the next step is to parameterize them. Parameterization helps reduce the time spent on model abstraction and geometry editing. This convenience obviates the arduous, if not impossible, task of having to create thousands of different designs manually.

The general guideline to parameterize an electric motor is as follows: first, the design variables are divided into dependent and independent variables. For the 4Pole 12Slot IPM motor, the dependent variables have been labeled $\mathbf{x}_1$ to $\mathbf{x}_{10}$ and highlighted in Fig. 3.3. These variables have been carefully selected based on the leading noise-sensitive design variables reported by [75] and [89]. All other design variables that are not included in this list form part of the independent set.

Next, all the dependent design variables are tied to mathematical expressions that do not violate the geometric- and physics-based constraints of the base model. When the design topology changes, all the design variables (including meshes, loads and boundary conditions) that are directly associated with the base model are automatically updated.

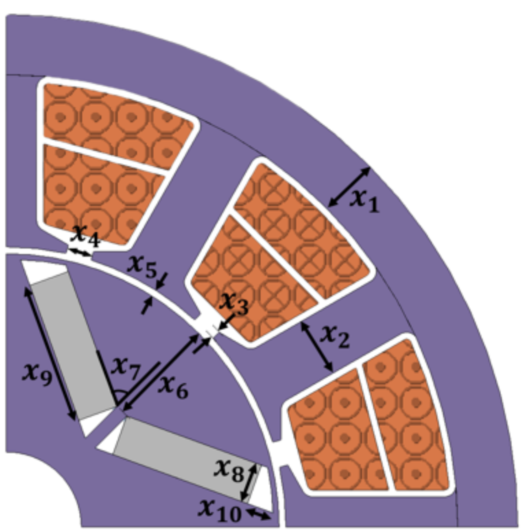

(a)

Lb	x	Ub
2.2 mm	x_1	6.6 mm
2.22 mm	x_2	6.66 mm
0.32 mm	x_3	0.95 mm
0.10 mm	x_4	0.29 mm
0.25 mm	x_5	0.75 mm
4.2 mm	x_6	12.6 mm
12.5°	x_7	37.5°
1.50 mm	x_8	4.5 mm
5.13 mm	x_9	15.3 mm
0.38 mm	x_{10}	1.13 mm

(b)

Fig. 3.4 (a) A $\frac{1}{4}$ 2D electromagnetic model parameterized in MAGNET (b) The lower bound (Lb) and the upper bound (Ub) of geometric design variables.

3.4 Creating the Design Space

Prior to performing the multi-physics simulations, the design space of the electric motor must be filled with samples. A space-filling sampling plan, also called design of experiments (DoE), is a strategy for allocating samples in the design space that aims at maximizing the amount of information that is required to perform a particular experiment. To choose an appropriate method for the experiments usually involves an assessment of the intended use of the results, the prior knowledge one has about the problem to be analyzed (such as the presence of noise and the function structure) and other restrictions related to the availability of samples and time [90].

Design of experiment techniques have been studied extensively in the literature for their applicability, strengths, and weaknesses. The most popular ones include Latin Hypercubes, Hammersley Sequences, and Uniform Designs. The Latin hypercube sampling (LHS) is the most convenient, and widely used, sampling plan for deterministic computer experiments. A brief description of the aforementioned sampling plans is presented in Appendix C.3, with the aim of showing some of their main strengths and weaknesses.

Latin hypercubes have been used to populate samples in the design space of the IPM motor. The Latin hypercube applies the minimax criterion to arrange the samples to be uniformly scattered in the design space. A list of motor designs (each motor design comprises the 10 dependent variables arranged in a particular pattern) was generated using a uniform distribution. However, after applying design constraints to check for structural feasibility, not all the permutations were found to be feasible. The list was pruned to remove all impractical design permutations. Next, close neighbors within a specified distance in the design space were also removed to ensure uniqueness of each design geometry. As a result, the distribution of the design variables were not necessarily a uniform distribution. In total, 1000 structurally reliable motor samples were retained for the studies and passed to the finite-element solvers.

3.5 Modeling Assumptions

The 4Pole 12Slot IPM motor, like any other electrical machine, is composed of intricate parts and components that can be very difficult, if not impossible, to replicate using computer software without making certain assumptions. It must be stated that the following assumptions have been incorporated in the design and the finite element simulations.

3.5.1 Geometric assumptions

Both the stator and rotor are geometrically symmetrical. For all practical electric motors, there is some degree of rotor eccentricity mainly due to tolerances and imperfections during manufacturing. Although this can be handled in the modeling, eccentricity has not been considered. The reason being that eccentricity distorts the periodicity of the electromagnetic forces making it impossible to simulate partial models of the reference geometry. The use of partial models reduces the time associated with solving a large number of motor samples. Also, the stator core is built of laminated, electrical steel, and the windings are made of thin strands of copper coils, which are very difficult to replicate in FEM models. For this reason, both the stator and coils are modeled as a solid block. The copper coils are modeled as 12 solid bars, well packed inside the stator slots. The equivalent end-windings have also been modelled as a solid ring and added to both ends of the stator coils.

3.5.2 Electromagnetic assumptions

The component of acoustic noise being considered is the electromagnetic noise. The excitation strategy is a pure sinusoidal current at rated condition, applied to the 3-phase stator winding. A 2D electromagnetic-field analysis has been performed with the assumption that there are no geometric skews. Briefly, skewing introduces an axial magnetic force variation and can therefore excite longitudinal structural modes of the stator and rotor structures. It can also create additional axial thrust. For electric motors rated below 1.5 kW, the tangential component of the electromagnetic forces can be ignored since they do not have significant acoustic noise effect on radial flux machines [91].

3.5.3 Structural assumptions

Since the focus is on the establishment of trends and not in the absolute values of the sound power, only resonances in the stator structure are used. Hence, only the stator and winding are modeled. By virtue of the rotor's position, i.e., confined inside the stator, its contribution towards exterior acoustics can be neglected. Besides, rotor vibrations can be ignored for speeds below 120 000 RPM [92].

As mentioned earlier, damping is a major uncertainty when calculating electromagnetically-induced acoustic noise. It depends on several factors including winding impregnation, winding type, insulation type, operating temperature and so on. The larger the damping, the lower the vibration and resulting acoustic noise. To be able to improve the NVH simulation results, empirical damping values must be used. Experiments to measure the damping values of the stator assembly are normally very difficult to perform. Hence, the theoretical modal damping equation [3], often used in the literature, which describes damping of a specific structural mode has been used in this work.

3.5.4 Acoustic assumptions

The stator is the main originator of acoustic noise and it has been considered as a cylindrical radiating surface. This permits the sound power level calculations to be performed using the semi-analytical formulations given in (A.7) to (A.9).

3.6 An Overview of Motor Drive Systems

Unlike line-start applications where a constant supply voltage and frequency are applied, an adjustable power supply is needed to reach different torque and speed levels. The integrated motor drive offers this flexibility by means of control techniques to regulate both the supply voltage and the frequency levels. Among all the existing control techniques, the closed-loop field oriented and direct torque controls are the most commonly used in the industry. More precisely, the field-oriented control (FOC) of multi-phase machines is often preferred over the other techniques due to the ease of implementation as well as reliability. A diagram of an FOC drive is shown in Fig. 3.5, which consists of three main parts:

- Control unit;
- Inverter circuit;
- Electric motor.

The inverter works in conjunction with a DC voltage source and a pulse width modulation technique. The control circuit consists of proportional-integral (PI) controllers as well as the dq0-to-ABC transformation matrix used to translate the drive input, i.e. the reference speed (ω_{ref}), to the three-phase PWM voltages. By converting the DC bus voltage into phase voltages using an appropriate switching technique, the inverter can effectively drive the motor at a particular switching frequency and modulation index [93]. Both the voltage magnitude and frequency can be controlled as functions of the reference speed and the motor load. The underlying principles along with the inner physics of the control-drive circuit are explained in Appendix C.

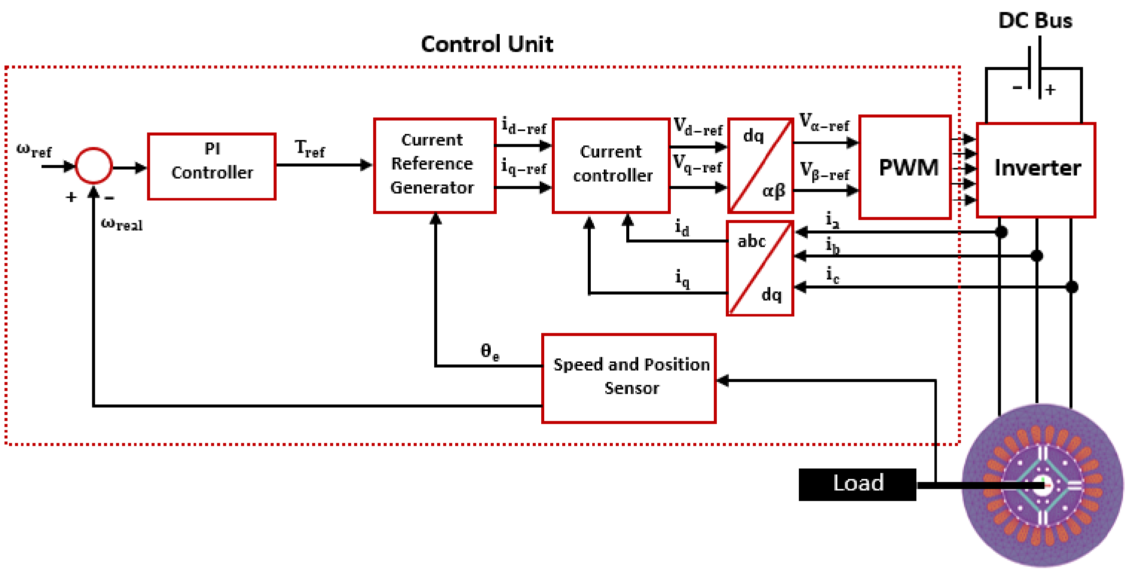

Fig. 3.5 Closed-loop field-oriented control technique

3.6.1 Modulation Index

For any PWM scheme, it is important to introduce metrics that quantify a PWM signal's quality. For this purpose, three are generally defined in the literature [94]: $\mathrm{m_a}$ is the amplitude modulation index in (3.1), $\mathrm{m_f}$ is the frequency modulation index in (3.2) and THD is the total harmonic distortion in (3.3). Here, $\mathrm{V_{LL_1}^{peak}}$ is the peak of the fundamental harmonic of the line-to-line PWM voltage, $\mathrm{V_{dc}}$ is the DC bus voltage, $\mathrm{f_{sw}}$ is the switching or carrier frequency, and $\mathrm{f_1}$ is the fundamental or modulation frequency. The numeric subscripts signify the harmonic numbers.

$$\mathrm{m_a} = \frac{\mathrm{V_{LL_1}^{peak}}}{\mathrm{V_{dc}}} \tag{3.1}$$

$$m_f = \frac{f_{sw}}{f_1} \tag{3.2}$$

$$THD = \frac{\sqrt{V_2^2 + V_3^3 + V_4^4 + \cdots}}{V_1} \tag{3.3}$$

3.7 Multi-Physical Simulations

The 4Pole IPM motor connected to a 2-level 6-switch space vector modulated IGBT inverter is analyzed to provide simulation guidelines for this study. The design process of the control-drive system is discussed by Ghorbanian in [95]. The corresponding design parameters are the same as in Table 3.1. One-thousand motor structures were used and each sample was run with 1 level of DC bus voltage and 4 levels of f_{sw}. This 1×4 combination yielded 4000 total samples.

3.7.1 Creating Unsolved DQ Models for Pre-Processing Step

Each motor sample consists of the flux linkage, d-axis inductance, q-axis inductance, winding resistance and cogging torque models. Since computing the cogging torque does not require the drive circuit connected to the motor, the corresponding model is solved in the pre-processing stage of simulations. Therefore, there are 1000×5=5000 models required for building 1000 nonlinear DQ models of the IPM motor.

All the DQ models are simulated on one PC (Intel Xeon E5-1650 CPU, 6 cores, 3.5 GHz, 32 GB RAM). Creating the DQ models took 22.5 minutes and the unsolved models size was 0.35 GB. The simulation times for the solved pre-processing DQ models are shown in Table 3.7.1.

Table 3.2 Pre-Processing Models Handled By MagNet

DQ Parameter	Simulation Time	Storage Size
Flux linkage (F_L)	14 min	0.29 GB
Cogging torque (T_c)	28 min	0.40 GB
Stator resistance (R_s)	13 min	0.29 GB
d-axis inductance (L_d)	28 min	1.25 GB
q-axis inductance (L_q)	29 min	1.25 GB

3.7.2 Simulink-based Motor Drive Simulation

It must be emphasized that there are 1000 samples, which are run at 4 different values of frequency modulation index (i.e., 9, 15, 21 and 27) and one level of V_{dc}. Therefore, there are 4000 motor drive models available. Once the values of the flux linkage, cogging torque, stator resistance, d- and q-axis inductances are extracted from the solved DQ models, the values are transferred to the motor drive system to simulate the currents for every sample. The currents are shown in Fig. 3.6 for different m_f values. The higher the m_f value, the closer the signal quality gets to the fundamental sinusoid.

The motor drive system is implemented in the Simulink environment and it consists of an electric drive circuit similar to Fig. 3.5, which is connected directly to a corresponding DQ model. The input to the drive circuit was the rotor speed and the magnetic flux. Using the same PC (Intel Xeon E5-1650 CPU, 6 cores, 3.5 GHz, 32 GB RAM), the storage size and the time required for solving the DQ models are 4.15 GB and 2344 minutes respectively.

3.7.3 Post-Processing Multi-Physics Simulations

This section outlines how the multi-physics performance objectives (i.e., magnetic pressure, stator natural frequencies, stator vibrations and the sound power levels) are evaluated for different m_f values using a combination of finite element and analytical means.

Electromagnetic Field Analysis

At steady state, the last cycle of currents for each design are extracted and applied to the electromagnetic model to simulate the electromagnetic-field objectives. The simulation step is summarized as follows: First, a transient 2D solver is selected and the simulation is performed for one electrical cycle. The MTPA control scheme is used for all 1000 samples. As done in previous chapter, a quarter model is simulated by applying symmetric boundary conditions at the quadrature surfaces to reduce the solve time. It took 38 hours on an the same Intel Xeon E5-1650 processor to simulate 1000 partial samples for different m_f values. Once the flux densities, B_n are found, the air gap space can be sampled at any time instant to calculate the normal magnetic pressure waves, P_n, as in (3.4). Here, μ_0 is the vacuum permeability constant, and the tangential flux density, B_t, has been ignored due to its negligible contribution to acoustic noise [91] for small- and medium-sized motors.

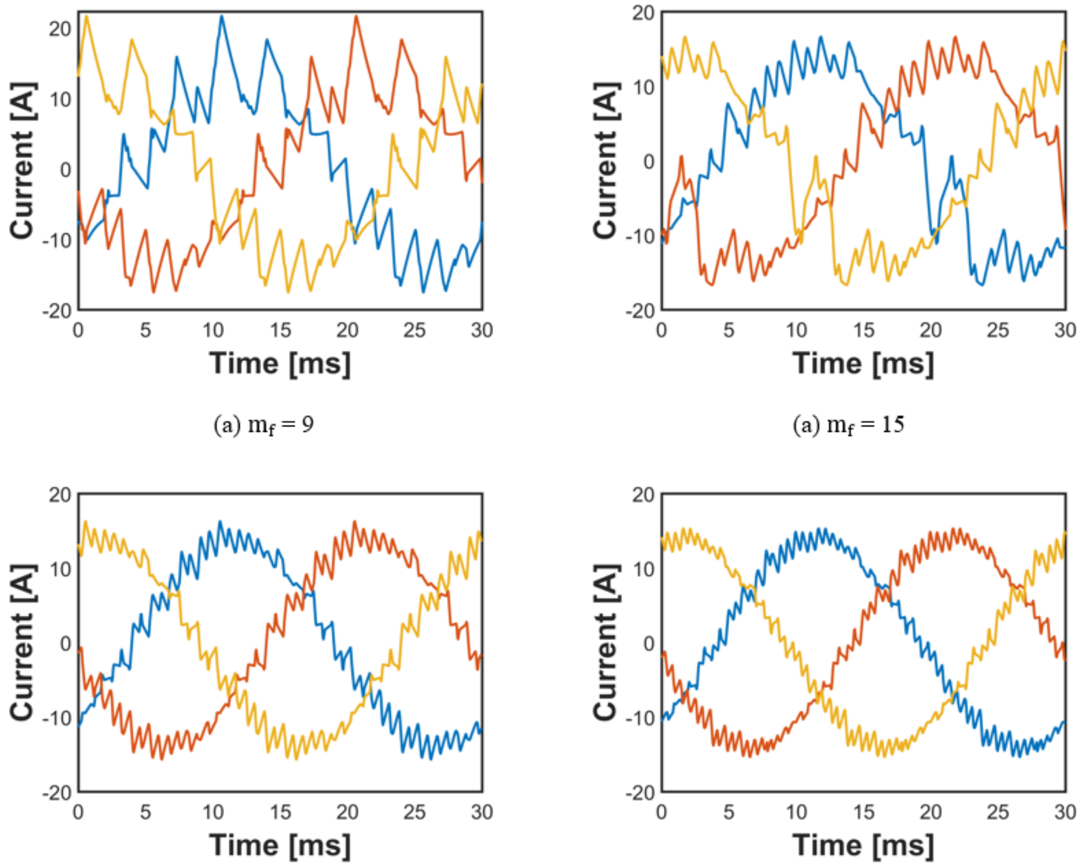

(a) $m_f = 9$ (a) $m_f = 15$

(a) $m_f = 21$ (a) $m_f = 27$

Fig. 3.6 PWM current waveforms for different modulation indices

$$\mathrm{P_n}(\theta) = \frac{1}{2\mu_0}\left[\mathrm{B_n^2}(\theta) - \mathrm{B_t^2}(\theta)\right] \approx \frac{1}{2\mu_0}\left[\mathrm{B_n^2}(\theta)\right] \tag{3.4}$$

Structural Modal Analysis and Sound Power Calculation

Once the airgap magnetic forces are extracted, 3D modal analysis is performed to determine the natural frequencies for all samples. For the structural 3D mesh with around 14,000 tetrahedral elements in Fig. 3.7, it took 8 minutes per sample on the same workstation to calculate the first 10 modes. The calculated modes, i.e., mode 1 to model 10, were enough to cover the audible frequency range for humans.

After the electromagnetic and structural simulations, the analytical formulations in

Section A.5.1 have been used to evaluate the P_{SL} for every sample. The normal magnetic pressure, P_n, and the resonant frequencies, f_s, are used in (A.7) to calculate the stator displacements, A_{mr}. The sound power, P_S (in Pascals), and the P_{SL} (in decibels) emitted by the electric motor into the surrounding air are computed by using (A.8) and (A.9).

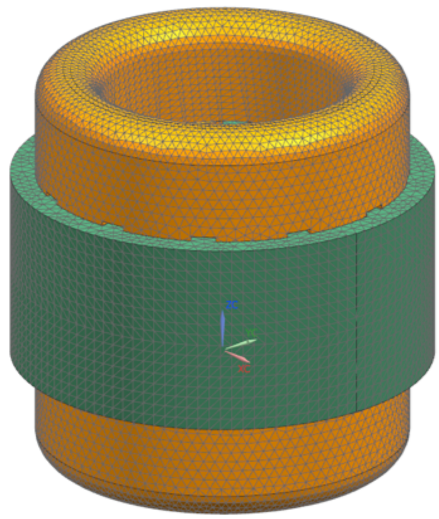

Fig. 3.7 4Pole 12Slot IPM Stator Mesh

3.7.4 Multiple-Time Sampling Approach

In earlier works [96], [97], the calculation of the acoustic noise has been performed using single-time sampling. For example, the last time instant in a transient simulation was selected in [97]. While this method works for purely sinusoidal excitations, it may not yield desirable results for the PWM. This is because the current waveforms shown in Fig. 3.6 consist of time harmonics and ripples which correspondingly affect the airgap flux densities at each time instant. In other words, if a single time instant is selected from the waveforms in Fig. 3.6, then the 3-phase currents at that time instant are not necessarily the same for different f_{sw} or m_f values. This time variation affects the magnetic flux densities and the magnetic forces in the airgap space. Therefore, focusing on only one time instant ignores significant PWM harmonics in other instants which can impact the overall sound power level. To address this issue, multiple-time sampling (MTS) is proposed to better analyze the acoustic noise of the electrical machine fed with non-sinusoidal currents.

First, the normal component of the airgap flux densities, B_n, is extracted for different time instants in one electrical period. In each time instant, the magnetic pressure wave, P_n, is evaluated using (3.4). For this particular IPM motor, 108 time instants were found to contain all the most important P_n values. Second, P_n at each instant is decomposed into spatial harmonics by applying a FFT. Lastly, the spatial harmonics of P_n for all time instants are used to evaluate the time-domain sound power level, P_{SL}, over one electrical period using (A.7) - (A.9). In Fig. 3.8, the dominant harmonics of the magnetic pressure wave are shown for only three time instants for the 4Pole 12Slot IPM motor. These harmonics correspond to the multiples of the number of poles. For PWM operation, the 0^{th} mode is also excited. It is clearly observed that at each time instant, the P_n harmonics do not remain constant as it is usually assumed which justifies the reason for using the Multiple-Time Sampling analysis approach.

3.8 Results and Discussions

Fig. 3.9 shows the normal flux density distributions for the prototype model at the studied m_f values at a single-time instant for a quarter of a mechanical revolution. Compared to the sinusoidal case, generally, for lower m_f values, the flux densities are higher due to the time harmonics of the currents shown in Fig. 3.6. On the other hand, this growth is less prominent for higher m_f due to the improvement in signal quality. A similar trend holds for different time instants.

To provide more insight into the effect of MTS, the harmonic amplitudes of P_n were analyzed with all 108 time instants for all samples. This is demonstrated with the help of error bars shown in Fig. 3.10. For every m_f case, the error bars represent the max-min variation of the P_n amplitudes for all time instants. Note that the error bars shrink for higher m_f values due to smaller PWM harmonics. Also, the variation of the mean values for all spatial harmonics is shown, and is approximately the same for all m_f cases.

The acoustic field of a selected sample is presented in Fig. 3.11 to demonstrate the efficacy of MTS. The instantaneous P_{SL} waveforms for m_f = 9 and m_f = 27 have been generated by sampling the airgap using 108 time instants over the electrical period. And by visual inspection, it can be observed that P_{SL} values for both m_f cases are either similar or fluctuate when the airgap space is sampled at random. For example, while the P_{SL} values (about 53.22 dB and 53.23 dB respectively) for their last time instants are almost equal, for the k^{th} time however, where the waveforms carry prominent time harmonics, P_{SL} values (54.95 dB and 53.31 dB for $m_f = 9$ and $m_f = 27$ respectively) differ. Clearly, each time instant expresses a portion of the acoustic behavior and cannot be relied upon as a basis for comparing P_{SL} waveforms for varying m_f values. Hence, an alternative that accurately represents the acoustic design space by taking full account of the P_{SL} must be sought. By using MTS, the airgap space is explored fully by increasing the sampling rate to account for all crucial magnetic forces. Then, P_{SL} is evaluated and propagated over the full range of the electrical period. Since the P_{SL} is now time varying, two new acoustic metrics, defined in (3.5) and (3.6), are introduced to accurately characterize the P_{SL} of the IPM motor.

$$P_{SL}^{avg} = \frac{1}{N}\sum_{i=1}^{N} P_{SL}^{i} \tag{3.5}$$

$$P_{SL}^{rip} = \frac{\max[P_{SL}] - \min[P_{SL}]}{P_{SL}^{avg}} \tag{3.6}$$

Here, P_{SL}^{avg} and P_{SL}^{rip} are the average and ripple sound power levels respectively. P_{SL}^{i} is the sound power level at the i^{th} time instant and N is the number of time samples per electrical period. The average P_{SL} is determined by the magnitude of the fundamental sinusoid, which does not change for varying m_f values. Hence, P_{SL}^{avg} can be used as a basis for comparing the noise levels for different m_f. In other words, the variance around P_{SL}^{avg} is mainly due to the time harmonics. In Fig. 3.11, P_{SL}^{avg} are 53.36 dB and 53.41 dB respectively for both m_f values. These values are expected to be close due to the reason above.

The ripple P_{SL}, as the name implies, quantifies the percent ripple sound power, which gives an indication of the variations in the noise signal. Ripple sound power was found to be 7.7% and 3.6% with respect to the average for both m_f cases (max-min values for $m_f = 9$ are 54.98 dB and 50.88 dB, and 54.37 dB and 52.47 dB for $m_f = 27$). This has been extended to investigate all samples in Fig. 3.12. In Fig. 3.12 (a), 4 histograms are shown for P_{SL}^{avg} for all samples and for 4 m_f scenarios. The overlap is due to the fundamental sinusoid which is relatively constant. In Fig. 3.12 (b), P_{SL}^{rip} is seen to depreciate with increasing m_f values for all samples. For $m_f = 9$, a broader right-skewed ripple noise is observed, while m_f values of 15-27, do not reveal any noticeable trends due to the mutual semblance in PWM quality as seen in Fig. 3.6. For the four m_f values, it was observed that there was no correlation between P_{SL}^{avg} and P_{SL}^{rip}. The correlation coefficient was below 0.22 for all modulation indices. Hence, P_{SL}^{avg} and P_{SL}^{rip} can be considered as independent objectives.

3.9 Conclusions on the Effect of Non-Sinusoidal Excitation

The coupled multi-physics simulation framework presented in Section 3.7 was used to evaluate the NVH behavior of the electrical machine. Using the 4Pole 12Slot Interior Permanent Magnet Synchronous Motor as the reference model, 1000 variants of the IPM motor were numerically and analytically analyzed. It was demonstrated in the simulation results shown in Fig. 3.9 and Fig. 3.10 that the electromagnetic force profile is immediately impacted by the quality of the current waveform fed into the electrical machine. The magnitude of the electromagnetic force harmonics were significantly different at every sampled instant of the airgap space. The concept of Multiple-Time Sampling was applied to analyze and incorporate the contributions of all the sampled airgap electromagnetic force harmonics that would have been ignored by the existing approach in the literature.

The corresponding simulated sound power levels varies as well for different modulation indices. As a result, the instantaneous sound power levels shown in Fig. 3.11 could not be characterized using the existing acoustic models. Therefore, two new sound metrics were introduced to put the acoustic noise due to the frequency modulation in proper perspective. It has been proven that the Multiple-Time Sampling approach used in this thesis works well for all non-sinusoidal excitations, especially when comparing the acoustic noise levels of electrical machines with varying modulation indices.

It is worth mentioning that non-sinusoidal excitation of the stator winding can result in an increase in the hysteresis and the eddy current losses of the electrical machine. The two quantities play a crucial role in defining the thermal behavior of the electrical machine. But more often than not, thermal models are excluded in the acoustic noise calculation routine. Therefore, to accurately obtain a realistic representation of the acoustic noise field around the electrical machine, a thermal model must be coupled to the existing subsystem models when setting up the multi-physics simulation problem. Hence, the role of temperature in the acoustic noise performance of the electrical machine will be studied in Chapter 4.

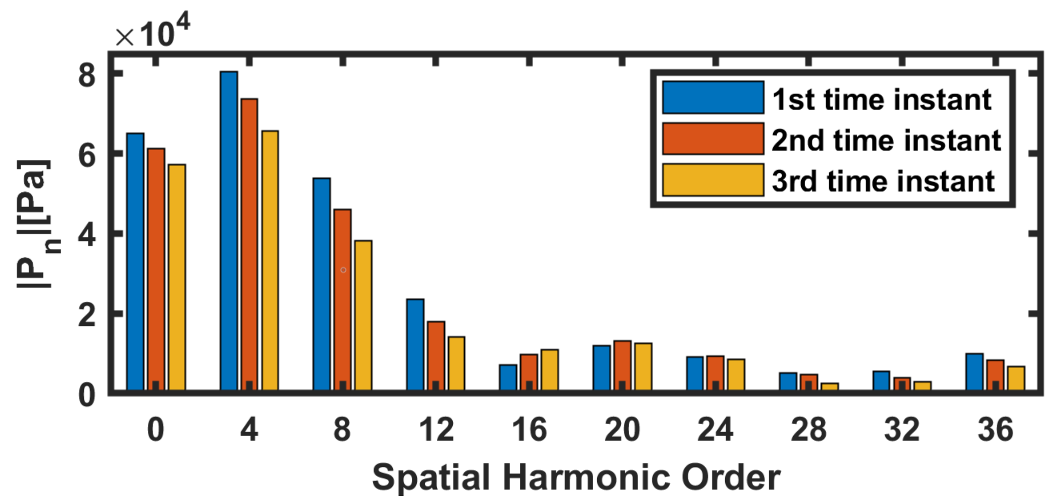

Fig. 3.8 4Pole 12Slot IPM motor: P_{n} harmonics for three (3) time instants.

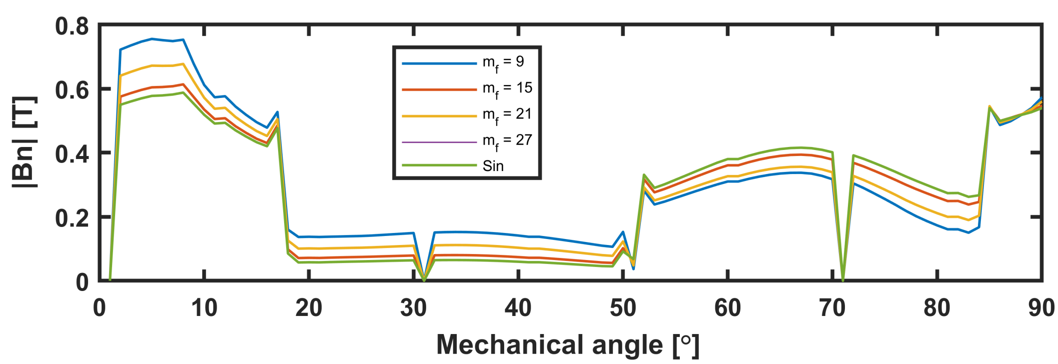

Fig. 3.9 Airgap magnetic flux density variation for different m_{f} at one time instant. The sinusoidal waveform is included for comparison purposes.

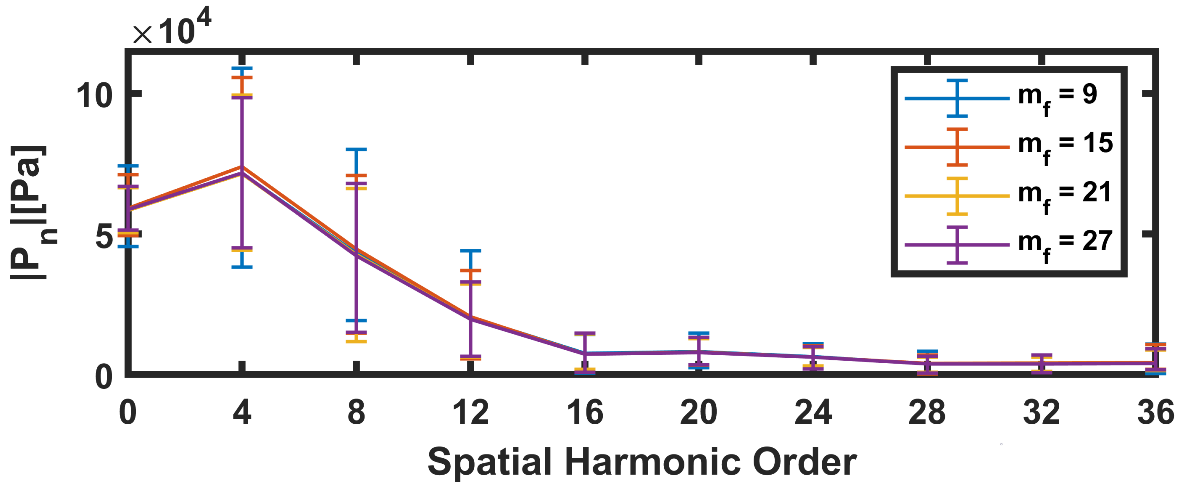

Fig. 3.10 Magnetic force harmonic variations for all samples at different modulation indices. All instants in one electrical period have been considered.

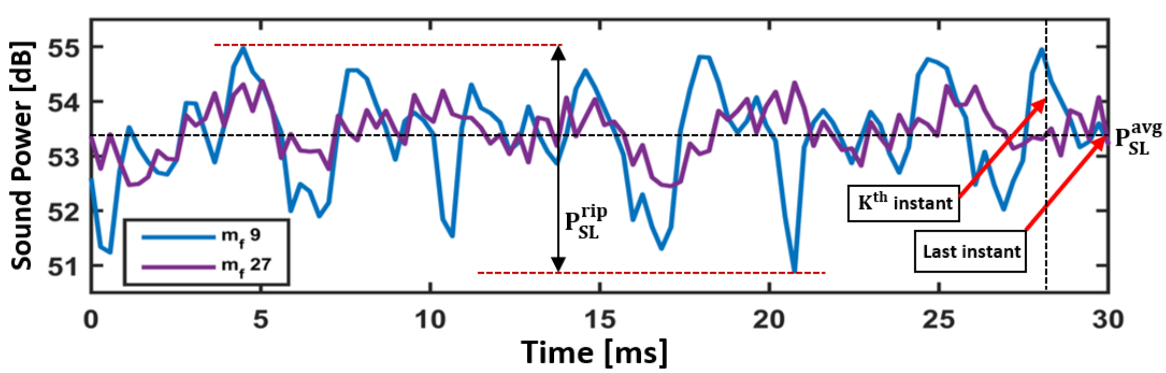

Fig. 3.11 Instantaneous sound power level over one electrical period.

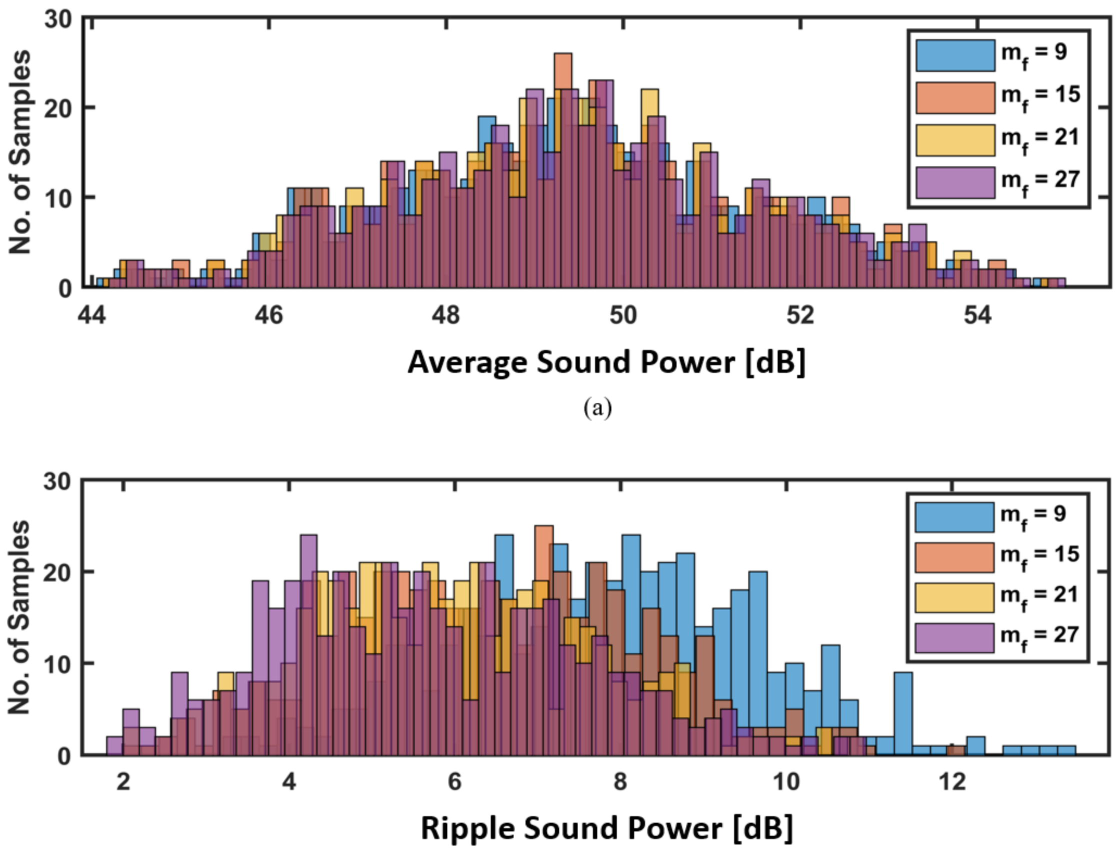

(a)

(b)

Fig. 3.12 Histograms of all samples for different m_f scenarios (a) average sound power level (b) Ripple sound power level.

Chapter 4

Effect of Temperature on Acoustic Noise of Electrical Machines

This chapter investigates the role of temperature in defining the acoustic noise field around the electrical machine, especially in the presence of non-sinusoidal excitation. The chapter is sectionalized as follows: Section 4.1 introduces the importance of incorporating thermal models in vibro-acoustic studies by drawing motivation from the paucity of thermo-acoustic materials in the literature; Section 4.2 explains how the thermal models were created and embedded in the existing finite element models to achieve the vibro-acoustic goal; Section 4.3 discusses the simulation procedure to evaluate the multi-physics performance objectives; Finally, Section 4.4 presents a collection of sound power data extracted from the simulated motor samples in the design space. It also discusses some emerging trends associated with the studied operating temperature points.

In summary, the proposed approach uses data-driven multi-physics simulation process discussed in previous chapters to provide thermo-acoustic design guidelines for evaluating the acoustic noise output of the 4Pole 12Slot Interior Permanent Magnet Synchronous Motor. This is then extended to study and extract knowledge related to the acoustic noise output of multiple motor samples within the design space of the Interior Permanent Magnet Synchronous motor.

4.1 Introduction

The issues with acoustic noise have received considerable research attention in recent times, and a survey of the literature in Chapter 1.5 covers most of the important aspects up to date. The majority of these works focus on improving the machine's electromagnetic, structural and acoustic subsystems. But in the real world, electric motors can run for several hours, if not days, resulting in unavoidable power losses. This can cause overheating of the electric motor if the cooling mechanisms are not effective.

Shunzo et al. [98], reported in the early 1980s that temperature variation could alter the resonant frequencies of the stator. But the revelation did not attract much attention. Since then, not much research effort has been invested in this endeavor. Therefore, the effect of temperature from the vibro-acoustic noise viewpoint is by no means mature, and further research work is needed to fully understand the heating phenomenon and its impact on acoustic noise. This chapter is inspired by Shunzo's work, and a recent publication authored by Tan-Kim et al. [82] in 2014. The latter used finite element tools to advance and validate Shunzo's hypothesis, but the authors did not extend their work to investigate other motor design topologies. What sets this thesis chapter apart, however, is the fact that instead of analyzing only one or two design geometries as done by predecessors, the design space of a 4Pole 12Slot Interior Permanent Magnet Synchronous Motor is covered with a large number of samples. Then, each sample is driven through temperature-dependent multi-physics finite-element simulations to extract knowledge related to their sound power levels.

Briefly, during startup, the machine's windings are fed with electrical voltage and current, V_s and I_s, which then produce an magnetomotive force, F, and eventual stator flux, ϕ_s. Based on the rotor topology, rotor flux, ϕ_r, or induced rotor flux is produced. Next, the interaction of both fluxes (ϕ_s and ϕ_r) generate an electromagnetic torque, Γ_{em}, which rotates the shaft at a given speed, Ω_r. This increase in rotor speed limits the input current due to the increasing back emf, E_g. At the same time, the winding resistance, R_s, the machine's magnetic flux density, B, and the power electronic converter's switching frequency, all introduce power losses. The power losses are dissipated as heat which is the main cause of temperature rise across the different components of the electrical machine.

Since the subsystem models, i.e., electromagnetic, structural, acoustic and thermal, are interdependent, any significant change in temperature will have a ripple effect on the other subsystem models. Hence, ignoring the thermal aspect can lead to inaccurate results. Thus, to ensure a more accurate determination of the acoustic capacity of the electrical machine, it is imperative to focus on the thermal subsystem as well. Fig. 4.1 [99] illustrates how the different physical subsystems of the machine work in concert to produce acoustic noise.

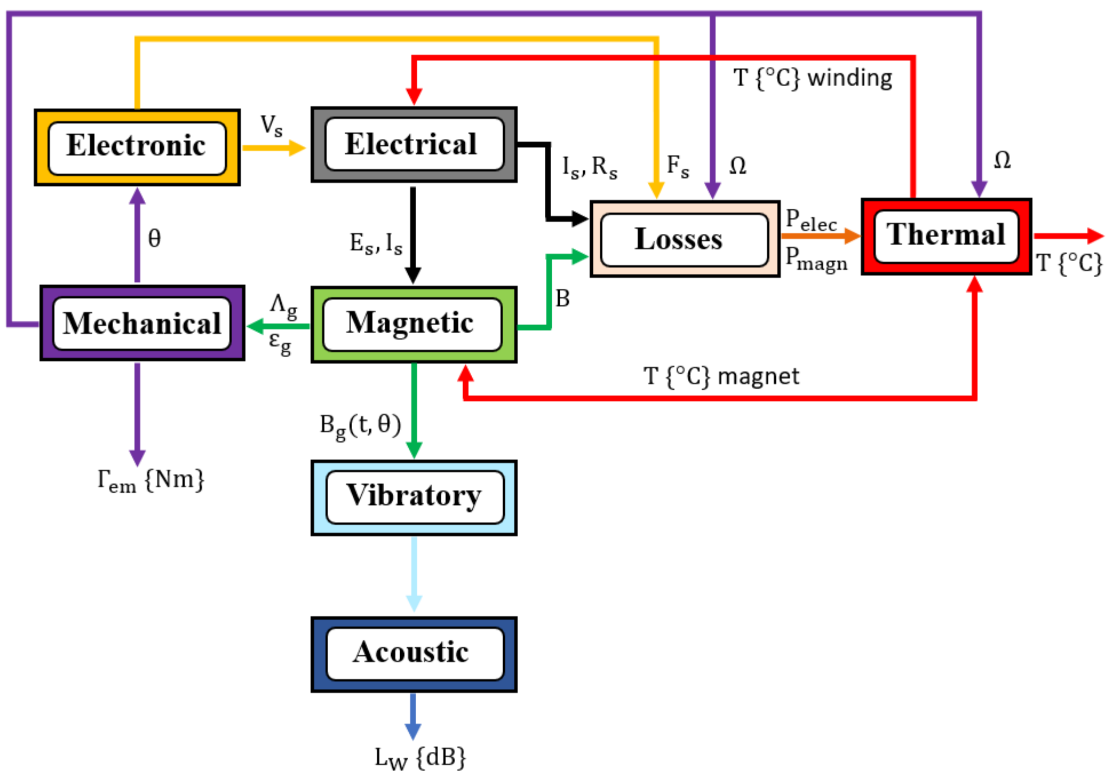

Fig. 4.1 Subsystems coupling of the electrical machine.

4.2 Thermal Modeling

For this work, it is assumed that a heating phenomenon already exists in the IPM motor and that no thermal FEA has been performed. Instead, temperature-dependent material properties have been embedded in the finite-element models. For the electromagnetic model, temperature-dependent B-H curves for non-oriented silicon steel and Neodymium-Iron-Boron (NdFeB) materials have been used. The B-H curves were obtained from actual measurements using the Brockhaus MPG 200 setup in Fig. 4.2. The temperature-dependent properties of non-oriented silicon steel and NdFeB permanent magnet are shown in Fig. 4.3 [100] up to 180°C.

For varnished copper, the material properties such as Young's modulus (see Fig. 4.4) were obtained from a previous thermal study conducted in [82]. Other material properties such as the Poisson's ratio for silicon-steel which exhibited consistent behavior for the studied temperature range were not considered. It must be re-iterated that this work has been done with strict adherence to NEMA's recommendation for selecting Class A insulation material properties. See Appendix C.2 for the different classes of insulation materials and their specific applications.

Also, it is assumed that enough time has passed for heat flow to stabilize. Hence, the temperature distribution is considered to be homogeneous across all the motor components at a steady-state condition. Additionally, the source of the heating phenomenon has not been considered in this chapter. However, Appendix C.1 provides detailed discussion on the causes of temperature rise in the electrical machine and related loss calculations. It is worth mentioning that all the assumptions (i.e., geometric, electromagnetic, structural and acoustic assumptions) considered in Chapter 3 are also applicable in this study.

Fig. 4.2 Brockhaus MPG 200 at the Computational Electromagnetics Lab.

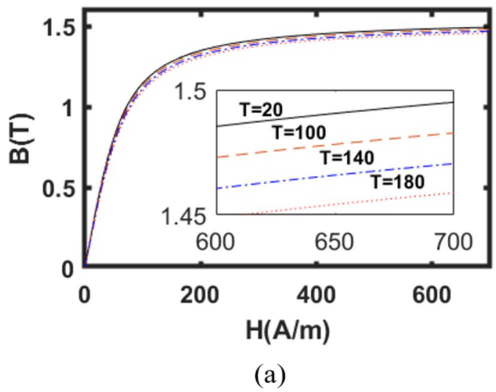

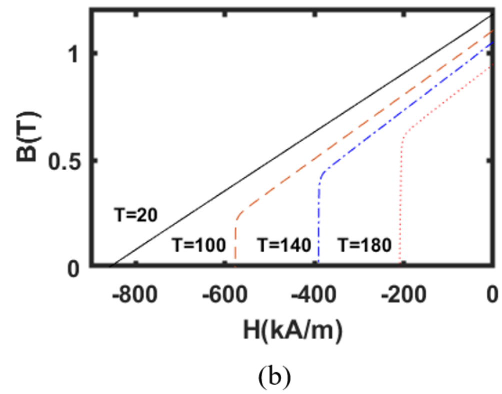

Fig. 4.3 B-H Curves (a) Silicon steel, (b) NdFeB permanent magnet.

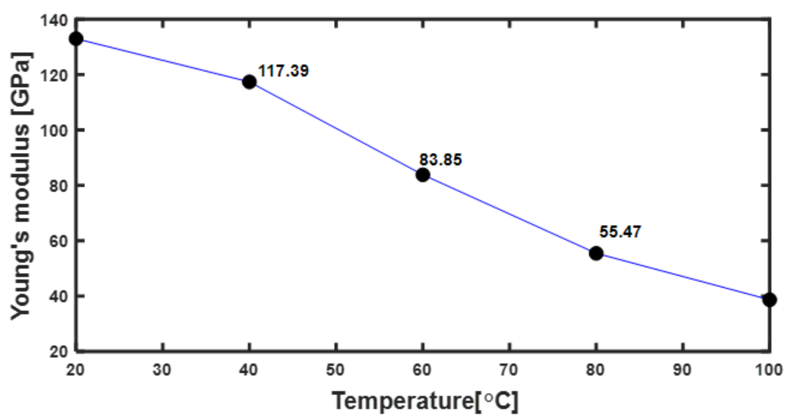

Fig. 4.4 Young's Modulus as function of temperature.

4.3 Multiphysical Simulations

The multiphysical performance objectives (MPO) to be evaluated are the magnetic flux densities in the airgap, the resonant frequencies, the stator vibrations and the sound power levels of each sample. Before calculating the MPOs, it is imperative to get a better understanding of how the thermo-acoustic simulation is performed for one sample which can then be extended to analyze the MPOs of all the 5000 samples in the design space of the IPM motor. The simulation process per sample is encapsulated in Fig. 4.5 below.

Briefly, the sample is taken through three main steps: The first step is the pre-processing step, where the sample is built by feeding its design variables obtained via DoE to the parameterized reference model in **module 1**. The next step is the simulation step, where

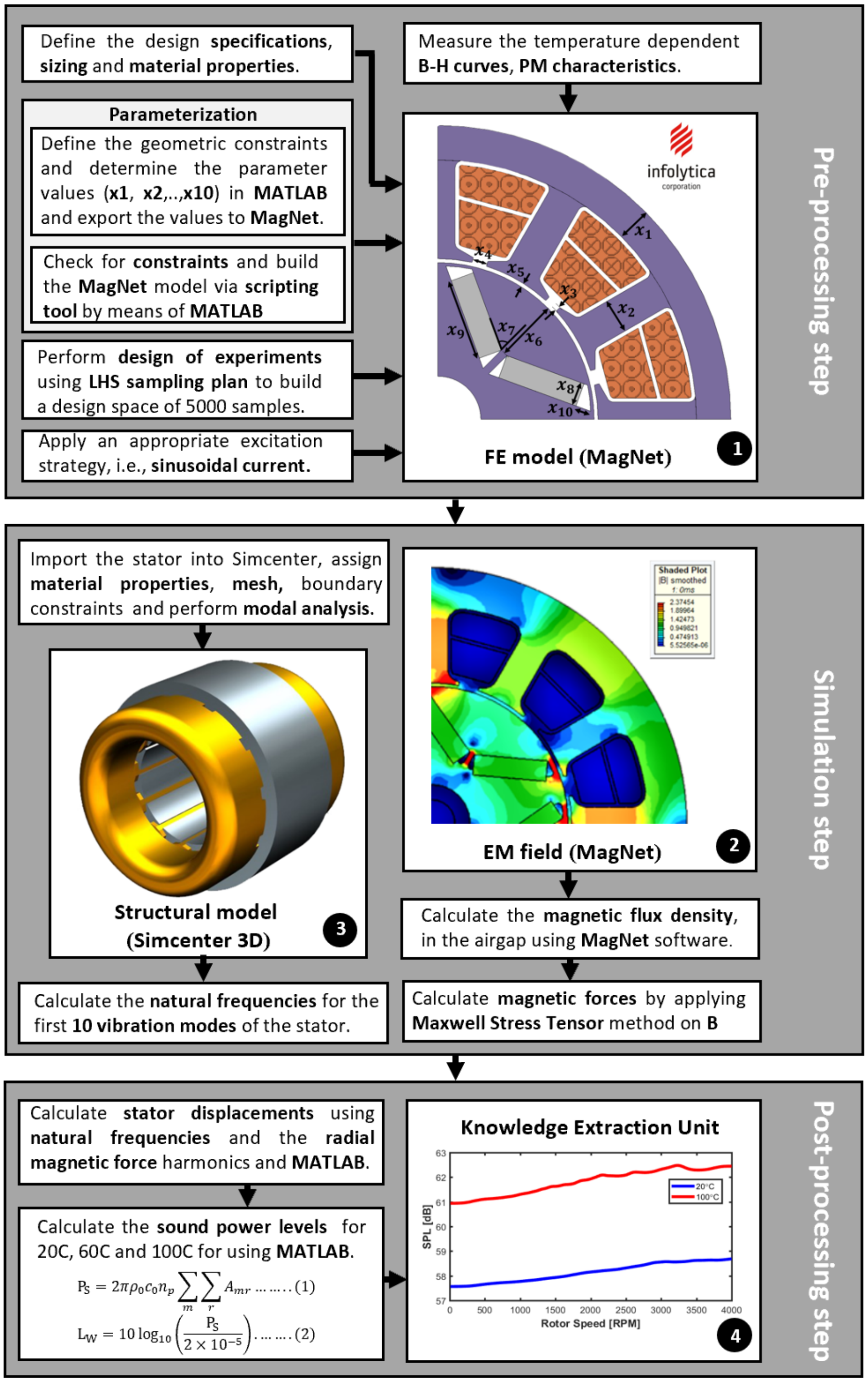

Fig. 4.5 Thermo-acoustic Noise Calculation Procedure Per Sample.

two main FE simulation analyses are performed. For the electromagnetic-field analysis, a balanced 3-phase sinusoidal current is applied to the model in **module 2**. Then, a transient 2D with motion solver is selected to simulate one mechanical period of the motor. Next, the airgap space is sampled at a specific time instant to extract the electromagnetic-field solutions, particularly the normal magnetic flux density, $\mathrm{B_n}$. Once the $\mathrm{B_n}$ is known, the magnitude of the normal magnetic pressure at any spatial angle along the tooth surface can be calculated from the Maxwell stress tensor method given in [91]. Next, a FFT analysis is performed to decompose the magnetic pressure waves into the frequency domain. For the structural modal analysis, the 3D Simcenter model in **module 3** is simulated to calculate the first 10 vibration modes of the stator. Finally, the post-processing step uses the resonant frequencies of the stator and the excitation forces to compute the stator vibrations and the sound power level. The knowledge extraction unit in **module 4**, analyzes the acoustic behavior of the IPM motor with respect to a range of operating speed points.

The simulation steps in Fig. 4.5 are automated to analyze the sound power levels of all 5000 samples at three operating temperatures: 20°C, 60°C, and 100°C respectively. However, for such a large number of samples, the FEA aspects can be time-consuming. To reduce the solve time, the motor's geometry can be exploited by applying symmetry conditions to simulate a fraction of the full model. One-quarter of the motor has been simulated using 100 fixed time steps. Then, the normal magnetic flux densities are extracted from the middle of the airgap at each time step and repeated in order to create a full waveform for FFT analysis. The simulation time took 4 minutes per $\frac{1}{4}$ EM model and about 8 minutes per full structural model (with 5 mm tetrahedral elements) on the Intel Xeon E5-1650 (6 cores, 3.5 Ghz, 32 GB RAM) processor.

It must be stated that both the Maximum Torque Per Ampere (MTPA) and the Flux-Weakening (FW) motor control strategies [9], discussed in Chapter 3 and Appendix B.1, have been respected in the electromagnetic-field simulation.

4.4 Results and Discussion

Fig. 4.6, shows the effect of temperature on the radial magnetic pressure for a random sample. It is demonstrated that thermal loading decreases the amplitude of the magnetic pressure for both the pressure waves and the harmonics. For Fig. 4.6 (b), only the most dominant modes of the pressure harmonics (which are recognized by the multiples of the number of poles, i.e., 4, 8, 12,...) are highlighted for visualization purposes. The decreasing trend in the amplitudes of the magnetic pressure with respect to increasing temperature can be ascribed to the gradual demagnetization of the permanent magnets. The magnetic properties of NdFeB magnets are highly dependent on temperature. Both the remanence and the intrinsic coercivity decrease with increasing temperature [101]. The decreasing remanence will cause the machine to draw more current to maintain the same torque, especially for Maximum Torque Per Ampere operations. This makes the permanent magnets more susceptible to demagnetization. The trend is similar for all the studied samples.

The most important vibration modes of the selected sample are presented in Fig. 4.7. All 5000 samples exhibited similar stator deformation trends since the boundary conditions were kept fixed in the space. Besides, modeshapes are not necessarily affected by structural variations. The scatter plots displayed in Fig. 4.8 cover the design space with the resonant frequencies of all samples for the three (3) operating temperatures. Each dot on the graph represents a motor sample and its corresponding resonant frequency for a given temperature. The location of the resonant frequencies of the base model for the different vibration modes are denoted by the symbol ★. At a glance, resonant frequencies tend to decrease substantially with respect to increasing temperature. The decreasing trend is unquestionably present across the board. In addition, the resonant frequency distribution in the space appears more associative and linearly correlated (see ρ values on each scatter plot) between mode 1-2 and mode 5-6, while mode 3-4 and mode 7-8 do not demonstrate any significant relationships. A perfect linearity relationship ($\rho = 1$) is observed between mode 1 and mode 2 at 100°C. The stronger the correlation strength, the closer the resonant frequency data points fall to a straight line, which means that regression models can fit tolerably well to the data such that an unknown quantity can be predicted from a known quantity. The stator vibrations, and eventually, sound power levels, are amplified when the resonant frequencies coincide or get closer to the exciting frequencies.

The sound power level distribution in the design space is illustrated in Fig. 4.9 for the Maximum Torque Per Ampere and Flux Weakening operation modes, respectively. The statistical symbols: μ represents the mean of the distribution, σ is the standard deviation, R denotes the range (left is for minimum and right is for maximum) and IQR represents the inter-quartile range of the sound power level distribution.

For the Maximum Torque Per Ampere, it is observed that sound power levels increase as temperature rises and the trend has been validated for different operating speeds (see

Appendix C.4). The P_{SL} at 20°C has a larger IQR than the P_{SL} at 60°C and 100°C, but only by 0.06 dB and 0.37 dB respectively. In both P_{SL} at 20°C and 60°C, about half of the design samples are within 45-52.7 dB range. However, P_{SL} at 100°C extends three-quarters of the samples farther outside the range than at lower temperature levels, which demonstrates increasing trend at elevated temperatures. About 1.4% of the design samples operated in the flux-weakening region. Given the relative lack of acoustic data and the large number of samples that are needed to observe noticeable trends, observations in the flux-weakening region have not been included in the current analysis.

4.5 Conclusions on the Effect of Temperature on Acoustic Noise

From this study, it could be said that heating does not only shorten the lifespan of the electrical machine but it can also be inimical to its acoustic performance. The operating temperature of the electric motor was found to have a strong correlation with the emitted noise. This was ascribed to the increasing rate of resonance which aggravated the vibrations due to the decreasing rate of the natural frequencies at very high temperatures. The trend was also found to be consistent with all the studied motor samples.

Another interesting observation is the diminishing trend in the magnitude of the electromagnetic force waves at elevated temperatures. This is an indication that the amplitude of the electromagnetic forces are not as important as the occurrences of resonance in the electric motor. What this could means is that any attempt at mitigating acoustic noise in the electric motor must aim at creating a mismatch between the frequencies of the excitation force and the natural frequencies of the electric motor structure rather than targeting the magnitude of the excitation forces themselves. One way of doing this, although not relevant for this thesis, is to modify the motor geometry to change the natural frequencies of the stator structure. Once a mismatch is achieved, the occurrence of resonance will reduce and ultimately the acoustic noise levels as well.

While it has been shown in Chapters 3 and 4 that the impact of non-sinusoidal excitations and thermal issues is significant in terms of the acoustic performance of an electrical machine, this evaluation requires a full multi-physics analysis. This can be extremely expensive if being performed during the design and optimization cycle where hundreds, or even thousands, of potential design candidates may be evaluated. To accelerate this process, simpler models incorporating the multi-physics effects, are needed. The next chapter explores the development of surrogate models as an approach to achieving this.

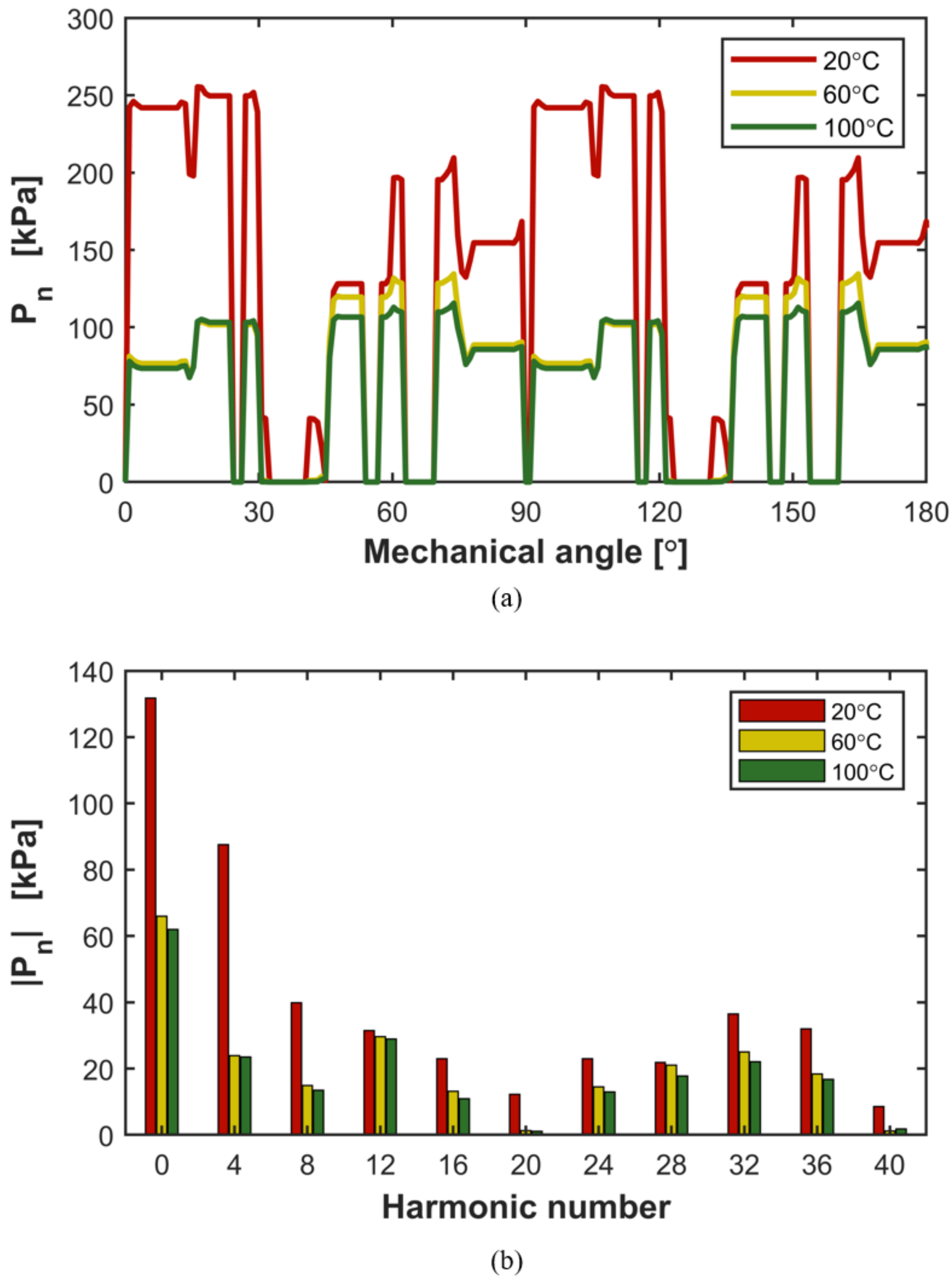

Fig. 4.6 Electromagnetic-field Analysis for Selected Sample (a) Radial Magnetic Pressure vs Mechanical Angle (b) Radial Magnetic Pressure Harmonics.

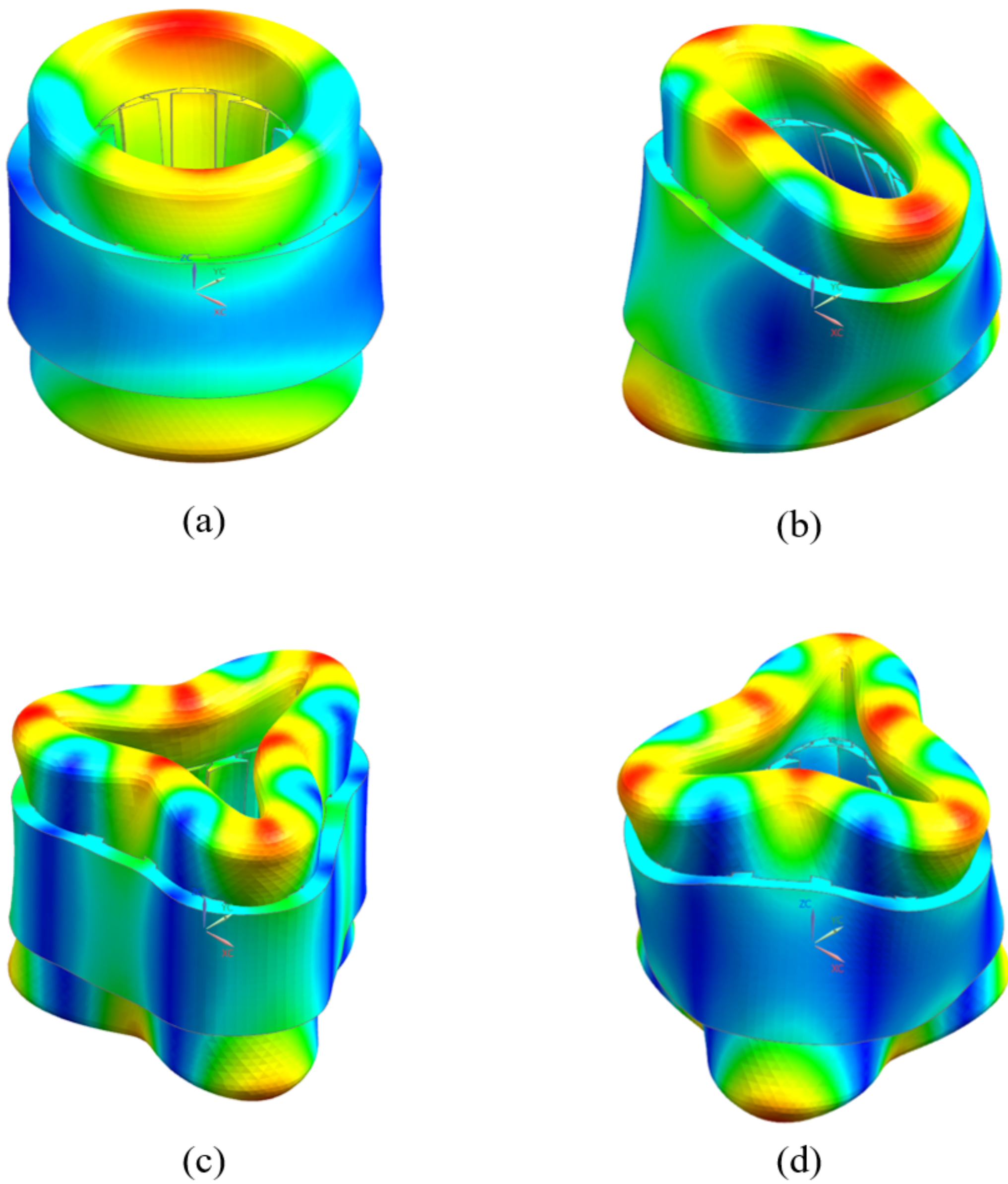

Fig. 4.7 Vibration modes for a selected sample (a) Mode 1 (7.301 kHz) (b) Mode 2 (8.423 kHz) (c) Mode 3 (16.890 kHz) (d) Mode 4 (17.910 kHz).

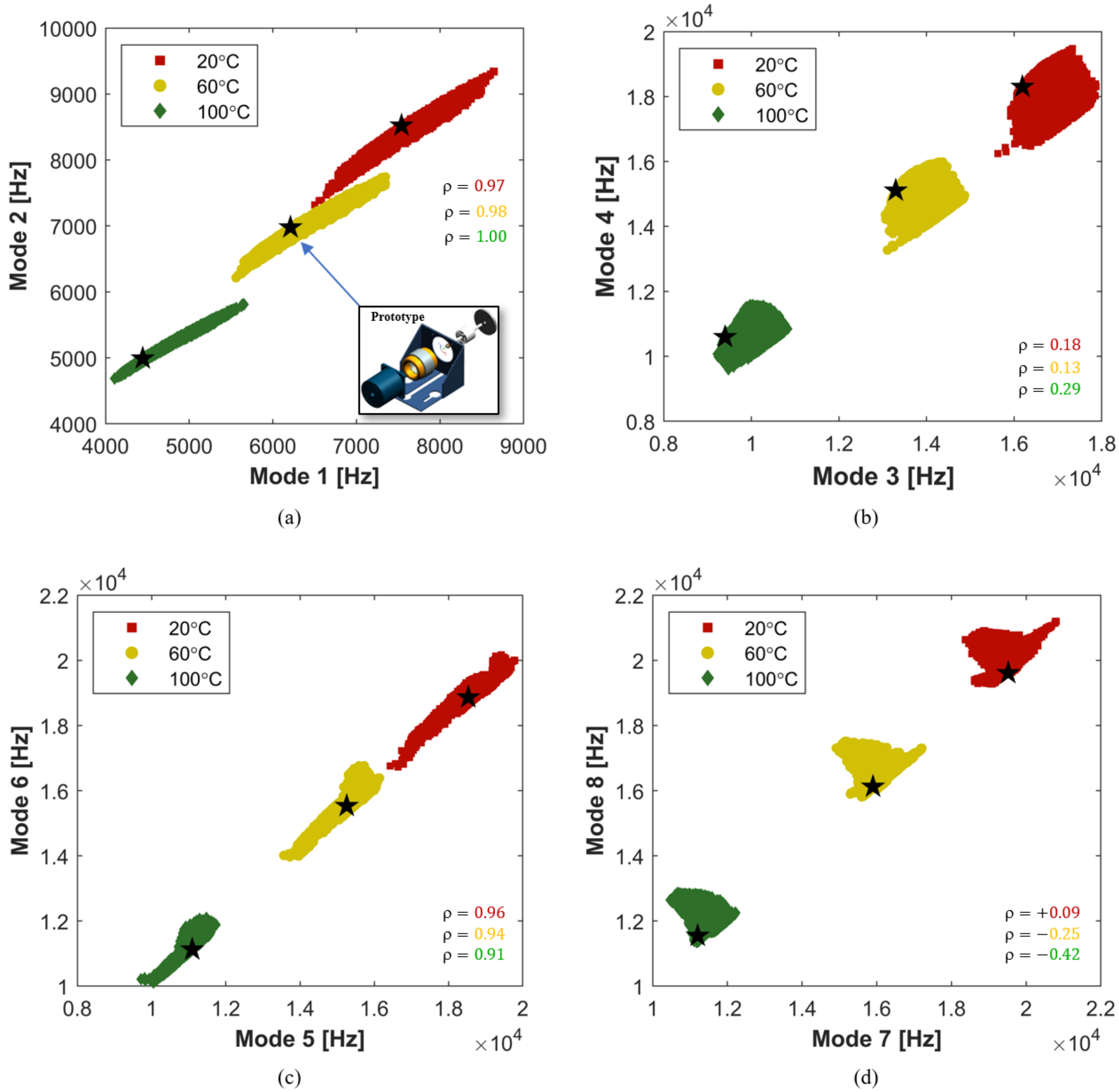

Fig. 4.8 Resonant Frequency Population Plots for All Samples (a)Mode 1 vs Mode 2 (b)Mode 3 vs Mode 4 (c)Mode 5 vs Mode 6 (d)Mode 7 vs Mode 8.

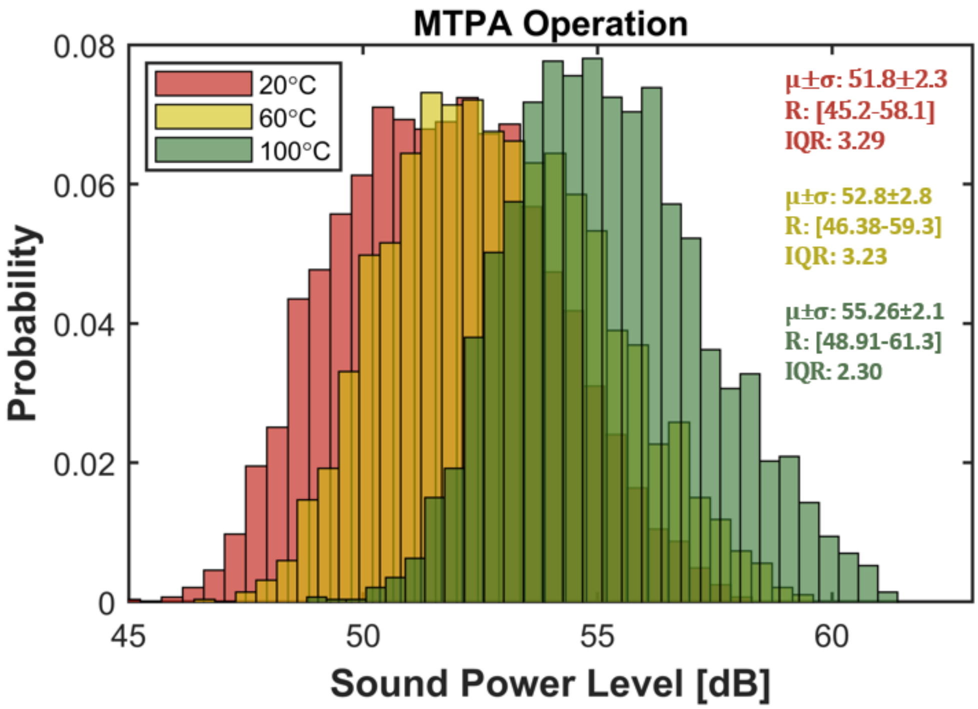

(a)

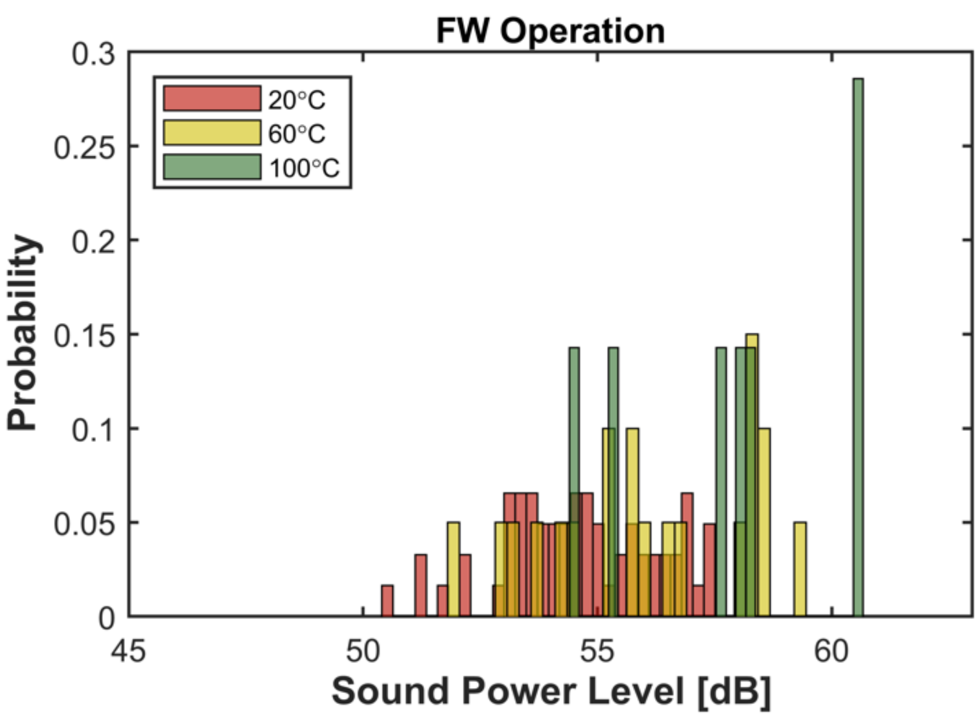

(b)

Fig. 4.9 Sound power level at different operating modes of the IPM motor (a) Maximum torque per ampere operation (b)Flux-weakening operation.

Chapter 5

Surrogate Models in Acoustic Noise Prediction of Electric Motors

Design and optimization problems (DOP) typically require running thousands of motor simulations which can be time-consuming. In some cases, simulations could take several hours, if not days. Therefore, it is important to find an alternative means of reducing the solution time. Surrogate models (SM) have commanded a lot of research attention in recent times. The adeptness of SMs to emulate the output of complex computer simulations with little computational effort makes them the best candidate for most DOP applications. Therefore, chapter 5 proposes the use of surrogate models to predict the acoustic noise, applied to the 4Pole 12Slot Interior Permanent Magnet Synchronous Motor. The procedure will entail first using FEA to evaluate the acoustic performance across the design space of the IPM motor. Then, 4 classes of SM are used to represent a portion of the design space before attempting to generalize and make predictions in a much larger space with a relatively lower computational burden. It is demonstrated that SMs can be considered as appropriate replacements for the time-consuming FEA simulations for future DOPs.

The chapter is organized as follows: Section 5.1 discusses the motivation for this research; Section 5.2 provides guidelines to create the P_{SL} data library for different design geometries; Sections 5.3 and 5.4 review SMs; the novelty resides in Section 5.5, where the multi-physics problem is cast as a regression problem. Here, an ensemble of 17 surrogates are implemented to predict P_{SL} for different designs; finally, Section 5.6 evaluates the surrogate models' competence and recommends suitable candidates for the regression.

5.1 Introduction

Despite advances in modern computing infrastructure, the computational cost associated with multi-physical problems such as acoustic noise evaluation of electrical machines still remains prohibitively expensive. Depending on the coupling scheme used, i.e., whether one-way or two-way coupling, concatenating the electromagnetic, structural and acoustic subsystems to calculate the emitted noise can be CPU-intensive.

As previously discussed in earlier chapters, acoustic noise has been covered extensively in the literature. Most of the works focused on improving the fidelity of the finite element models. However, in the digital design process where most design and optimization routines require the simulation of thousands of motor structures in order to arrive at an optimal motor design, the process can be a computational burden. Therefore, it is imperative to seek out an alternate means of handling DOPs where the solution time could be shortened. For example, the authors in [102] used a High-Performance Computing service to reduce the simulation time for a feature extraction DOP analysis of an integrated motor drive system.

In engineering design, surrogate models are widely used to address some of these concerns [10]. In the context of electric motor drives, SMs are often used as function evaluators to (a) reduce the need for time-consuming FE simulations [10], and (b) speed up the optimization process in the subsystem and system levels [72]. For the current state of the art in machine design, SM application is limited. Silva [10] used surrogate models to explore aspects of electromagnetic design but did not include acoustic noise in his work. Mohammadi et al. [97] used surrogate models on different synchronous reluctance motors to predict $\mathrm{P_{SL}}$ for design and optimization purposes, but their surrogates did not focus on the underlying subsystem models. However, Wang [103] fitted models to structural subsystems of several stator geometries to predict their natural frequencies, but he was only interested in knowing how his models handle the parametric variations in the stator. Hence, the objective of this chapter is to extend previous works by exploring the competence of different SMs as rapid function emulators for future system-level DOPs (e.g., an electric vehicle in which the same machine topology is used). Here, a wide range of surrogates will be implemented and screened for performance, suitability and selectability for the acoustic noise problem.

5.2 Multiphysics Simulations and Data Collection

To set up the surrogate problem, a datastore for different designs must be created. The 4Pole 12Slot IPMSM was used as the reference model. The flowchart in Fig. 5.1 delineates how the data was generated. **Module 1** encapsulates the CAD modeling, geometric parameterization and space filling. Once the design space is created with the required number of samples, a portion of the samples are explored and simulated (**Module 2**). For every sample, the $\mathrm{B_n}$ per mechanical cycle for a fixed sinusoidal current was extracted using the FEA package in [6]. It took about 4.5 minutes per sample on the PC (Intel Xeon E5-160, 6 core, 3.5 GHz, 32 GB RAM). Once the $\mathrm{B_n}$ values were found, the airgap space was sampled at a specific time instant to compute $\mathrm{P_n}$ using the Maxwell Stress tensor in (3.4).

For **Module 3**, a 3D structural modal analysis was performed to evaluate the natural frequencies, $\mathrm{f_s}$, of the stator. For a stator mesh with about 16000 tetrahedral elements, it took 12 minutes per sample to extract the first 10 modes. To further reduce the solution time in **Module 4**, the semi-analytical approach used in Chapters 4 and 3 has been applied to calculate the acoustic noise ($\mathrm{P_{SL}^A}$) at different operating speed points for each sample.

Once the results from **Module 1** to **Module 4** are obtained, a database can be constructed based on the evaluated samples. Each sample is represented by 1-10 design variables, 1-100 $\mathrm{P_n}$ harmonics, 1-10 stator $\mathrm{f_s}$ and a corresponding $\mathrm{P_{SL}^A}$ for varying rotor speeds.

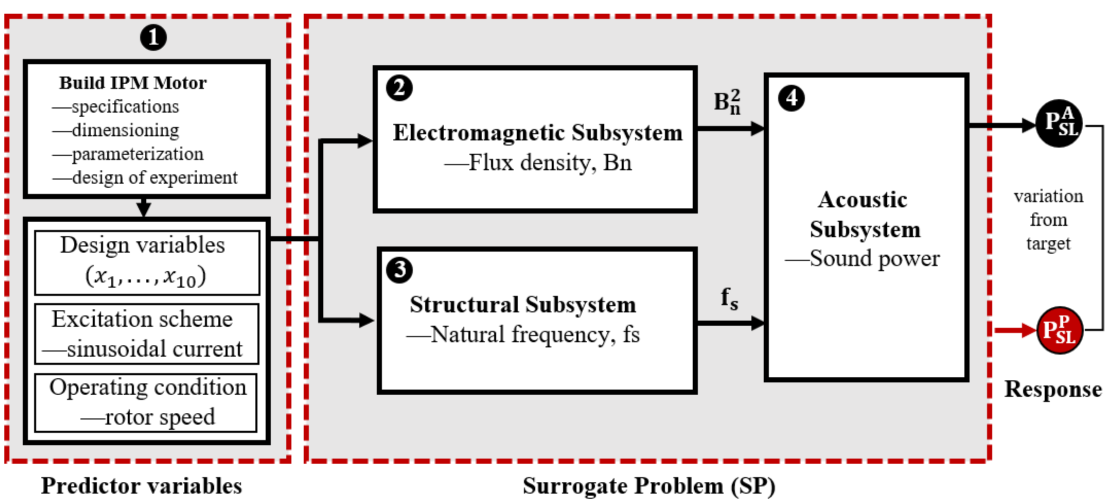

Fig. 5.1 Acoustic noise generation mechanism. $\mathrm{P_{SL}^A}$ and $\mathrm{P_{SL}^P}$ are the actual sound power and predicted sound power levels for FE and SM respectively.

5.3 Overview of Surrogate Models

A surrogate model is a mathematical model that mimics the behavior of a computationally expensive simulation code over the complete parameter space as accurately as possible, using the least amount of data points. In general, SMs trade precision for rapidity. However, some models can explain certain phenomena so elegantly and provide predictions with such a high degree of accuracy that they are sometimes raised to the level of theories and laws [104]. Fig. 5.3 presents a taxonomy for SMs. As can be seen, SMs can be divided into two main groups: (i) First Principles SMs and (ii) Meta-Models. Each SM can still be subdivided into different categories with their own characteristics.

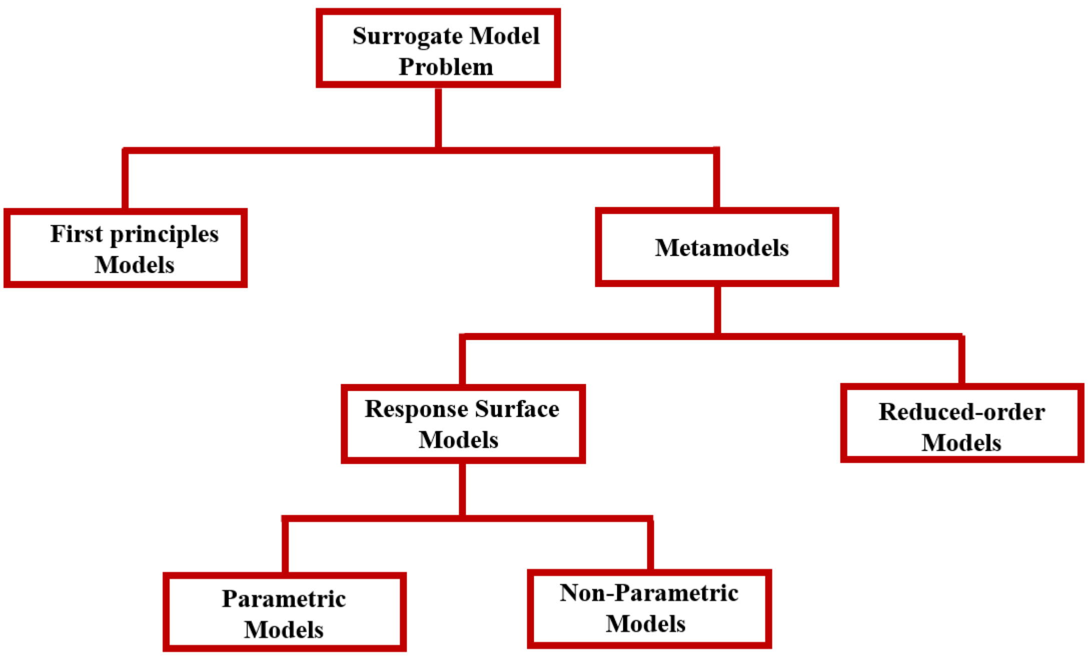

Fig. 5.2 A Taxonomy for Surrogate Models.

A first principles model is built directly from established scientific laws without relying on fitted parameters. What this means is that first principles SMs are simplified versions of the original mathematical model. An example is the Magnetic Equivalent Circuit (MEC) which is based on lumped-parameter magnetic circuit models (reluctance networks). In MECs the field distribution is mapped into a relatively small number of reluctance elements that represent the flux tubes in the geometry of the modeled device [105]. Using this concept, the magnetic fields of complex devices can be quickly solved using methods and techniques developed for electric circuits.

Meta-models are not derived directly from the theory. As illustrated in Fig. 5.3, meta-models are phenomenological models that find the mapping between design variables and model outputs through data obtained from the high-fidelity simulation model. This is what gives them the name meta-model meaning *model of the model.* The symbols used in Fig. 5.3 are explained as follows: R_r is the real system observation or response, R_f is the response obtained from FE simulations, R_m is the response produced by the surrogate model and ε is the error between prediction/observation pair.

Response Surface Models (RSM) are a kind of Meta-model that explore the relationships between several input variables and one or more output variables. RSMs, in turn, can be divided into two classes: (i) Parametric Models which assume a priori a certain functional relationship between inputs and outputs; and (ii) Non-Parametric Models that do not assume any specific functional relationship.

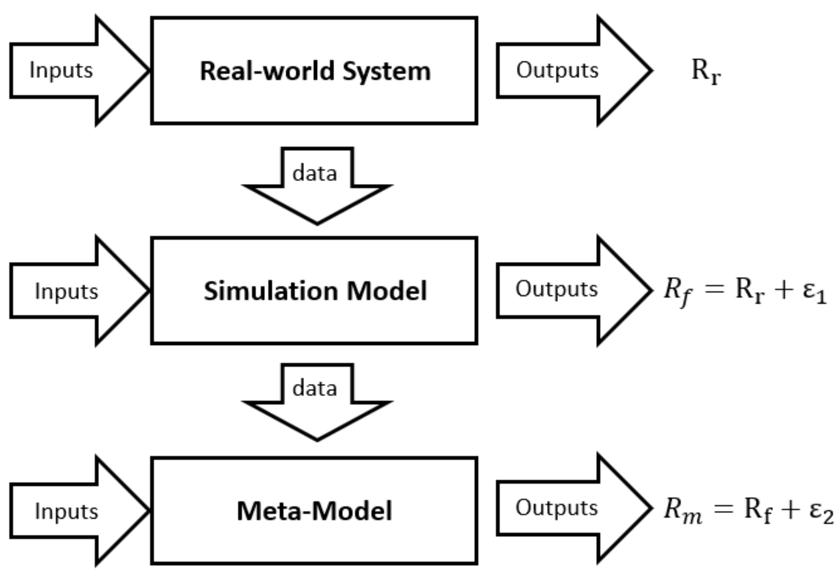

Fig. 5.3 Meta-Model Concept.

The simplest types of parametric meta-models are the polynomial models [106]. They usually consist of low-order polynomials fitted to sample data by least squares estimation. Polynomial models were very popular methods for the approximation of expensive computer simulations until the 1990's [107], [108]. As they became more widely used and better understood, their limitations became more and more apparent, i.e., the curse of dimensionality [106], the inability to create accurate global approximations in highly nonlinear design spaces [109] and lack of interpolation properties. As a result, by the end of the 1990's, the interest shifted to more flexible, non-parametric, approximation models, such as Radial Basis Functions (RBF) [110], and Kriging [111].

RBFs use a weighted sum of simple functions in an attempt to approximate complicated function landscapes, while Kriging uses a global polynomial approximation combined with a localized deviation represented by a Gaussian process regression. Both models tend to be very flexible with respect to the nature of the landscapes they can emulate [109]. Furthermore, confidence intervals for the predictions can be obtained without much additional computational cost [112]. Despite these advantages, Kriging and RBFs have more complex fitting procedures which usually involve the solution of another optimization problem. Besides, Kriging predictions require matrix inversions which, depending on the number of samples, may also be computationally expensive.

In addition to these two, other data-fitting models have also been explored in the literature, e.g, Artificial Neural Networks [113], Genetic Programming [114], Linear Regression (L), Multivariate Adaptive Regression Splines (an extension of Linear models that model nonlinearities) [115], Support Vector Machines (SVMs) [109], and Decision Trees (T) [116].

Another type of meta-model is the so called Reduced Order Model (ROM). Instead of working on integral values of the field solution (e.g., torque, efficiency, etc) a ROM tries to reduce the number of of nodes in the FEM system. A ROM mimics the basic structure of the FEA and not just a functional relationship between input and output parameters. Since ROMs operate in the dimensionality of the discretization rather than on the design space, they tend to be less sensitive to the increase in the number of design variables. On the other hand, their application to shape design can be troublesome. For this reason, ROMs are rarely used in the context of geometry design.

There is no consensus as to which is the best surrogate modeling technique in the context of CAD. Each family of surrogate models has its own advantages and disadvantages. First principle surrogate models can offer concise descriptions of the device inner physics but are hard to generalize across different problems. Response surfaces can be easily applied to any kind of problem but offer little insight into the underlying process inner workings. ROMs retain the basic structure of the underlying finite element code but since they need direct access to the mesh structure and field values, they are difficult to couple with proprietary simulation packages.

5.3.1 Construction of Surrogate Models

In surrogate-based problems, a set of observations of input data called "Predictors" and known output response variables are required to generate the mapping functions that represent the models. From this point onwards, it is worth mentioning that the term "sample" has been used to represent each predictors-response pair in this document. The general steps involved in building a surrogate model are summarized below, and further encapsulated in Fig. 5.4.

1. **Generate sample database**: normally, samples are generated via computer simulations in which the variables cover a carefully chosen range of values. The database can also be a collection of information from an empirical study over a period of time.

2. **Select surrogate model**: identify a suitable parametric or nonparametric meta-modeling approach to use. The model is selected based on the problem and the nature of the predictors and the response variables.

3. **Partition sample database**: clean the data by removing outliers and treating missing data. Then, pre-process the data into a form suitable for the chosen modeling algorithm by specifying subsets of the data to be used for training, validation, and testing.

4. **Build surrogate model**: the selected meta-model in step two is fitted to the training data set to generate the surface response functions for mapping the predictors onto the response variables.

5. **Assess model performance**: this step fine-tunes the model's hyperparameters using the samples from the validation data set.

6. **Test new data**: the model is tested on new data not known to the model. In general, the accuracy of SMs depends on the number of samples that are used to train the models. Therefore, this step can be repeated by varying the training sample size until target requirements converge.

7. **Final tuned model**: if target requirements are met, the developed model can then be used as a possible replacement of the high-fidelity model. What this means is that if additional values of predictor variables are collected from the high-fidelity model without an accompanying response value, the fitted model can be used to make a prediction of the response at a much lower computational cost.

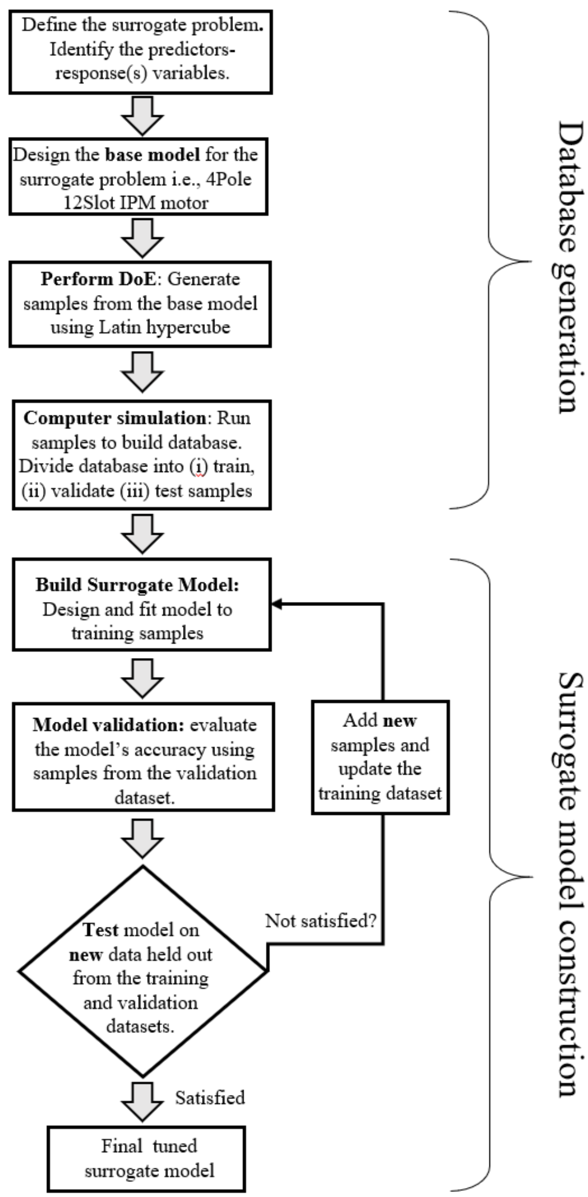

Fig. 5.4 Diagram of elements involved in building SMs.

5.3.2 Validation Strategies in Modeling

The evaluation of a model's skill on the training dataset would result in a biased score. Therefore, the model must be evaluated on a held-out dataset that has not been seen by the model in order to give an unbiased estimate of the model's prediction accuracy. Since the validation dataset and the test dataset are both held-out samples, there is much confusion in surrogate modeling about what a validation dataset is exactly and how it differs from a test dataset. As a result, both terminologies are sometimes used interchangeably.

A validation dataset is a sample of data used to provide an unbiased evaluation of a model fit on the training dataset while tuning model hyperparameters. For example, to choose the number of hidden layers in a Neural Network model. The test dataset, on the other hand, is the held out samples that have not been used prior, either for training the model or tuning the model parameters. Because the test samples were not used in building or fine-tuning the model, they are predominantly used to evaluate the performance of the final tuned model, especially when comparing or selecting between final models.

A model that is too flexible and suffers from over-fitting has a worse validation accuracy. Therefore, to avoid over-fitting to the training dataset, an appropriate validation scheme must be chosen to examine the predictive accuracy of the fitted model. In fact, the same validation scheme must be used if the ultimate goal is to compare the effectiveness of several models. Three (3) main types of validation strategies will be discussed in this section.

Cross-Validation

This method protects against over-fitting by partitioning the dataset into folds (k disjoint divisions) and estimating accuracy on each fold. For each fold, the model is trained using observations from other folds. Then, model performance is assessed using in-fold data. The average test error is calculated over all folds. Cross validation gives a good estimate of the predictive accuracy of the final model trained using the full data set. The method requires multiple fits, but makes efficient use of all the data, so it works well for small data sets.

Holdout Validation

Here, a percentage of the data is used as a validation set. The model is fitted on the training dataset and the performance is assessed using the validation set. The model used for validation is based on only a portion of the data, so holdout validation is appropriate only for large data sets. The final model is trained using the full data set.

No Validation

All the data is used for training and the error rate is computed on the same data. This means that, here, there is no protection against over-fitting. This approach, however, is not recommended because without any test data, you get an unrealistic estimate of the model's performance on new data. That is, the training sample accuracy is likely to be unrealistically high, and the predictive accuracy is likely to be lower.

5.3.3 Quality Assessment of Models

Traditionally, different measures of model accuracy are used for quality assessment of surrogate models. These measures, referred to as Performance Metrics in this document, mostly use the error deviation from the benchmark response to evaluate the competence of the surrogate model. As an illustration, let $\mathbf{y} = [y_1, y_2, ..., y_{\mathrm{n}}]$ and $\mathbf{y}_{\mathrm{s}} = [y_{\mathrm{s}_1}, y_{\mathrm{s}_2}, ..., y_{\mathrm{s}_{\mathrm{n}}}]$ be the arrays of responses computed with a high-fidelity (or benchmark) model and its surrogate model, respectively. The most popular measures of error are defined as follows:

- The Mean Squared Error (MSE)

$$\epsilon_{\mathrm{MSE}}(\mathbf{y}, \mathbf{y}_{\mathrm{s}}) = \frac{\sum_{\mathrm{i}=1}^{\mathrm{n}} (y_{\mathrm{i}} - y_{\mathrm{s}_{\mathrm{i}}})^2}{\mathrm{n}} \tag{5.1}$$

- The Root Mean Squared Error (RMSE)

$$\epsilon_{\mathrm{RMSE}}(\mathbf{y}, \mathbf{y}_{\mathrm{s}}) = \sqrt{\frac{\sum_{\mathrm{i}=1}^{\mathrm{n}} (y_{\mathrm{i}} - y_{\mathrm{s}_{\mathrm{i}}})^2}{\mathrm{n}}} \tag{5.2}$$

- The Mean Absolute Error (MAE)

$$\epsilon_{\mathrm{MAE}}(\mathbf{y}, \mathbf{y}_{\mathrm{s}}) = \frac{\sum_{\mathrm{i}=1}^{\mathrm{n}} |y_{\mathrm{i}} - y_{\mathrm{s}_{\mathrm{i}}}|}{\mathrm{n}} \tag{5.3}$$

- The Mean Absolute Percentual Error (MAPE)

$$\epsilon_{\mathrm{MAPE}}(\mathbf{y}, \mathbf{y}_{\mathrm{s}}) = \frac{1}{\mathrm{n}} \sum_{\mathrm{i}=1}^{\mathrm{n}} \left| \frac{y_{\mathrm{i}} - y_{\mathrm{s_i}}}{y_{\mathrm{i}}} \right| \times 100 \tag{5.4}$$

- The Maximum Absolute Error (MAX)

$$\epsilon_{\mathrm{MAX}}(\mathbf{y}, \mathbf{y}_{\mathrm{s}}) = \max_{\mathrm{i} \in 1,\ldots,\mathrm{n}} |y_{\mathrm{i}} - y_{\mathrm{s_i}}| \tag{5.5}$$

- The Coefficient of Determination (R^2)

$$\mathrm{R}^2 = 1 - \frac{\sum_{\mathrm{i}=1}^{\mathrm{n}} (y_{\mathrm{i}} - y_{\mathrm{s_i}})^2}{\sum_{\mathrm{i}=1}^{\mathrm{n}} (y_{\mathrm{i}} - \overline{y})^2} \tag{5.6}$$

The MSE and the RMSE work on the assumption that the error is unbiased and normally distributed. In this scenario, these two performance metrics have very direct interpretations. The MSE gives the variance of the error and the RMSE estimates the standard deviation of the error distribution [117]. The RMSE is generally favoured over the MSE because its values have the units of the response which makes it easier to interpret.

The MAE also returns values in the units of the response. It differs from the RMSE on the assumption about the error distribution. While RMSE assumes a normal distribution, the MAE assumes a uniform distribution [117]. Another difference between these two metrics is that while the MAE gives the same weight to all errors, the RMSE gives more weight to errors with larger absolute values than errors with smaller absolute values [118].

The MAPE is a scale independent measure that is useful to compare models across different data sets. When a given surrogate model is used to approximate different physical quantities with large variations in range, the MAPE offers a more intuitive interpretation of accuracy than the aforementioned metrics.

The lower the values obtained by each of these metrics, the more accurate the surrogate model is. While MSE, RMSE, MAE and MAPE are used to measure the the overall accuracy of the model, MAX estimates upper bounds for the prediction errors. It is important to highlight that the MAX is the least robust statistic, i.e., it is maximally sensitive to outliers. Thus, a surrogate model that produces very accurate predictions for the whole dataset except for one sample would still receive a low score.

The coefficient of determination, R^2, is another measure of model accuracy, where $\overline{y}$ is the mean of the set y. The R^2 is interpreted as the "proportion of variance explained by the surrogate model" [119]. The term $\sum_{i=1}^{n} (y_i - y_{si})^2$, as in the MSE, is the error variance. The term $\sum_{i=1}^{n} (y_i - \overline{y})^2$ is the sample variance with $\overline{y}$ being the mean of the distribution of the response variable y. Thus, a R^2 of 1 means that the sum of the errors is 0, which means that the model explains 100% of the variance contained in the data. Different from the other metrics, the higher the values of R^2, the more accurate the surrogate model is. The values of R^2 ranges from (-∞,1] and it is maximum only when the error, $y_i - \hat{y}_{si}$, is equal to 0.

5.4 Summary of Selected Surrogate Models

Four (4) classes of regression models have been considered: Linear Regression (L), Decision Tree (T), Support Vector Machine (SVM) and Gaussian Process Regression (GP). To guarantee fairness in performance, it is worth emphasizing that no preferential treatment was given in terms of tuning or modifying individual models. For this reason, neural networks, whose skill solely depends on the definition of number of neurons, hidden layers and the regularization, have not been implemented in this work.

5.4.1 Linear Regression Models

Linear regression was the first type of regression analysis to be studied rigorously, and to be used extensively in practical applications. This is because models which depend linearly on their unknown parameters are easier to fit than models which are non-linearly related to their parameters and because the statistical properties of the resulting estimators are easier to determine. If the relationship between the predictor variables and the response variable is linear, L models can be very effective.

The simplest version of linear regression models, L_1, has been defined in (5.7a), where y is the response variable, $x_1, \ldots, x_n$ are the predictor variables, β_1, β_2,..., β_n are the unknown regression coefficients, β_0 is the intercept, and ε_j is the j^{th} random error term that accounts for the discrepancy between the model and the observations. The predicted values of the regression model are derived from (5.7b), where $\widehat{y}$ is the predicted value, and $\widehat{\beta_0}$, $\widehat{\beta_1}$,...,$\widehat{\beta_n}$ are the estimates of the regression coefficients.

The following variation of L models were used in this thesis: (i) Interaction Linear Regression (L_2), where interaction terms ($\beta_{i,j}x_ix_j$) are added to (5.7a); (ii) Robust Linear Regression (L_3), where the maximum-likelihood is used instead of the least squares method to find the coefficients β_j; and (iii) Stepwise Linear Regression (L_4), where the terms $\beta_j x_j$ in (5.7a) are added one by one to find the simplest possible model.

$$y = \beta_0 + \sum_{j=1}^{n} \beta_j x_j + \varepsilon_j \tag{5.7a}$$

$$\widehat{y} = \widehat{\beta_0} + \sum_{j=1}^{n} \widehat{\beta}_j x_j \tag{5.7b}$$

5.4.2 Decision Tree Models

A decision Tree (T) is a regression model expressed as a recursive partition of the instance space. The Decision Tree consist of nodes that form a rooted tree, meaning it is a directed tree with a node called *root* that has no incoming edges. All other nodes have exactly one incoming edge. A node with outgoing edges is called an *internal* or *test* node. All other nodes are called leaves, also known as terminal or decision nodes (see Fig. 5.5. In a decision tree, each internal node splits the instance space into two or more sub-spaces according to a certain discrete function of the input attributes values. In the simplest and most frequent case, each test considers a single attribute, such that the instance space is partitioned according to the attribute's value. In the case of numeric attributes, the condition refers to a range.

Each leaf is assigned to one class representing the most appropriate target value. Alternatively, the leaf may hold a probability vector indicating the probability of the target attribute having a certain value. Instances are classified by navigating them from the root of the tree down to a leaf, according to the outcome of the tests along the path.

The varieties of T models considered in this thesis include Fine Tree (T_1), Medium Tree (T_2) and Coarse Tree (T_3). What differentiates each version of Decision Tree from the other is the maximum number of partitions per variable which is 4, 20 and 100, respectively.

Several advantages of the Decision Tree Model have been emphasized in the literature. Firstly, Decision Trees are self-explanatory and when compacted, they are also easy to follow. In other words, if the decision tree has a reasonable number of leaves, it can be easily understood by a non-expert. The representation is rich enough to handle discontinuous response surfaces which may be desirable in some applications, especially in electrical machines where some of the variables are discrete. Also, Decision Tree models are capable of handling datasets that may have errors or may have missing values.

On the other hand, Decision Tree models have some disadvantages too. For example, most of the algorithms require that the target attribute will have only discrete values. As the Decision Tree use the divide and conquer method, they tend to perform well if a few highly relevant attributes exist, but less so if many complex interactions are present. Also, the greedy characteristic of T models leads to another drawback that should be pointed out. This is its over-sensitivity to the training dataset to irrelevant attributes and to noise.

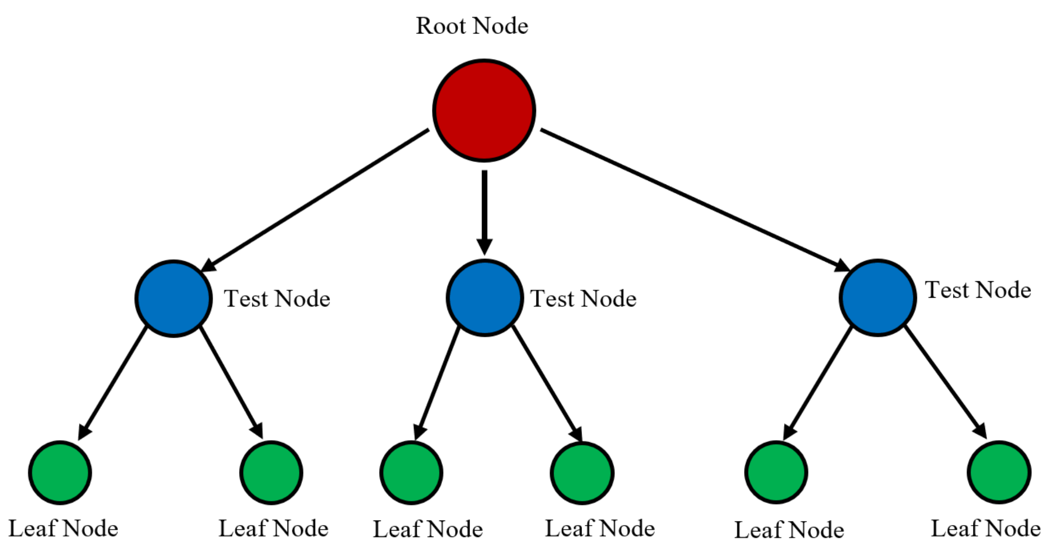

Fig. 5.5 Decision Tree representation

5.4.3 Support Vector Machines

Support Vector Machines gained particular momentum during the last two decades since Vapnik (1995, 1998) published his well-known textbook on statistical learning theory with a special emphasis on Support Vector Machines. Since then, there has been intense activity in the study of Support Vector Machines, which has spread more and more to various areas of engineering [120].

Although Support Vector Machines have witnessed lots of modifications over the years, the fundamental concept remains the same. Basically, we are looking for the optimal separating hyperplane between two classes by maximizing the *margin* between the classes' closest points. Margin means the maximal width of the slab parallel to the hyperplane that has no interior data points (see Fig. 5.6. The points lying on the boundaries are called *support vectors*, and the middle of the margin is our optimal separating hyperplane. Data points on the wrong side of the discriminant margin are weighted down to reduce their influence. When we cannot find a linear separator, data points are projected into an (usually) higher-dimensional space where the data points effectively become linearly separable. This projection is realised via kernel techniques. The kernels used are Linear (SVM_1), Quadratic (SVM_2), Cubic (SVM_3), and Gaussian [12]. Three scales were employed for the Gaussian kernels: $\sqrt{\mathrm{P}}/4$ for the Fine (SVM_4), $\sqrt{\mathrm{P}}$ for the Medium (SVM_5), and $4\sqrt{\mathrm{P}}$ for the Coarse (SVM_6), where P is the number of input variables.

The whole task can be formulated as a quadratic optimization problem which can be solved by known techniques. A program that is capable of performing all these tasks is called a Support Vector Machine. A Support Vector Machine finds a function, f(x), as flat as possible, that deviates from the observed response by a value less than the tolerance, ε, for each training point x. Thus, Support Vector Machines do not care about errors if they are less than ε but will not accept any deviation larger than ε.

Although Support Vector Machines have become very popular, there are some drawbacks. SVMs scale rather badly with the data size due to the quadratic optimization algorithm and the kernel transformation. Furthermore, the correct choice of kernel parameters is crucial for obtaining good results, which practically means that an extensive search must be conducted on the parameter space before results can be trusted, and this often complicates the task [121].

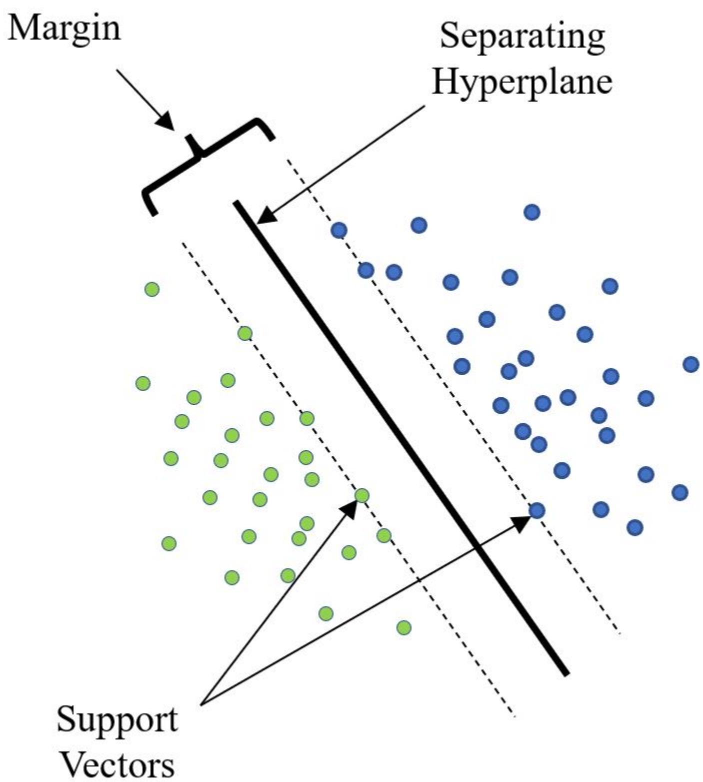

Fig. 5.6 Classification (Linear seperable case)

5.4.4 Gaussian Process Regression Models

The concept of Gaussian process has been exploited by many researchers in various ways for decades. Gaussian Process Regression have also been used in numerous applications for many years, for example, in spatial statistics under the name of *kriging*. The GP models express the sought, unknown, function $y(\mathrm{x})$ as a combination of a global model, f(x), with local deviations, Z(x). The f(x) approximates the global trend of the original function while Z(x) creates local deviations to approximate a possible multimodal behavior. Mathematically, Z(x) is the realization of a stochastic process with zero mean, variance, σ^2, and covariance given by (5.8).

$$\mathrm{Cov}[\mathrm{Z}(\mathrm{x_i}), \mathrm{Z}(\mathrm{x_j})] = \sigma^2 \mathrm{R} \tag{5.8}$$

R is the correlation matrix of all the sample data defined in (5.9). Here, $\mathrm{R}(\mathrm{x_i}, \mathrm{x_j})$ is some covariance function which expresses similarity, and f(x) is taken as a constant which corresponds to the mean of the sample data.

$$\mathrm{R} = \begin{bmatrix} \mathrm{R}(\mathrm{x_1}, \mathrm{x_1}) & ... & \mathrm{R}(\mathrm{x_1}, \mathrm{x_n}) \\ \vdots & \ddots & \vdots \\ \mathrm{R}(\mathrm{x_n}, \mathrm{x_1}) & ... & \mathrm{R}(\mathrm{x_n}, \mathrm{x_n}) \end{bmatrix} \tag{5.9}$$

The covariance function, $\mathrm{R}(\mathrm{x_i}, \mathrm{x_j})$, can take many forms: Squared Exponential or Kriging ($\mathrm{GP_1}$), Matern 5/2 ($\mathrm{GP_2}$), Exponential ($\mathrm{GP_3}$), and Rational Quadratic ($\mathrm{GP_4}$). The maximum-likelihood method is used to find the parameters, which means that a non-linear optimization problem is solved involving the inverse of the correlation matrix. For this reason, their training time tends to be much higher when compared to the other models.

5.5 Implementation of Selected Surrogate Models

To formulate the surrogate problem, two (2) modelling approaches have been proposed: (i) Global Surrogate Modeling (GSM), and (ii) Local Surrogate Modeling (LSM). The GSM and LSM are implemented in the following sections.

5.5.1 Global Surrogate Modeling

The GSM encapsulates the three (3) underlying domains of physics, i.e., the electromagnetic subsystem, the structural subsystem and the acoustic subsystem, giving an overall insight into the functional relationship between predictors-response pairs.

The GSM is constructed using a motor geometry and the motor speed as input to the model. The corresponding $\mathrm{P_{SL}}$ is the model's response variable. The motor speed ranged between 100-4000 RPM. In total, 80 motor speed points were used to create a sample database. This resulted in 80 operating speed points × 3000 motor designs = 240 000 data samples. Fig. 5.7 illustrates the concept. Here, $\mathrm{x_1}$,...,$\mathrm{x_{10}}$ represents the design variables of the motor geometry, $\mathrm{N_m}$ is the operating speed selected at random, and ε denotes the error term, which signifies the deviation from the actual $\mathrm{P_{SL}}$ response. The electromagnetic, structural and acoustic subsystems are denoted EMS, STS, and ACS respectively.

The Global Surrogate Model has been implemented using the four (4) classes of models, and each model has about 3-4 variants, details of which have been explained in Section 5.4. In all, an ensemble of 17 metamodels were implemented. Each model has been constructed using random samples from a training dataset. The dataset has been carefully chosen to avoid clustering in the acoustic design space by using the LHS sampling plan. A standard holdout validation scheme was applied to calibrate each of the trained surrogate models. The samples not used in calibrating the surrogate models formed part of the test set.

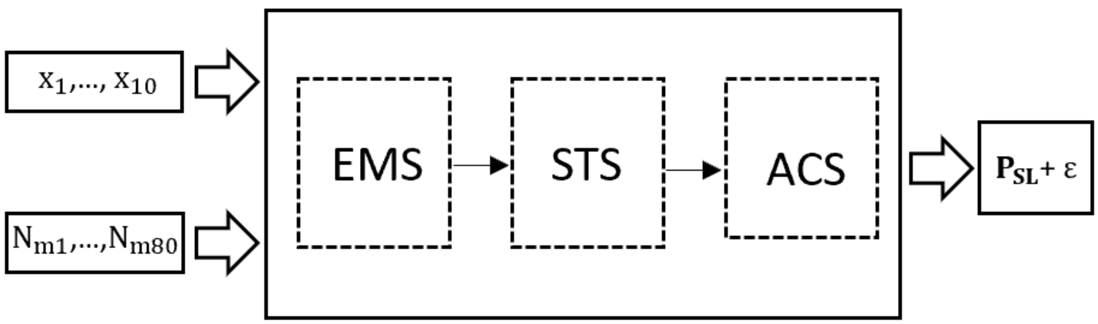

Fig. 5.7 Implementation of GSM concept.

5.5.2 Local Surrogate Modeling

The LSM tries to fit a model to each subsystem independently and relies on the predicted responses as input to an acoustic model. For the EMS, each design and its corresponding magnetic pressure harmonic number constitutes the input to the LSM model. The output of the EMS is the magnetic pressure harmonic amplitude. For the STS aspect, a sample comprises a motor design and the first 10 vibration modes as predictor variables and the first 10 natural frequencies as the response variable. For the ACS, the analytical formulation in [97] has been applied. Hence, fitting a model to ACS was irrelevant.

The procedure for the training, validation and testing of all the surrogate models in LSM is the same as the approach used in Section 5.5.1. The implementation of the proposed LSM concept is described in Fig. 5.8. Here, $\mathrm{H_n}$ is the harmonic number, $\mathbf{m}_\mathrm{n}$ is the vibration mode, and the $\varepsilon_1+\varepsilon_2$ error term denotes the cumulative deviation from the actual response.

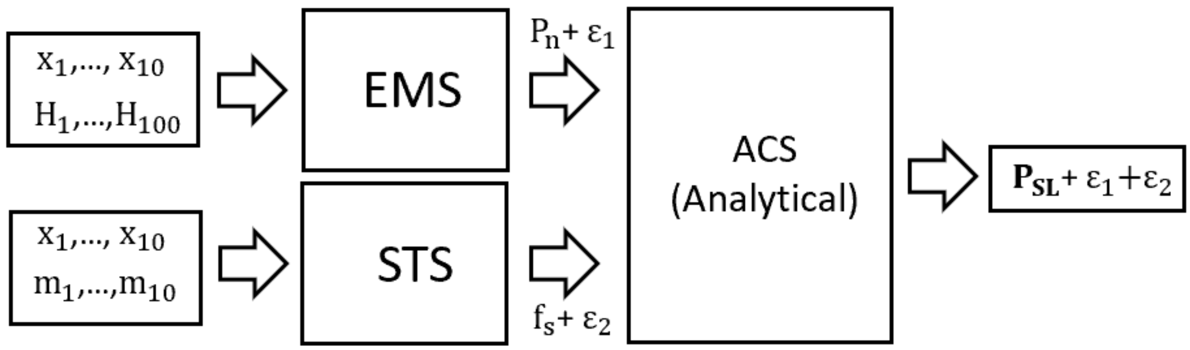

Fig. 5.8 Implementation of LSM concept.

5.6 Results and Discussion

Two of the performance metrics explained in Section 5.3.3 have been used to rank the skill of each surrogate model: the Root Mean Squared Error in dB, and the Coefficient of determination value. The training time (TT) in seconds, and the evaluation speed (N) in samples per second have also been used to evaluate the performance of the models against that of the finite element simulations. As mentioned earlier, the RMSE is the most important metric for assessing the competence of surrogate models. The lower the RMSE value, the smaller the error deviation which indicates a better fit. The R^2 values suggest how well the model fits the response data.

In general, a surrogate is considered a suitable model if it has the following attributes: (i) It must be able to produce accurate estimates of the underlying complex patterns of the actual response variable, and (ii) the model must be cheaper to train and use than to generate each solution using the high-fidelity model. Table 5.1 uses the RMSE values to screen for the best surrogate models that have been implemented in GSM.

To find the optimal number of samples for training the models, the dataset is divided into 1k, 5k, 10k and 50k samples. As the training dataset increases, the model's competence improves but at a higher cost of training. Refer to Fig. 5.9 for the effect of varying the training sample size on the RMSE values for different models. On average, the training time for L models are 0.02 min, 0.03 min, 0.33 min and 0.51 min; 0.02 min, 0.05 min, 0.37

min and 0.55 min for T models; 0.03 min, 0.35 min, 1.53 min, and 27.8 min for SVMs; and 0.65 min, 5.83 min, 9.9 min, and 581 hrs for GP models respectively.

The Gaussian Process Regression Models were the most suitable candidates for GSM. However, training those models can be very costly as explained in [72]. The best model, GP_3, took 64 hrs to train with 50k samples, improving its RMSE value from 0.639 dB to 0.04 dB. The Tree models offer the best tradeoff between accuracy and training time. The Linear regression models were the cheapest overall in terms of training time, but their error estimates were largest. Support vector machines performed much better than the Linear regression models. The SVM_4 went from being the overall worst model for 10k samples to being the best performer in its class when 50k samples were used. Due to this peculiarity, it was expected that extending the sampling size to 200k could improve the accuracy of the cheaper models. However, it is demonstrated that beyond 50k, RMSE values tend to saturate. At 200k, the RMSE values for T_1-T_2, and SVM_3-SVM_5 had very little impact.

In terms of R^2, all the SMs implemented in GSM, except Linear Regression Models showed increasing trends reaching values above 0.9. This means that the models were capable of fitting well to over 90% of the response data. The rapidity of the models in predicting results, however, demonstrated a decreasing trend as the training sample size increased (refer to Table 5.2 for observations on R^2 and N). The reason being that the models' hyperparameters which control the learning process, grow in complexity as the training sample size increases. The N depends on the complexity of the hyperparameters. On average, L and T models can predict 1-2 million samples per second. The slowest model, GP_4, for 50k, has an evaluation speed of 788 samples per second which translates to around 1.27 milliseconds per sample. This is a clear improvement for this model compared to using FE simulations, which take around 20 minutes to predict P_{SL} for each sample. Even though training GP_4 can be arduous, this occurs only once, and the generated functions can be used again, especially for future design and optimization routines.

For the LSM, only the results for the optimal training dataset of 50k samples are shown in Table 5.3. It must also be stated that only the best performing models in each of the four (4) classes of SMs are presented for discussion. The Decision Tree Models offer the lowest propagation error in terms of using the predicted responses as inputs to the acoustic model. The reason being that Decision Tree Models generate a piecewise constant estimate of the quantity of interest which relates to the provided dataset. The other models assume that the analyzed quantity is continuous and smooth. This assumption is incorrect since

P_n and f_s are discrete values, thereby compromising the accuracy of the models. T_1 can still guarantee reasonable P_{SL} estimates due to their relatively lower RMSE values of 705 Pa and 147 Hz respectively. Nevertheless, the other models may not produce comparable results due to larger error estimates. For example, in the case of L_4, a spectral RMSE shift of 2180 Hz in the vibration modes can wrongfully trigger a resonance phenomenon in the stator structure which can exaggerate the sound power levels.

In Fig. 5.10, the Decision Tree Model, T_1, which offers the best tradeoff in terms of RMSE, TT, and N, has been used to draw a comparison between GSM and LSM. The abscissa axis represents the P_{SL} observations for the high-fidelity model, in this case the FE simulation results, while the ordinate axis represents the predicted P_{SL} observations from T_1. The datum line (see red dotted diagonal line) measures the deviation from the high-fidelity P_{SL} response. If the observations are clustered around the datum line, it means that the prediction error is very small and vice-versa. At a glance, it is patently clear that the P_{SL} observations for LSM are sparsely spaced around the datum line compared to that of the GSM, whose P_{SL} observations are tightly gathered around the datum line. Clearly, the cumulative error term, $\varepsilon_1+\varepsilon_2$, accounts for the sparse distribution in the acoustic space.

In conclusion, the lower RMSE values in the case of GSM indicated the models' capability to predict acoustic noise. The models' performance, however, degraded in LSM due to the nature of the subsystems' data distribution and the cumulative error propagation. The Decision Tree Models offered the best overall tradeoff for RMSE, TT and N. The accuracy of the models depended on the size of the training dataset. However, the models themselves already rely on expensive finite element simulations to build, which is a major drawback. But once these models are built, they can be reused for future problems.

5.6.1 Conclusions on the Application of Surrogate Models in Acoustic Noise

Developing simpler models that can rapidly and accurately encapsulate the multi-physics effects is the main objective of this chapter. But the ultimate goal is to incorporate these models in the design and optimization cycle of the electrical machine where hundreds, if not thousands, of potential design candidates may be evaluated. Some of this work has been implemented since the main thesis work was completed. For example, in reference [122], optimized surrogate models were developed and applied to the design of an inverter-fed interior permanent magnet synchronous motor.

This work, therefore, is a fundamental step towards establishing a more generalizable trend in the future where it will be extended to cover a wide range of other motor design topologies. The issue of the generalizability of surrogate models remains a potential research problem and can be addressed by developing a scalable model and/or a normalized input vector of the training dataset.

Table 5.1 Metadata of Global Surrogate Models I

Model	Root-Mean Square Error [RMSE]					Training Time [sec] [TT]			
	1k	5k	10k	50k	200k	1k	5k	10k	50k
L_1	1.12	1.10	1.11	1.11	-	1.53	1.67	18.34	18.3100
L_2	1.06	1.04	1.04	1.04	-	1.03	2.67	20.36	37.5100
L_3	1.11	1.10	1.10	1.10	-	0.89	1.40	19.96	36.7400
L_4	1.06	1.04	1.04	1.04	-	80.01	209.51	437.87	1787.70
T_1	0.95	0.54	0.33	0.12	0.09	0.59	4.87	23.86	42.5100
T_2	0.94	0.68	0.49	0.19	0.10	1.94	2.07	22.00	28.7800
T_3	1.02	0.81	0.69	0.36	-	1.84	1.93	21.63	27.9400
SVM_1	1.12	1.10	1.10	1.09	-	1.73	9.49	49.98	680.280
SVM_2	0.77	0.68	0.67	0.66	-	1.56	15.87	70.56	1107.07
SVM_3	0.69	0.58	0.56	0.53	0.53	1.90	30.44	103.86	1940.80
SVM_4	1.41	0.98	0.66	0.18	0.15	1.79	18.78	91.34	1781.80
SVM_5	0.72	0.52	0.44	0.30	0.20	2.17	27.27	120.25	2169.10
SVM_6	1.07	0.94	0.84	0.68	-	3.27	24.76	115.17	2327.40
GP_1	0.66	0.46	0.37	0.06	-	18.81	231.04	426.46	141100
GP_2	0.62	0.31	0.16	0.05	-	33.19	254.43	495.85	716000
GP_3	0.64	0.35	0.21	0.04	-	28.21	262.84	489.04	230111
GP_4	0.61	0.31	0.16	0.05	-	76.12	650.21	985.00	1007200

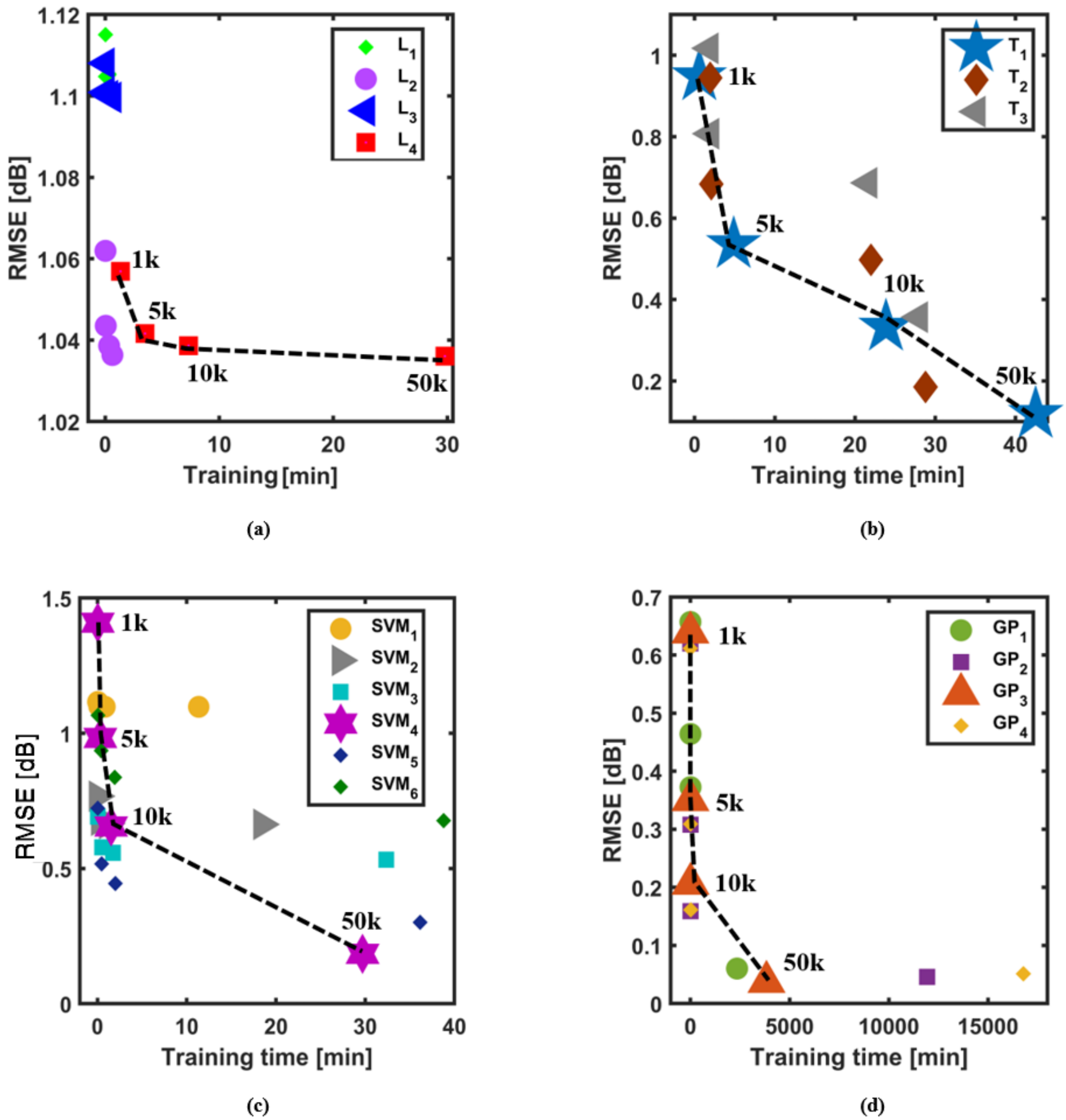

Fig. 5.9 Performance vs training time for all tested models (a) Linear Regression Models (L_n) (b) Tree Model (T_n) (c) Support Vector Machines (SVM_n) (d) Gaussian Process Regression Models (GP_n).

Table 5.2 Metadata of Global Surrogate Models II

Model	Coefficient of Determination [R^2]					Sample Evaluation Speed [N]				
	1K	5K	10K	50K	200K	1K	5K	10K	50K	200K
L_1	0.46	0.47	0.47	0.47	-	1.6M	1.3M	1.1M	1.6M	-
L_2	0.51	0.53	0.54	0.54	-	1.6M	522k	486k	540k	-
L_3	0.46	0.47	0.47	0.47	-	1.7M	1.6M	1.2M	1.7M	-
L_4	0.51	0.53	0.54	0.54	-	1.1M	837k	717k	362k	-
T_1	0.60	0.83	0.94	0.99	1.00	2.2M	1.9M	1.9M	1.5M	1.M
T_2	0.61	0.77	0.88	0.98	1.00	2.1M	2.0M	1.8M	1.9M	1.5M
T_3	0.55	0.71	0.78	0.94	0.99	2.2M	2.0M	2.2M	1.9M	1.9M
SVM_1	0.46	0.47	0.47	0.46	0.70	725k	123k	81.7k	14M	669
SVM_2	0.73	0.79	0.80	0.79	0.89	660k	88k	61.5k	9.1k	573
SVM_3	0.78	0.84	0.85	0.85	0.93	555k	84k	57.0k	8.9k	605
SVM_4	0.76	0.55	0.77	0.99	0.99	281k	31k	21.8k	9.2k	8216
SVM_5	0.75	0.86	0.89	0.95	0.99	263k	34k	27.8k	5.3k	1818
SVM_6	0.50	0.61	0.69	0.79	0.90	289k	28k	18.4k	3.8k	504
GP_1	0.80	0.90	0.93	0.99	-	94k	17k	8.8k	1.8k	-
GP_2	0.80	0.93	0.98	0.99	-	49k	11k	5.71	1.1k	-
GP_3	0.80	0.92	0.97	0.99	-	73k	15k	7.8k	1.4k	-
GP_4	0.81	0.93	0.98	0.99	-	38k	7.6k	4.0k	788	-

Table 5.3 Metadata of Best Local Surrogate Models

Model	Electromagnetic Subsystem				Structural Subsystem			
	RMSE	R^2	N	TT	RMSE	R^2	N	TT
L_2	4375	0.53	460k	0.4	-	-	-	-
L_4	-	-	-	-	2180	0.82	350k	0.8
T_1	705	0.95	810k	0.7	147	0.99	160k	0.4
SVM_3	882	0.94	200	176	-	-	-	-
SVM_5	-	-	-	-	1432	0.92	2.5k	1.7
GP_2	4070	0.59	81	461	1351	0.93	820	15

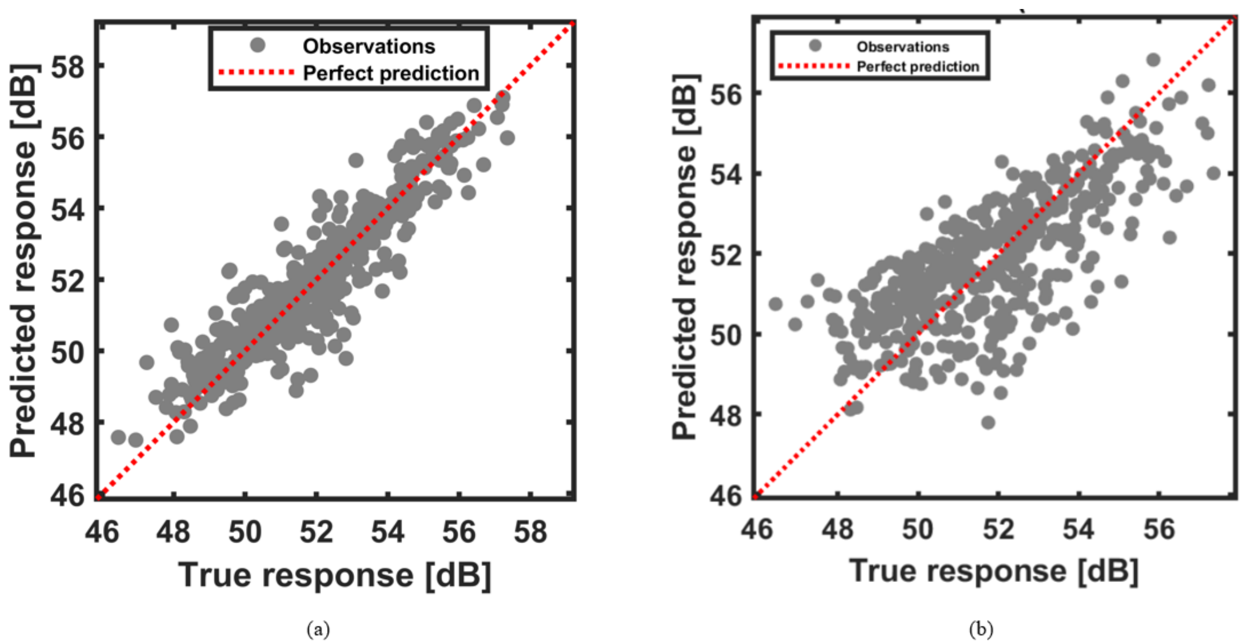

Fig. 5.10 True response vs predicted response in dB (a) Global Surrogate Model (GSM) scatter plot (b) Local Surrogate Model (LSM) scatter plot.

Chapter 6

Conclusion

This chapter recapitulates the major contributions of this thesis. It is organized as follows: First, a summary of the main chapters is given in Section 6.1; Next, a general discussion that clearly outlines the wider impact of this work is also presented in Section 6.2; Finally, the author explores some of the limitations of this thesis, and other well-known design challenges to lay the groundwork for future works in Section 6.3.

6.1 Summary of chapters

Chapter 1 equipped the reader with the fundamental concepts and relevant acoustical terminologies needed to understand the thesis. It also explored the effects of noise pollution and the standards that various governments have institutionalized to regulate PELs. A brief summary of electrical machine noise has been presented, followed by an overview of the taxonomy of electrical machines where the IPM motor is emphasized as the benchmark model for this work. The chapter also reviewed the current state-of-the-art research in vibro-acoustics in an effort to develop a plan for further studies.

In Chapter 2, the procedure for casting acoustic noise as a multiphysics problem using analytical, numerical, and experimental models were explained with special emphasis on the finite element method. Some of the general challenges that hamper the accuracy of the acoustic noise results were also reviewed.

Chapter 3 studied the effect of non-sinusoidal current waveform on the noise emitted by the machine. It demonstrated that sampling the air gap space for the electromagnetic forces could be done more effectively using the Multiple Time Sampling approach. Two new metrics namely Average Sound Power and Ripple Sound Power Levels were also introduced to augment the existing metrics. The Average Sound Power calculates the average of the sound power at every sampled point along the air gap space. The Ripple Sound Power also accounts for the difference between the highest crest and the lowest trough in the instantaneous sound waveform over one electrical cycle.

Chapter 4 incorporated a thermal model in the multiphysics simulation framework. The finite element subsystems were modeled with temperature-dependent material properties of silicon-steel, NdFeB and varnished copper to account for the heating effect. The study showed substantial decrease in both the electromagnetic forces and the natural frequencies at very high temperatures. The behavior of the permanent magnets could be ascribed to demagnetization at elevated temperatures. The reduction in the natural frequencies of the motor resulted in the exaggeration of the noise levels as the modified vibration modes resonated with the exciting frequencies.

In Chapter 5, the computational burden associated with evaluating acoustic noise was addressed using an alternative model referred to as a surrogate model. A wide range of surrogate models were tested on the interior permanent magnet synchronous motor. The performance of these models were quite promising with the Decision Tree model emerging as the best tradeoff candidate in terms of accuracy and prediction speed.

6.2 General Discussion

Undoubtedly, acoustic noise emitted by rotating machines remains a major issue in all regions of the world. Aside from the health implications caused by the loudness and the annoying harshness of the noise, the efficiency of the machine can also reduce since sound is a form of energy. For this reason, noise, vibration, and harshness control must be one of the major performance objectives in the design and optimization of the electrical machine.

NVH assessment is needed early in the design process as the solutions often need substantial modification to the design, forcing in engineering changes which are much cheaper when made early. Remember, these prototypes can be very expensive to build! Hence, there has been great interest in computer aided predictive techniques for noise and vibrations analysis. As mentioned earlier in this thesis, various numerical methodologies exist such as the Finite Element Method and the Boundary Element Method.

Although this thesis does not focus on NVH abatement, it indirectly provides the mitigation guidelines to build quieter machines. For example, where passive noise control is used as the mitigation strategy, the motor designer normally makes changes to the motor's geometry to alter its natural frequencies to avoid resonating with that of the exciting forces. This research however, enlightens the motor designer on the possibility of achieving undesirable results, even with the modified geometry, when the operating temperature of the machine exceeds certain thresholds. The results in Chapter 4 clearly show that the temperature at which the machine operates has a profound influence on its resonant frequencies, and that they are bound to change drastically when the machine continues to operate at very high temperatures.

A lot of companies today are doing serious damage to their brands or losing millions of dollars via product recalls and payment of customer warranties due to defects that went unnoticed in the design process. With rapid prediction models such as the surrogate model, these huge losses could be minimized or completely averted. Defects such as loudness can be identified and solved even before the product goes into commercial production. Also, surrogate models can also make design modifications much easier since they allow the motor designer to by-pass most of the computationally-intensive multiphysics simulations.

Most modern electrical machines are no longer driven from a purely sinusoidal AC supply. The electric motors used in variable speed applications are often driven by power electric drive systems. These systems supply the stator with non-sinusoidal current. As at the time of writing this thesis, the existing models for characterizing acoustic noise arising from non-sinusoidal excitation could not accurately account for the electromagnetic forces due to the switching effect of the power electronic circuit. With the proposed sampling technique and the new acoustic quantities introduced in Chapter 3, the motor designer is able to gain more insight into the electromagnetic force components and accurately quantify the noise levels.

Although the above discussions validate the relevance and usefulness of this thesis, there are, however, some limitations to this work. Some of the limitations of this research will be addressed in future works.

6.3 Future work

The work presented in this thesis is a fundamental step towards a complete understanding of the complex multiphysics design and optimization process. However, it is restricted to acoustic noise and specific to the interior permanent magnet synchronous motor. Below are some avenues for future research and improvements:

- **Address limitations discussed in Sections 3.5 and 4.2**: This means introducing some degree of rotor eccentricity in the models to account for manufacturing imperfections. It can also incorporate the effect of magnetostriction in the core materials, and modeling the stator core laminations to further improve upon the accuracy of the prediction models. Some works on the effect of modeling the stator core as thin sheets of electrical steel laminates have already been published. See reference [123].

- **Streamline coupling between subsystem models**: Improve upon the finite element simulation results by modeling the acoustic noise in a single multiphysics simulation environment where all the finite element solvers, i.e., the electromagnetic and vibro-acoustic solvers, are present. The challenge, however, lies in finding a competent software package capable of handling such complex fully-coupled multiphysics simulation chain.

- **Improve generalization of models's performance**: The predictions of some of the surrogate models are arguably accurate enough to be applied in the design process. However, without training on new data, the models do not generalize to unseen motor geometries. The models should be able to intelligently fine-tune their hyperparameters to adjust to an entirely new motor geometry. Hence more work needs to be done to make the models generalizable. For example, a surrogate model trained on an IPM motor must be able to perform predictions on an induction motor.

- **Compare simulation results with benchmark**: Although industry standard simulation tools are used for this work, the author intends to validate the finite element results with actual test results. This will establish some level of confidence and credibility in the work. The 4Pole 12Slot IPM motor which is used throughout this thesis has already been built and available in the CEMLab for this task.

Appendix A

Acoustic Noise Metrics & Electrical Machine Classification

A.1 Sound Waves

Sound waves are small-amplitude adiabatic oscillations that are generated by a vibrating body. Sound waves fall into three (3) categories covering different ranges of frequencies.

- **Audible sound waves**: These lie within the normal range of hearing of the human ear. The human ear perceives frequencies between 20 Hz (lowest pitch) and 20 000 Hz (highest pitch). Acoustic vibrations outside of this field are not considered as *sounds*, even if they can be perceived by other animals.
- **Infrasound waves**: The American National Standards Institute (ANSI) defines sound at frequencies less than 20 Hz as *infrasound*. At very high levels, infrasound can be very lethal to humans. Our internal organs resonate at frequencies between 5 and 15 Hz. This is why, when the sound level is high enough, sounds dominant in this frequency range cannot be heard but can be felt as vibrations in our bodies. This vibration of internal organs may damage these tissues and cause circulatory and stress-related illnesses. Infrasonic frequencies, however, are useful for monitoring seismic activities and volcanoes, and petroleum formation below the earth.
- **Ultrasound waves**: These are sound waves with frequencies greater than 20,000 Hz (ANSI). Unlike infrasound, ultrasound attenuates rapidly with distance from the

source and therefore is usually not dangerous unless a person is in contact with a high-level beam source. Low levels of ultrasound are used extensively in the medical profession to view internal organs, blood flow, and fetuses without any harm.

The hearing range of every animal species is different. Compared to some animals, the audibility range for humans is quite small. For example, a dog's hearing range is approximately twice as wide. Dogs typically can detect sounds between 50 Hz and 46 000 Hz, but are deaf to anything below 50 Hz. Other animals can hear frequencies far into the ultrasonic range. Some dolphins and bats, for example, can hear frequencies up to 130 000 Hz. Animals such as whales, elephants and hippopotamus use infrasound to communicate over distances. The audio frequency range for some species are shown in Table A.1 [124].

Audibility Range for Different Animal Species

Species	Range [Hz]	Species	Range [Hz]	Species	Range [Hz]
Human	20 - 20,000	Mouse	1,000-100,000	Dolphin	1,000-130,000
Dog	50 - 46,000	Horse	55 - 33,500	Whale	10 - 20
Cat	30 - 50,000	Chimpanzee	100 - 20,000	Snake	100 - 800
Rat	1,000 - 60,000	Elephant	14 - 16	Frog	100 - 3,000
Rabbit	300 - 45,000	Goldfish	100 - 2,000	Chicken	125 - 2,000
Pigeon	200 - 10,000	Bat	3000-120,000	Owl	200 - 12,000

A.2 Basic Acoustic Quantities: Decibels and Levels

Every discipline has its own esoteric language that sets its experts apart from the rest of the population, and acoustics is no exception to the rule. In addition to its own language, sound assessment also has a different mathematical way of describing its parameters. The intent of this section is to break through these language barriers and provide the most relevant information (and terminologies without high-level theory or mathematics) that would be needed to understand noise issues from a practical viewpoint.

A.2.1 The History of Decibel: The Unit of Sound

Early in the history of the telephone, it was decided to adopt logarithmic scales for representing acoustic quantities encountered in electrical equipment. So, in 1928, scientists at Bell Laboratories unanimously agreed on Decibel (dB), which was originally called Transmission Unit. Since then, dB, has become the de facto standard unit of measurement of sound for the sake of convenience [125]. As a result, Sound Power, Sound Pressure, and Sound Intensity from electro-acoustic transducers are commonly stated in terms of dB.

So, what are decibels? The key point is that a dB value on its own is nothing, is literally meaningless. This is because a dB is, fundamentally, a ratio. A ratio of some current quantity to some predefined reference quantity. For dB to mean anything, the reference level must therefore be stated explicitly. Typically, when it comes to sound, the reference is the minimum sound that an average human with normal hearing can perceive at 1000 Hz, which is 0 dB. This value is known as the Absolute Threshold of Hearing. ATH is generally reported as the RMS sound pressure of 20 μPa. For vibrations, dB is expressed as a ratio relative to a reference displacement, velocity or acceleration.

In engineering acoustics, whenever a quantity is expressed in dB, the result is known as a Level. Therefore, sound measurement can be expressed as Sound Pressure Level, Sound Power Level or Sound Intensity Level. Sound Pressure Level is mostly used since our hearing mechanism responds to pressure variations.

A.2.2 Sound Power Level

Sound power is the total acoustic power radiated by a vibrating source. It is independent of the surrounding medium. Hence, it cannot be measured by sound meters. Instead, it must be calculated from measurable sound pressure readings. The dB relating the ratio between two sound power sources can be calculated using [3]:

$$\mathrm{P_{SL}} = 10 \log \frac{\mathrm{P_1}}{\mathrm{P_{ref}}} \tag{A.1}$$

where $\mathrm{P_{SL}}$ is the sound power level, $\mathrm{P_1}$ is a known sound power, and $\mathrm{P_{ref}}$ is the reference given by $\mathrm{P_{ref}} = 10^{-12}$ W. $\mathrm{P_{SL}}$ should not be confused with sound pressure level ($\mathrm{L_p}$) or sound intensity level ($\mathrm{P_{SIL}}$), which are also expressed in dB. The $\mathrm{L_p}$ and $\mathrm{P_{SIL}}$ specify the acoustic "disturbance" produced at a point removed from the source.

A.2.3 Sound Pressure Level

Sound pressure is the measurable phenomenon of gradient changes through a medium resulting from a source. This occurrence is what is perceived by the ear. It is roughly proportional to the square root of sound power. Therefore, the sound pressure ratio is roughly equal to the square root of the sound power ratio at a given decibel level. The decibel relationship between two pressures is found using [3]:

$$\mathrm{L_p} = 20 \log \frac{\mathrm{L_1}}{\mathrm{L_{ref}}} \tag{A.2}$$

where $\mathrm{L_1}$ is a known sound pressure in Pascal, and $\mathrm{L_{ref}}$ is the reference sound pressure. Since sound pressure is affected by the distance from the source to the measuring devices, it is important to accurately reflect this distance used during data collection. Most electric motors specifications have standardized on 3 ft (0.91 m) from the motor enclosure as the distance from which sound should be measured.

A.2.4 Sound Intensity Level

Sound intensity is a vector; it allows defining the amplitude and also the direction of the sound. $\mathrm{P_{SI}}$ is the flux of sound energy per unit area. Acoustic intensity corresponds to the average rate of sound energy transmitted through a unit area, perpendicular to the direction of travel of the sound. Mathematically, $\mathrm{P_{SIL}}$ is given by:

$$\mathrm{P_{SIL}} = \frac{1}{\mathrm{T}} \int_0^{\mathrm{T}} pv dt \tag{A.3}$$

where T = period, should be longer than the reciprocal of the lowest frequency of interest; p = instantaneous sound power; t = time; and v = component of instantaneous particle velocity in the specified direction.

A.3 The Hearing Mechanism

The ear is the organ of hearing. Its role in the human anatomy is the reason for all studies and efforts in this thesis. Therefore, it will not be complete without an understanding of how hearing results from the collaboration between the ear and the auditory brain.

A.3.1 Anatomy of the Human Auditory System

The human ear is one of the most intricate and delicate mechanical structures in the human body. It consists of three (3) main parts: the outer ear, the middle ear, and the inner ear. The outer ear includes the pinna, the auditory canal, and the eardrum. Pinna

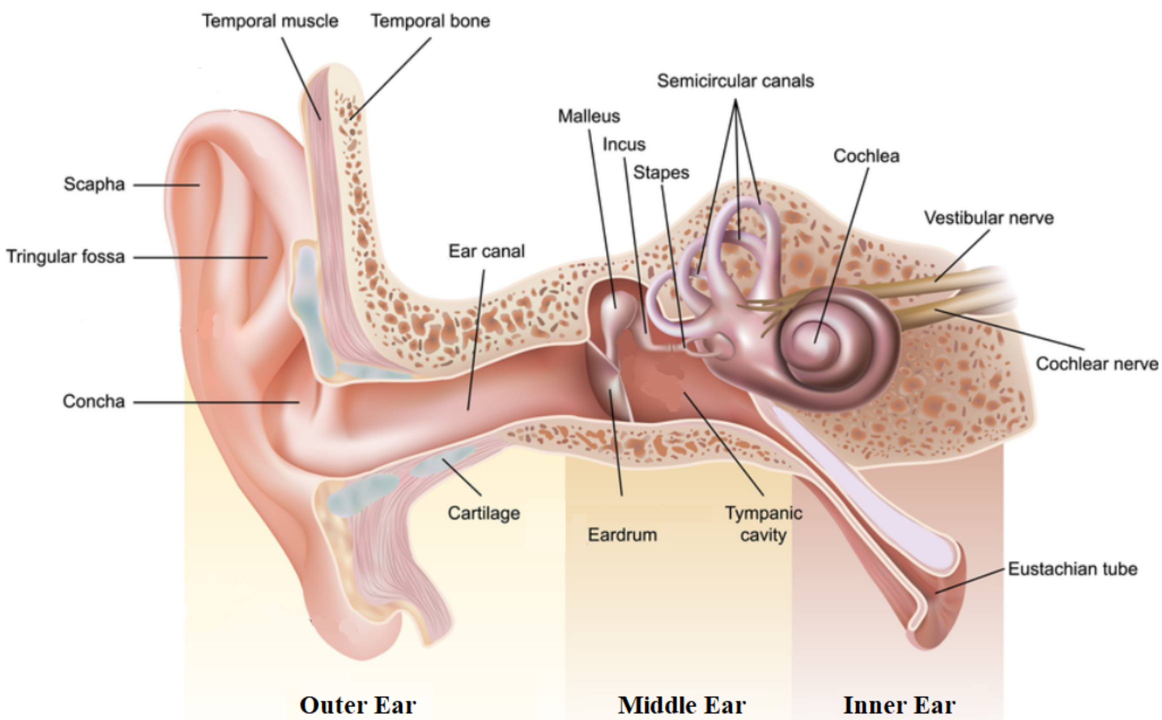

Fig. A.1 Anatomy of the Human Ear [4]

is the visible part of the ear that protrudes from the head. The middle ear contains three tiny bone arrangement: malleus (or hammer), incus (or anvil) and the stapes (or stirrup). Collectively, they are called *ossicles*. The inner ear is made up of the semi-circular canals, and the cochlea. The semi-circular canals are involved in balance and movement. The cochlea is a fluid-filled chamber locked in the skull. Inside the cochlea are very specialized sensory cells called *hair cells*, which are responsible for our remarkable ability to detect very soft sound and tolerate reasonably loud sound. The location of the hair cells in the cochlea dictates the frequency sensitivity of the hair cells. The higher frequency hair cells are closest to the oval window, as would follow from their shortest wavelength. Fig. A.1 above presents the human hearing apparatus broken into the commonly designated segments of outer, middle, and inner ears. The path of the sound signal through this mechanism is discussed next.

A.3.2 How We Hear and the Impact of Noise

Sound signals enter the auditory system through the outer ear, funneled by the pinna and the external ear canal, to the eardrum. As sound strikes the eardrum, it vibrates. This vibration results in movement of the ossicles. As the ossicles move, the stapes presses into a thin membrane of the cochlea known as the oval window, which causes motion of the fluid inside the cochlea. This motion stimulates the top portion of the hair cells, which results in chemical changes that produce nerve impulses. These nerve impulses are carried along the hearing nerve to the brain, where they are interpreted as sound. The fluid vibrations in the cochlea are similar to ocean waves rolling onto a coastline. The farther up the cochlea these waves land, the lower the frequency that is interpreted, because the longer wavelengths represent the lower frequencies [126].

A.4 Fundamental Principles of Rotating Machines

The term "Electrical machine" is broadly used to describe any electromechanical energy converter. As the name implies, such a device can convert electrical energy into mechanical energy and vice versa with the aid of mostly a rotary motion. When the energy flow is from electrical to mechanical, it acts as a "motor", and when the conversion is from mechanical energy to electrical energy, it becomes a "generator". The process is reversible, which means that most electrical machines can take either role; however, a machine that is designed to fulfill one function, e.g., as a motor, is less efficient when used as a generator.

In general, an electrical machine consists of a device having a magnetic circuit in two parts which are separated from one another by an air gap. One part of the machine is stationary and is known as the "stator"; the moving or rotating part is known as the "rotor". The stator core is made of laminated electrical-grade silicon steel to minimize eddy currents induced by the varying magnetic field. The stator coils are usually housed in slots punched in the laminated core. A coil consists of strands of copper wire. The size of the wire is a function of the motor's expected full-load current, insulation type and rated operating temperature. A single coil occupies two slots in the stator (one slot for each side of the coil). Only the portion of the coil in the slots contributes to the magnetic field. The coil sides are connected together by the end turns. The arrangement of coils in the stator slots forms the winding system. In some electrical machines, permanent magnets are used in place of copper coils. Between the slots are the teeth which carry the flux through the winding system. Although the flux is predominantly confined to the teeth, it is important to understand that it links the coils of the winding. The rotor is mounted on bearings that are attached to the stator. Similar to the stator structure, the rotor is comprised of silicon steel lamination and could include magnets, damper windings or a combination of both.

The two parts of the machine are also known as the field system and the armature. The armature is the winding in which e.m.f is induced by virtue of the rotating action of the machine; it is also the part of the machine which includes the main current-carrying conductors of the machine. The field system comprises the windings which develop the magnetic field of the machine. For machines with commutators such as DC machines, the armature is normally the rotor. In most AC machines, the armature winding is on the stator, and is connected to the supply. Thus, the armature may either be stationary or rotating. An example of the architecture of an electrical machine is shown in Fig. A.2

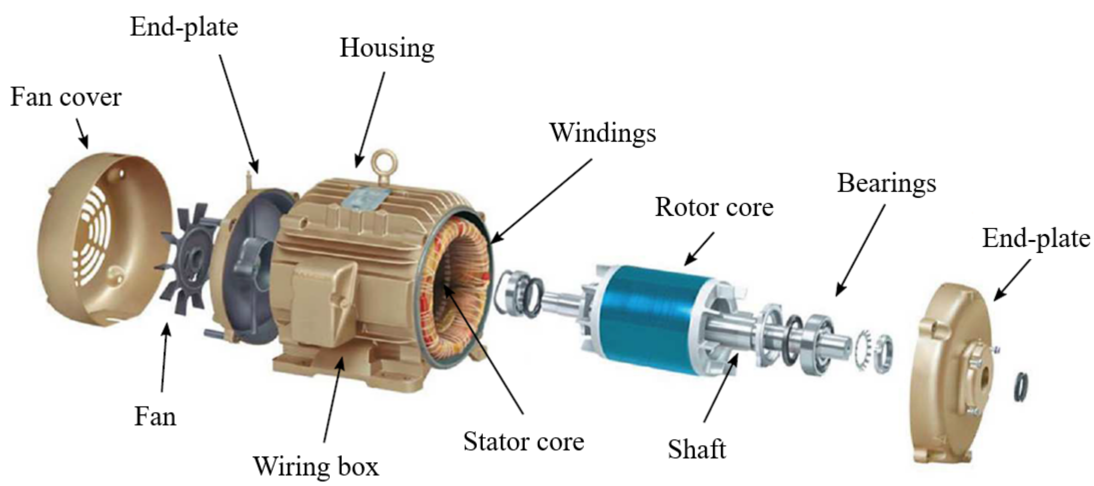

Fig. A.2 An exploded view of an induction motor [5]

A large variety of machine categories emerge from the different combinations of stator slots number $\mathbf{Q}_\mathrm{s}$ and rotor magnetic poles Q_r; the winding arrangement, i.e., whether the stator winding is concentrated or distributed around the core; and how the magnetic fields are generated, and interact with each other to produce torque in the machine. Overall, an electrical machine is conventionally denoted $\mathrm{Q}_\mathrm{s}/\mathrm{Q}_\mathrm{r}$, followed by the machine type. For example, an induction motor (IM) with 24 stator slots and 4 poles is written as "24/4 IM".

In the broadest sense, electrical machines can be divided into AC and DC, depending on the supply involved. However, it is also possible to classify electrical machines as singly-excited or as doubly-excited. In a singly-excited machine, only one member, i.e., either the rotor or the stator, has current-carrying windings; a typical example is the induction motor. The doubly-excited machines have current-carrying windings on both the stator and the rotor; many practical machines are of this type.

It is important to understand how rotational motion is achieved from electromagnetic interactions in the air-gap. Hence the fundamental working principles of the most common motors used in everyday life with the illustration of some of their cross-sections in Fig. A.3, have been discussed in this section. The general taxonomy of electrical machines is presented in Fig. A.4.

A.4.1 DC Machines

From a historical point of view, the DC machine was the earliest electromechanical energy conversion device that heralded the dawn of the electrical age [127]. A DC current carrying armature is connected to the supply end through commutator segments and brushes while the armature is placed between north and south poles of a permanent or electro magnet. The Lorentz force produced generates a rotating motion of the rotor. By means of various combinations of shunt-, series-, and separately-excited field windings, they can be designed to display a wide variety of volt-ampere or speed-torque characteristics for both dynamic and steady-state operations. Therefore, DC machines can be classified as Shunt, Series or Separately-excited. In addition, it is common to see DC motors referred to as "Compound-wound". These descriptions reflect the way in which the field and armature circuits are interconnected, which in turn determines the operating characteristics. For example, the series motor has a high starting torque when switched directly on line, so it is becomes the natural choice for traction applications, while applications requiring constant speed will use the shunt-connected motor.

Permanent magnet versions are also available in motors with outputs from a few watts up to a few kilowatts, while wound-field machines begin at about 100 watts and extend to the largest (MW) outputs. The advantages of the PM type are that no electrical supply is required for the field, and the overall size of the motor can be smaller. On the other hand the strength of the field cannot be varied so one possible option for control is ruled

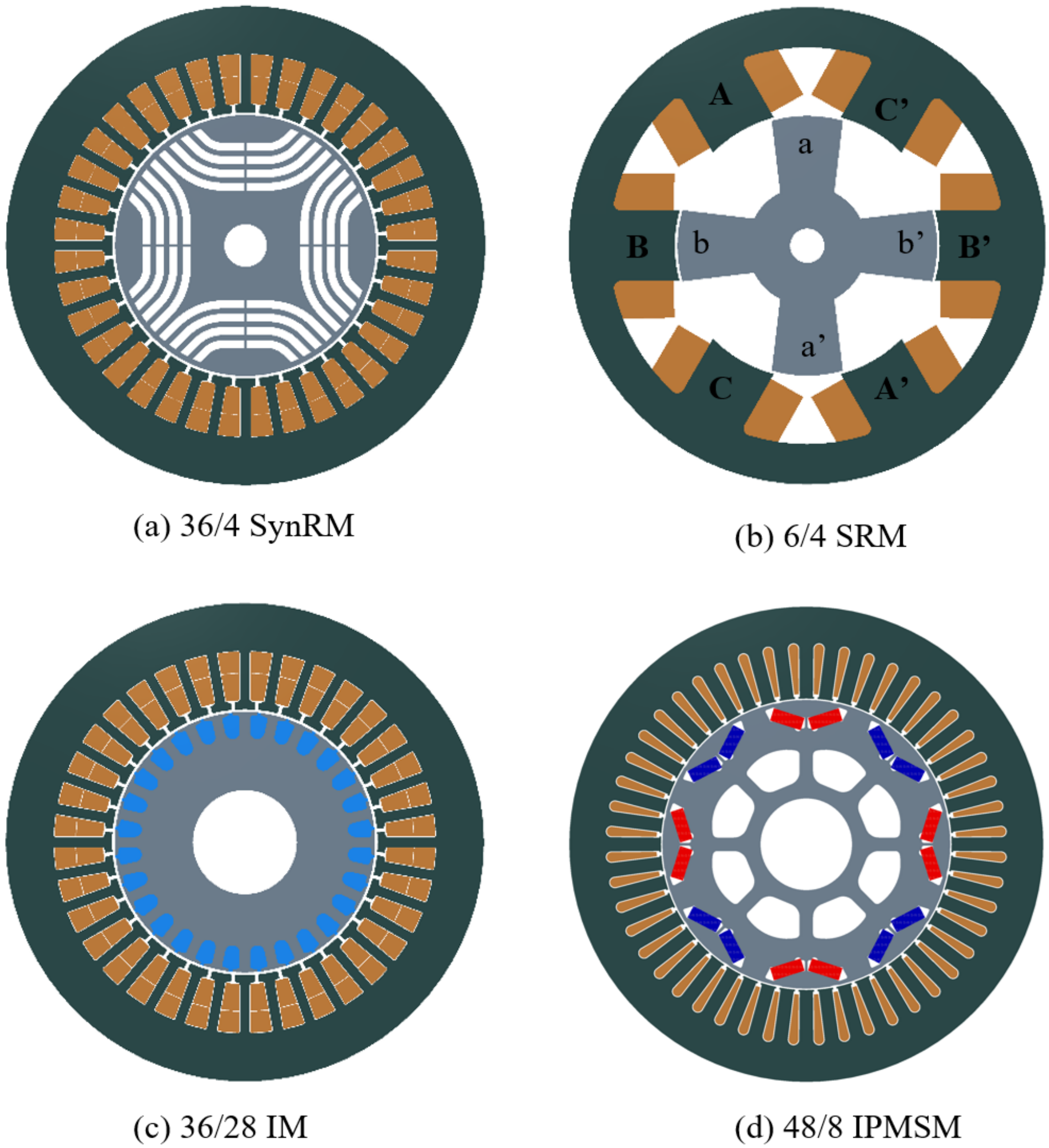

Fig. A.3 Cross-sectional view of motor geometries in Motorsolve [6]

out. Although they benefit from simple control, they suffer from frequent maintenance requirements and low efficiency. Commutators increase torque ripple and limit the motor speed while brushes add friction interferences. The development of power electronics in the last decades made the AC machines more attractive for wide-ranging applications.

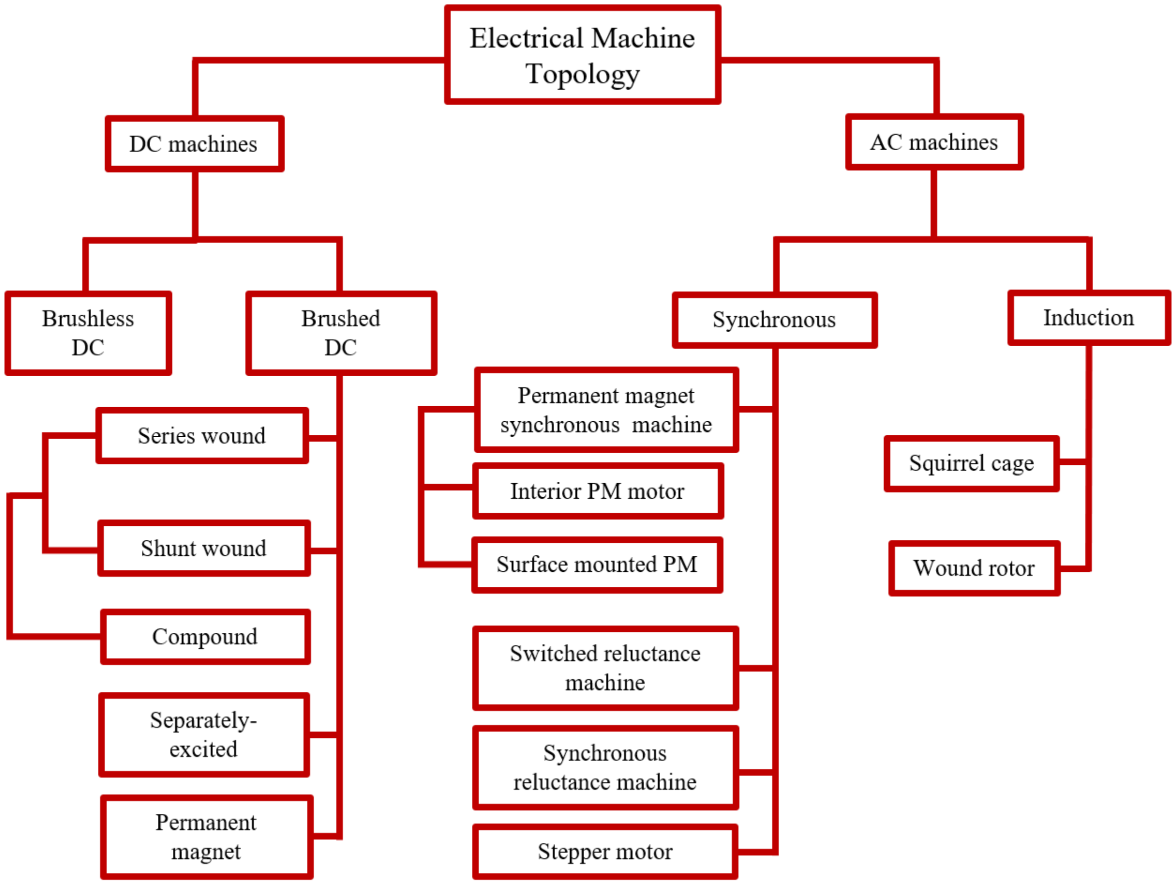

Fig. A.4 Classification of rotating electrical machines

A.4.2 Induction Machines

IMs are the most widely used motor in industrial and commercial utilization of electric energy. Reasons for their popularity include simplicity, reliability, and low cost, combined with reasonable overload capacity, minimal service requirements and good efficiency [127].

The application of AC current to the stator winding results in the appearance of a rotating magnetic flux in the air-gap, which induces currents in the short-circuited rotor windings (by Faraday's law of electromagnetic induction). The induced currents in the rotor (due to the rotating field) interact with the field to produce a torque that rotates the rotor in the direction of the rotating field.

A.4.3 Permanent Magnet Synchronous Machines

The permanent magnet synchronous motor has been widely applied in various fields due to its simple structure, high power density, reliable operation and cooling capacity by removing copper in the rotor. Contrarily to IMs, the rotor magnetic flux is fixed by permanent magnets located inside or outside the rotor structure. It makes the control simple to implement, and sinusoidal (or trapezoidal) multi-phase AC currents can be injected through the stator copper coils to generate the rotating flux.

However, the main drawback is the insufficient rare-earth materials used to manufacture PMs, which influences the cost of PMSMs. Since the excitation is fixed, the designer must either choose the shape and disposition of the magnets to match the requirements of one specific load, or seek a general-purpose compromise. Additionally, PMSMs suffer from the tendency for the magnets to be demagnetized by the high stator current during starting, and from a restricted maximum allowable temperature. The demagnetization problem, however, have been improved through the use of high coercivity rare-earth magnets.

Based on the direction of magnetic flux path, a PMSM can be classified into either a radial-flux, an axial-flux, a linear-flux or a transverse-flux motor [128]. Currently, the majority of the PMSMs used in EVs are radial-flux. However, axial-flux have also drawn some attention and are endowed with a very broad prospects due to the compact structure and high torque/power density. Koenigsegg Regera, for example, is equipped with three axial-flux PMSMs from YASA Motors.

A.4.4 Synchronous Reluctance Machines

The SynRM produces reluctance torque through a magnetically salient rotor structure using flux barriers. Through an ideal set of sinusoidally-distributed coils excited by balanced sinewave currents, a smoothly-rotating stator field is produced in order to force the salient rotor to rotate and align its primary magnetic axis with the stator field. This helps to minimize the overall reluctance path between the stator and rotor structures thereby producing reluctance torque [9].

The biggest difficulty with pure SynRMs, however, is geometrically designing their rotor structure. This presents a major drawback at very high speeds. The centrifugal forces act on the tangential ribs of the rotor,which could potentially cause them to break.

A.4.5 Switched Reluctance Machines

The first reference to the term SRM was made by S. A. Nasar in 1969 [129]. Since then, the SRM has become very popular due to progress in solid state switches. The motor and its associated power-electronic drive system has been applied to a wide range of applications including general-purpose industrial drives, compressors, domestic appliances and office and business equipment [130]. The SRM has a doubly-salient, singly-excited arrangement. Both the stator and rotor have salient poles. The stator carries coils on each pole, while the rotor, which is made from laminations in the usual way, has no windings or permanent magnets and is therefore cheap to manufacture and extremely robust. The stator winding is usually a polyphase winding. The torque is produced by the tendency of the rotor pole to align with the stator pole to maximize the stator flux linkage when the winding of the stator pole is excited by a current.

Figure A.3 (d) shows a cross-sectional view of a SRM (6 stator poles and 4 rotor poles) with three (3) phases. Diametrically opposite stator poles are excited simultaneously. If phase A is excited, rotor poles marked a and $a^{'}$ will be aligned with stator poles marked A and $A^{'}$. If phase B winding is excited, rotor poles b and $b^{'}$ will be aligned with poles B and $B^{'}$ of stator phase B, and therefore the rotor will move clockwise. Thus, if the phases are excited in the sequence A, B, C the rotor will move in the clockwise direction or A, C, B for counterclockwise rotation due to the reluctance torque action which tends to pull nearest rotor pole pair into alignment with the appropriate stator poles. The rotor will move with some synchronism with the stator field, but the motions of the stator field and rotor poles are in opposite directions. The excitation must be switched sequentially from phase to phase as the rotor moves, hence the name switched reluctance motor.

A.5 Deterministic Methods of Acoustic Noise Prediction

In an effort to predict the noise emitted from an electrical machine, there are three (3) main approaches: Analytical, Numerical and Experimental methods. The analytical and numerical methods can be combined to offer the best speed-accuracy tradeoff.

A.5.1 Analytical Method

This approach relies on the equations that govern the machine's geometry to predict acoustic noise. For example, "permeance" and "winding" functions have been used by many researchers to evaluate the air gap flux density [75],[131]. The analytical models of the electromagnetic field are not the main focus of this thesis and will not be elaborated here. The structural model is based on the assumption that the stator is a simplified circular cylinder with both ends free from constraints. Vibration is established based on the vibration theory of a cylindrical shell. The total vibration is obtained by superposing the contribution of each force order, and the sound power emitted by the machine is premised on the assumption that the stator's cylindrical or spherical shape is the radiating surface.

The following simple formulae, (A.4)-(A.6), derived by Jordan, Frohne and Üner [132], which takes into account the effects of shear, rotary inertia, teeth and winding have been used to predict the structural modes. Here, f_m is the m^{th} modal frequency, E is the Young's modulus of the core material, R_m is the mean radius (see Figure A.5), ρ is the density of the core material, h is the core thickness, m is the mode number, and Δ (and Δ_m) is the mass addition factor for displacement (and rotation) defined in [2]. Also, by considering the stator as a purely cylindrical structure, the stator vibrations A_{mr} for vibration mode m can be evaluated using (A.7). Here, F_{nr} is the r^{th} Fourier series amplitude of the radial force, f_{er} is the r^{th} harmonic frequency, f_{sm} is the m^{th} mode of the stator's natural vibration, M_s is the stator mass and ζ_m is the m^{th} harmonic of the damping factor.

The input to the acoustic model is the stator vibrations. The vibration can be in the form of displacement, velocity or acceleration. There are essentially two analytical approaches for calculating the radiated acoustic power, one being based on a cylindrical model of the machine while the other assumes a spherical model. The cylindrical model was first developed by Alger [133], who modeled a machine as an infinitely long cylinder but could not account for its aspect ratio. The spherical model was first suggested by Carter [134], and subsequently developed by Jordan [22]. A further development by Ellison and Moore [135] enabled the effect of an axial variation of the radial vibrations to be determined. However, the spherical model had its limitation: it was suitable for machines having aspect ratio approaching unity only. Zhu and Chen [18] developed a much simpler formula for the acoustic power which depended on the dimensions, the vibration modes and the exciting forces of the electrical machine. In this thesis, (A.8) has been used to evaluate the sound power $\mathrm{P_S}$ in watts emitted by the stator, where ρ_o is the density of air, c_0 is the speed of sound in air and n_p is the number of poles. The sound power level $\mathrm{P_{SL}}$ in decibels is defined by the logarithmic ratio in (A.9), where $\mathrm{P_{ref}}$ is the reference sound power in watts which is equal to 10^{-12} W. The relationship between sound power level $\mathrm{P_{SL}}$ and the mean sound pressure level $\bar{\mathrm{L}}_\mathrm{P}$ on a given measuring surface S is given by (A.11).

The analytical method can solve problems in a few seconds, but the approach performs several simplifications in the motor's geometry and therefore features a lower accuracy. This limits its applicability, and there are quite a number of limitations for this method to be applied in practice. The following are some of the limitations:

- All the analytical methods cited above are mostly applicable to radial-field machines. Analytical models for axial-flux machines are limited.

- The actual boundary conditions of electrical machines are complicated. However, the analytical method can only describe the supporting state of the motor by three kinds of boundary conditions, namely, free, simple and fixed;

- The analytical method is only appropriate for electrical machines with very simple geometry. For machines with complex structure, significant errors could be induced.

Hence, a more accurate model is needed to handle the complex topology of today's ever-evolving electrical machines.

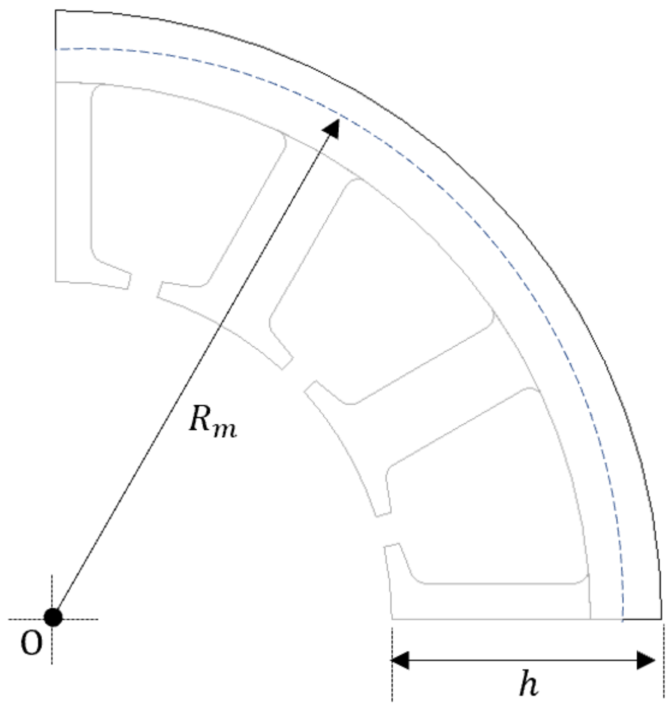

Fig. A.5 $\frac{1}{4}$ stator: $\mathrm{R_m}$ is mean radius, and h is core thickness [3]

$$\mathrm{f_{m=0}} = \frac{1}{2\pi \mathrm{R_m}} \sqrt{\frac{\mathrm{E}}{\rho\Delta}} \tag{A.4}$$

$$\mathrm{f_{m=1}} = \mathrm{f_{m=0}} \sqrt{\frac{2}{1 + (\frac{\mathrm{h}}{2\sqrt{3}\mathrm{R_m}}) \frac{\Delta_\mathrm{m}}{\Delta}}} \tag{A.5}$$

$$\mathrm{f_{m\geq 2}} = \frac{\mathrm{f_{m=0}\ hm(m^2-1)}}{2\sqrt{3}\mathrm{R_m}\sqrt{(\mathrm{m^2}+1) + \mathrm{i^2(m^2-1)(4m^2+m^2}\frac{\Delta_\mathrm{m}}{\Delta}+3)}} \tag{A.6}$$

$$\mathrm{A_{mr}} = \frac{\mathrm{F_{nr}/[(2\pi f_{sm})^2 M_s]}}{\sqrt{[1-(\mathrm{f_{sm}/f_{er}})^2]^2 + [2\zeta_\mathrm{m}(\mathrm{f_{sm}/f_{er}})]^2}} \tag{A.7}$$

$$\mathrm{P_S} = 2\pi\rho_0 \mathrm{c_0 n_p} \sum\nolimits_\mathrm{m} \sum\nolimits_\mathrm{r} \mathrm{A_{mr}} \tag{A.8}$$

$$\mathrm{P_{SL}} = 10\ \log_{10}\left(\frac{\mathrm{P_S}}{\mathrm{P_{ref}}}\right) \tag{A.9}$$

A.5.2 Numerical Method

Numerically, acoustic noise may be formulated using either one or a combination of any of the following: Boundary Element Method (BEM), Finite Element Method (FEM) and Finite Difference Method (FDM). Generally, for calculating the noise radiated into space, the BEM is preferred because only the surface of the motor needs to be discretized and the space does not have to be discretized. The FEM, however, discretizes the space around the motor. The FDM is seldom used for acoustic problems because they are basically only suited for simple and bounded geometries and require large number of calculation points compared with BEM/FEM. It must be emphasized that the BEM and FDM are beyond the purview of this thesis. Hence, by numerical method we mean the finite element method.

The FEM is a computerized model for predicting how a system reacts to real-world phenomena such as forces, vibrations, heat and other physical effects. FEM works by breaking down a complex system into a large number of smaller, simpler parts, such as little cubes, called "elements", the shape and size of which are decided by the user. Then, forces or loads on individual elements are calculated one by one using differential equations. A computer then adds up the behavior of all the individual elements to predict the behavior of the entire system. An appropriate finite-element analysis (FEA) tool must be selected for this job. There are a lot of commercial FEA software packages available on the market for a wide range of applications. For this work, Mentor graphics' interoperable software MotorSolve and Magnet have been used for the electromagnetic aspect [6]. Simcenter 3D Multi-physics, which runs on the Siemens NX software platform has been used to realize the structural and acoustic models [80]. MotorSolve is a motor design software which has a vast model library for many machine topologies. Magnet is more of a general-purpose tool which allows for the modeling and FEA analysis of any low-frequency electromagnetic device. With Magnet, it is easy to control FEA parameters such as mesh density, tolerances for the nonlinear solver, and so on. Simcenter 3D on the other hand, combines several CAE solutions on a unified platform, and takes advantage of integrated industry-standard solvers, such as NX Nastran, for a full range of applications. This integration enables the implementation of a streamlined multi-physical development process.

The first task is to build the CAD geometry based on measured dimensions of a practical machine. Then, a library of the necessary material properties that compose the machine is created. Each component of the CAD geometry is assigned with the corresponding material properties of the machine. Next, the geometry is discretized into finite element domains. This process is called “mesh generation”. Most software packages can generate the mesh automatically. However, it must be defined how the modeled system should be broken down into finite elements. Then, the appropriate constraints such as physical loadings or boundary conditions are applied to the mesh elements. Finally, a solver module is selected based on the analysis type to evaluate the differential equations numerically. The FEM software must understand what kind of solution is expected, i.e., steady state, transient, and so forth. The results can be presented in the form of graphs, contour plots, or tables.

The FEM's capability to mimic realism and delivers deeper insight, ensures accurate acoustic modeling. The accuracy of the FEM results generally depends on the number of elements in the model. The only drawback of the FEA analysis of the fields, however, is that it is time-consuming. Depending on the mesh size, the model's complexity and the type of analysis, the simulation time can run into several hours. Luckily, this issue is being addressed through variant techniques of the FEA such as Field Reconstruction Method.

The field reconstruction approach utilizes the field created by current in a single slot, along with field generated by the permanent magnet of the rotor over a single stator tooth pitch to construct the entire force profile for the electrical machine under arbitrary stator excitation and rotor position [136]. It must be pointed out that even though most of the objectives in this thesis have been achieved numerically, this approach has not been used.

A.5.3 Semi-Analytical Method

The numerical method has a very high prediction accuracy rate but it is time-consuming. A purely analytical method boasts of computational rapidity but its precision is limited due to the simplification of the machine's geometry. Therefore, the semi-analytical approach comes into being. The semi-analytical method combines the strengths of the analytical and the numerical methods to predict the vibration and noise of electrical machines.

As all the electromagnetic force, structural modes and vibroacoustic quantities can be calculated analytically or numerically, the semi-analytical methods are various. A commonly used approach is to calculate the radial magnetic forces through FEM, the vibration modes and acoustic radiation can be, then, obtained by the analytical model [137],[138]. However, due to the low precision of analytically calculated structural modes, this method has the same defects as the analytical method. On this premise, the analytical modal analysis can be superseded by a numerical solution to improve the accuracy of the semi-analytical model [38],[71],[97]. Furthermore, it is a common practice to reduce the computational effort by evaluating the electromagnetic forces analytically using the Maxwell stress tensor method given in [3]. Here the components of the magnetic flux density are extracted from the middle of the air gap using the numerical method.

A.5.4 Experimental Method

Since none of the models discussed above can capture all the design details as the actual system itself, an effective means of evaluating the acoustic noise emitted by the electrical machine must be sought. The experimental approach comes through as the best candidate for this task. The experimental method involves measurements on actual electrical machines. The procedure for taking acoustic measurements in an actual machine under actual operating condition can be quite challenging. The general procedure is discussed below and is applicable to any electrical machine and in any stage of its operating life.

First, acceleration transducers called accelerometers are stuck on the machine surface to measure the vibrations from the stator. The measurement is sensitive to the position and location of the accelerometer. Next, the noise test is carried out in an anechoic chamber. Briefly, an anechoic chamber is a hemispherical room in which free-field condition is simulated by lining the inside of the room with highly absorbent material so that the sound pressure is inversely proportional to the square of the distance from the sound source. Then, microphones are placed on the hemispherical surface at specified radius from the electric motor to record the mean sound pressure. For small electrical machines, the convenient measuring surface can be a hemispherical surface with a radius of 1 m or 0.5 m and all the measurement points should be spread evenly over the surface. For medium-sized and large machines, it can be a surface which is at certain key points 1 m away from the motor surface. Additionally, the ISO 1680 recommends acoustic noise measurements to be taken 1 m away from the motor surface. Fig A.6 portrays a electrical machine inside a hemispherical surface. The numbers on the surface indicate the locations of each microphone.

The sound pressure around an electrical machine vary not only with the distance from the machine but also with the shape and location of the measuring surface. Therefore, it is essential to quote the mean sound pressure level value together with the shape and location of the measuring surface. When we want to compare the noise emission capacity of two motors, we should compare the sound pressure level $\bar{\mathrm{L}}_{\mathrm{P}}$ values referred to a common measuring surface. In order to avoid the need to quote both the mean sound pressure level and the shape and location of the measuring surface, we can use the acoustic term *sound power level*. The sound power level P_{SL} is evaluated from $\bar{\mathrm{L}}_{\mathrm{P}}$ by the microphones using (A.10) and (A.11), where S is the area of the hemisphere surface whose radius is 1 m and $\mathrm{S}_0 = 1\ \mathrm{m}^2$ is the reference area, L_{Pi} is the sound pressure of microphone i, and n is the total number of measurement points. Fig. A.7 shows an experimental setup to measure the sound power of a permanent magnet synchronous motor. The motor is suspended from the ground at the center of the hemispherical surface and four Bruel & Kjaer Type 4187 microphones equidistant from each other have been used to measure the mean sound pressure level.

The sound power measured from the noise test is used as the benchmark to validate the efficacy of the analytical, numerical and semi-analytical models. But the noise from measurements are always higher than those estimated by the other models. The reason being that the experimental approach accounts for all the noise components emitted by the electrical machine, i.e., aerodynamic, electromagnetic and mechanical noises. It must be re-emphasized that the analytical, the numerical and the semi-analytical models are used to predict electromagnetic vibration and noise only. So, to validate the accuracy of the predicted results, it is necessary to filter out the aerodynamic and mechanical noises from the measured results. The aerodynamic noise can be eliminated by removing the fans during the noise test. For the air-cooled and water-cooled machines, the contribution of the aerodynamic noise can simply be ignored. Subsequently, the mechanical noise can be recognized based on the sudden power-off method. With the power supply removed, the electromagnetic noise is eliminated and the mechanical noise can be distinguished directly.

$$\mathrm{P}_{\mathrm{SL}} = \mathrm{L}_{\mathrm{P}} + 10\ \log_{10}\left(\frac{\mathrm{S}}{\mathrm{S}_0}\right) \tag{A.10}$$

$$\bar{\mathrm{L}}_{\mathrm{P}} = 10\ \log_{10}\left(\frac{1}{20}\sum_{i=1}^{n} 10^{(0.1)\mathrm{L}_{\mathrm{P}i}}\right) \tag{A.11}$$

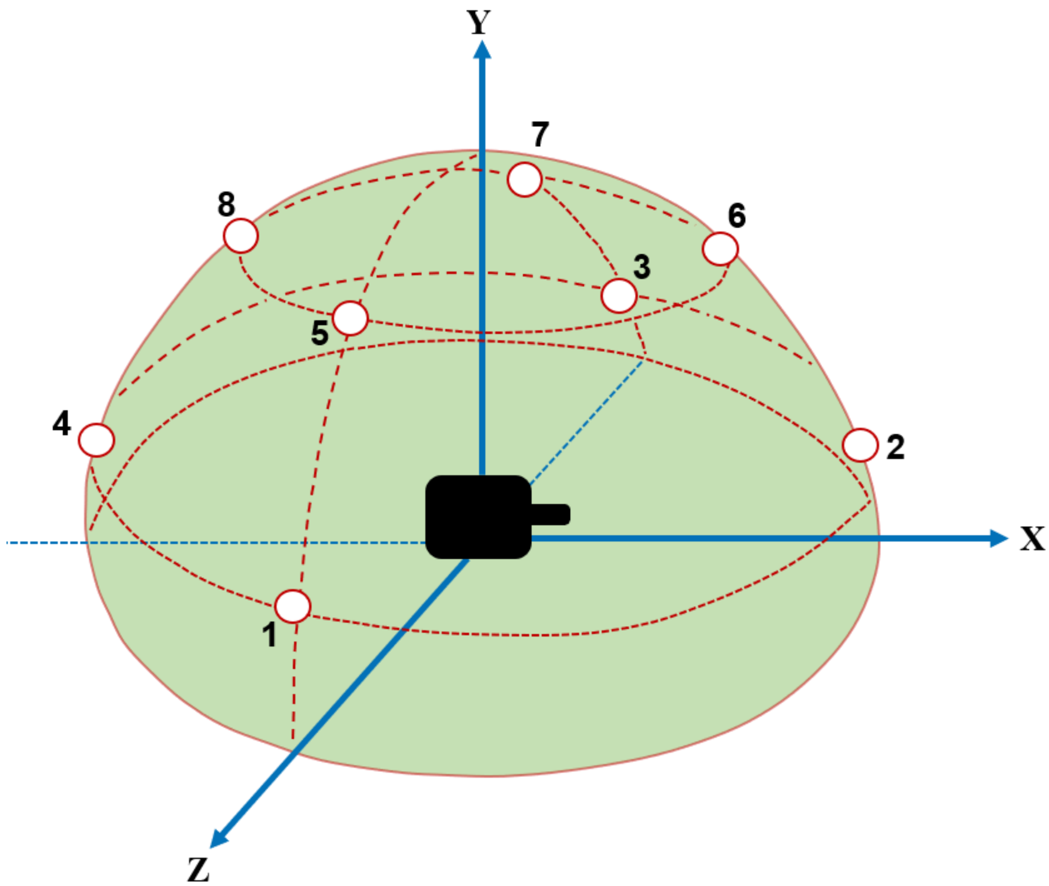

Fig. A.6 Example of the distribution of 8 measuring points over an imaginary hemispherical surface enclosing a motor. Radius of hemisphere is 1 m [2]

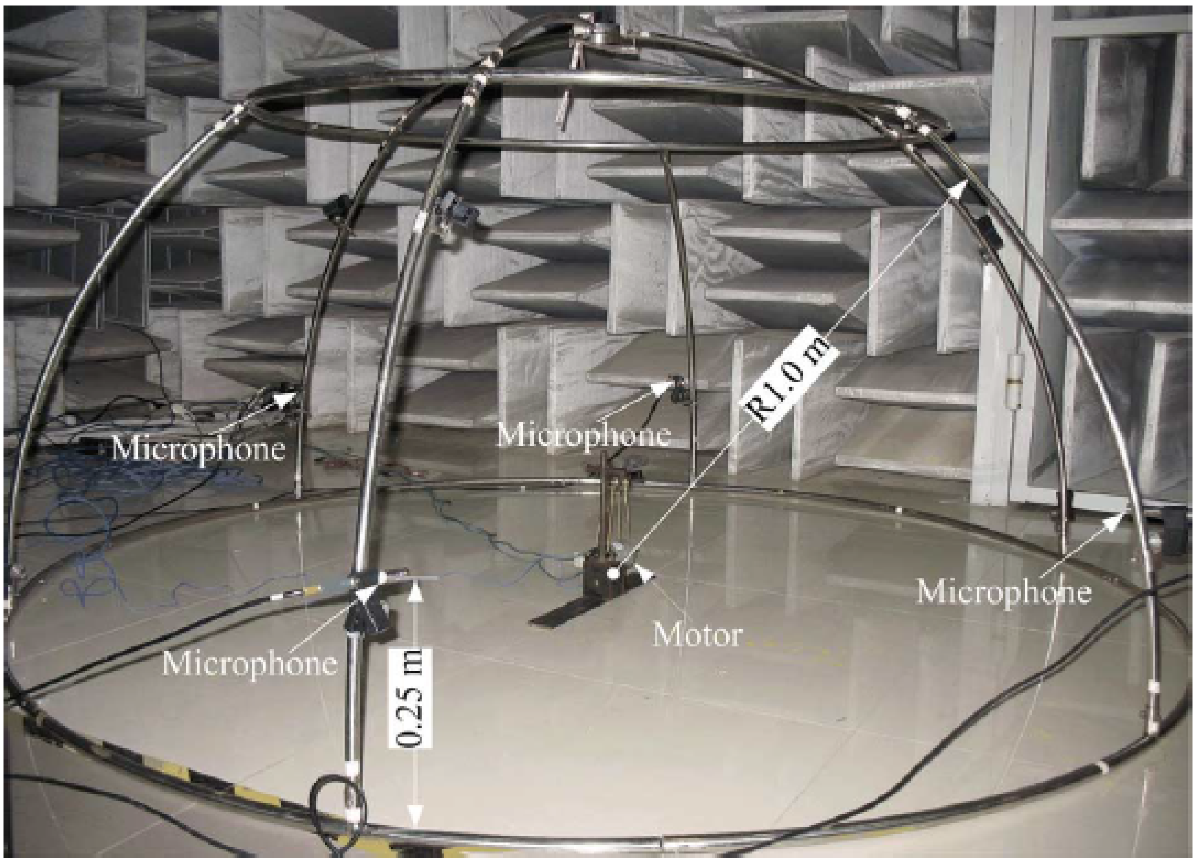

Fig. A.7 Experimental setup of the measurement of sound pressure of an electrical machine in a hemi-anechoic room at 4 microphone locations [7]

Appendix B

Electric Motor Operation & Control-Drive System

B.0.1 DQ Model of Synchronous AC Machines

Synchronous AC machines such as an interior permanent magnet can be represented using a dq model to simplify its control and analysis. In brief, multi-phase AC quantities such as the winding voltage and current are transformed into two DC values that are synchronous to the rotor speed, named as the "direct" and the "quadrature" axes [139]. Changing the number of poles or phases does not affect the underlying principle as the dq model accounts for it. A key assumption is that only the fundamental harmonic is considered. Note that the dq convention employed here follows that in [140] where the q-axis represents the high inductance path.

The stator current vector, $\mathbf{I}_{\mathrm{S}}$, is represented by (B.1) in Cartesian coordinates using the d and q-axis currents, $\mathbf{I}_{\mathrm{d}}$ and $\mathbf{I}_{\mathrm{q}}$. An alternative representation uses Polar coordinates, where I_{S} is the current magnitude and $\boldsymbol{\gamma}$ is the current advance angle. The reference point of γ is taken from the q-axis with a counterclockwise positive rotation. Since I_{S} is restricted by the inverter current or the machine's thermal limit, both $\mathbf{I}_{\mathrm{d}}$ and $\mathbf{I}_{\mathrm{q}}$ are constrained within the **current limit circle** in (B.2).

In a similar manner, the stator flux linkage vector, λ_{S}, is represented by (B.3) using its d and q-axis components, λ_{d} and λ_{q} and load angle, δ. The flux linkage is related to the stator current through the dq-axis inductances, $\mathbf{L}_{\mathrm{d}}$ and $\mathbf{L}_{\mathrm{q}}$, and the PM flux linkage, λ_{m}. Typically, the value of $\mathbf{L}_{\mathrm{q}}$ significantly decreases for higher I_{s} due to material saturation, while $\mathbf{L}_\mathrm{d}$ stays relatively constant (Fig. B.1).

$$\mathbf{I}_\mathrm{S} = \begin{bmatrix} \mathrm{I_d} \\ \mathrm{I_q} \end{bmatrix} = \begin{bmatrix} -\mathrm{I_s} \sin\gamma \\ +\mathrm{I_s} \cos\gamma \end{bmatrix} \tag{B.1}$$

$$\mathrm{I_S^2} = \mathrm{I_d^2} + \mathrm{I_q^2} \tag{B.2}$$

$$\boldsymbol{\lambda}_\mathrm{S} = \begin{bmatrix} \lambda_\mathrm{d} \\ \lambda_\mathrm{q} \end{bmatrix} = \begin{bmatrix} -\lambda_\mathrm{s} \sin\delta \\ +\lambda_\mathrm{s} \cos\delta \end{bmatrix} = \begin{bmatrix} \mathrm{L_d I_d} + \lambda_\mathrm{m} \\ \mathrm{L_q I_q} \end{bmatrix} \tag{B.3}$$

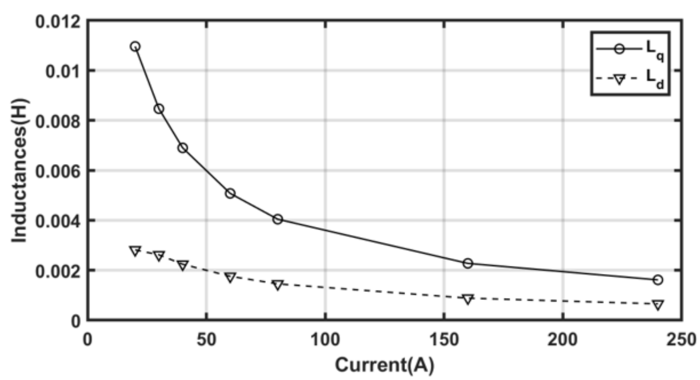

Fig. B.1 $\mathrm{L_q}$ and $\mathrm{L_d}$ vs Current

Based on the previous characteristics, two well-known measures are defined for synchronous AC machines. One of them is the saliency ratio, ξ, as shown in (B.4) which correlates with the amount of produced reluctance torque. The other measure is the characteristic current, $\mathrm{I_{ch}}$, in (B.5) which quantifies a motor's wide-speed range. Ideally, $\mathrm{I_{ch}}$ should be close to the rated current to guarantee infinite speed operation.

$$\xi = \frac{\mathrm{L_q}}{\mathrm{L_d}} \tag{B.4}$$

$$\mathrm{I_{ch}} = \frac{\lambda_\mathrm{m}}{\mathrm{L_d}} \tag{B.5}$$

Following the previous definitions, the stator phase voltage vector, $\mathrm{V_s}$, is defined in (B.6) using its dq components. In steady-state, this voltage vector is related to $\mathrm{I_S}$ and λ_S using the stator phase resistance, $\mathrm{R_s}$, and the electrical frequency, ω_e. For the sake of simplified explanation, the effect of winding resistance is ignored which can normally be accounted for by boosting the rated voltage by 10% to 20%. Given the limit of the battery voltage, the **voltage limit ellipse** in (B.7) is obtained as a function of the dq currents. The ellipse's eccentricity is controlled by ξ and is centered at -$\mathrm{I_{ch}}$ on the $\mathrm{I_d}$-axis. The radius is a function of the DC bus voltage which affects $\mathrm{V_s}$, $\mathrm{L_d}$, and the rotor speed. The higher the rotor speed, the smaller the ellipse's size which restricts the choice of optimal dq currents. This means that the motor would typically operate in the second quadrant of the dq current plane.

Based on the dq model representation, the electromagnetic torque, $\mathrm{T_{em}}$, can be written as in (B.8) and (B.9) for Cartesian and Polar coordinates respectively. The first component constitutes the PM torque, while the second one is the reluctance torque. To maximize $\mathrm{T_{em}}$, an optimal dq current must be set which will be discussed below.

$$\mathbf{V}_\mathrm{S} = \begin{bmatrix} \mathrm{V_d} \\ \mathrm{V_q} \end{bmatrix} = \mathrm{R_s I_S} + j\omega_\mathrm{e}\lambda_\mathrm{S} \tag{B.6}$$

$$\mathrm{V_S^2} = \mathrm{V_d^2} + \mathrm{V_q^2} \rightarrow \left(\frac{\mathrm{V_s}}{\omega_\mathrm{e}\mathrm{L_d}}\right)^2 = (\mathrm{I_d} + \mathrm{I_{ch}})^2 + \xi^2\mathrm{I_q^2} \tag{B.7}$$

$$\mathbf{T}_\mathrm{em} = \frac{3}{2}\mathrm{P_1}(\lambda_\mathrm{m}\mathrm{I_q} + (\mathrm{L_d} - \mathrm{L_q})\mathrm{I_d I_q}) \tag{B.8}$$

$$\mathbf{T}_\mathrm{em} = \frac{3}{2}\mathrm{P_1}(\lambda_\mathrm{m}\mathrm{I_s}\cos\gamma + (\mathrm{L_q} - \mathrm{L_d})\mathrm{I_s^2}\sin 2\gamma) \tag{B.9}$$

B.0.2 Operation Map of Electrical Machines

The first principle in the context of integrated motor drive systems is the torque-speed map used to demonstrate the essential variation of motor quantities, such as voltage, torque, flux and current, together in one plane with respect to the synchronous speed or frequency.

Fig. B.2 illustrates the generic operation map of an electric machine. Not all types of machines are capable of operating over the entire map. For example, synchronous reluctance machines do not possess a wide flux weakening (FW) operation since they are not assisted with permanent magnets to provide an almost zero d-axis flux linkage [140]. However, in new technologies, such as hybrid and electric vehicles, motors are designed such that, for example by adding permanent magnets, they are capable of operating over a wide torque-speed range. The maximum torque per ampere region (MTPA) is applicable to both the transient and steady-state operations below the base speed. The motor voltage, or rather equivalently and more technically the back-electromotive force, ideally increases linearly from zero to its rated value at the base speed. Along the linear voltage region, the rated magnetic flux is perfectly tuned. Otherwise, the torque falls below its maximum value. If the slope of the supply voltage is higher than rated, the magnetic flux, and consequently the magnetic losses, will increase. Also, a non-zero voltage bias must be added in order to compensate for the voltage drop across the phase winding resistance. This bias is normally around 10% to 20% of the rated voltage. The motor current is adjusted to its maximum value which is typically determined by the thermal constraints of the machine and the inverter. The motor torque and flux are also kept constant in the MTPA region.

On the other hand, the FW region includes operating points beyond the base speed up to the maximum constant power speed. The voltage and the current are ideally fixed at their rated values. The motor torque is degraded to guarantee a safe power level of the system. This task is handled by weakening the motor flux density in the airgap which reduces the back-EMF and permits the same current level in the windings. Beyond the base speed, there are two distinct modes, including the constant power speed range and maximum torque/volt (MTPV). In theory, the output power is constant and equal to the rated value in the constant power speed region. However, depending on the motor type, there can be deviation from rated conditions. The MTPV control is applicable to operating points located far from the base speed, beyond the maximum constant power speed. Not all types of machines can operate in the MTPV region which is a function of the motor current and the DC bus voltage. Moreover, the maximum available speed is a function of the DC bus voltage. A detailed discussion of the various control strategies used to operate electrical machines in the different regions of the torque-speed map and the SVPWM switching technique are presented in Appendix B.1 and Appendix B.2 respectively.

B.1 Motor Control Strategies

The mode diagram displayed in Fig. B.3 for an IPM motor will be used to explain the following control strategies: MTPA, FW, and MTPV.

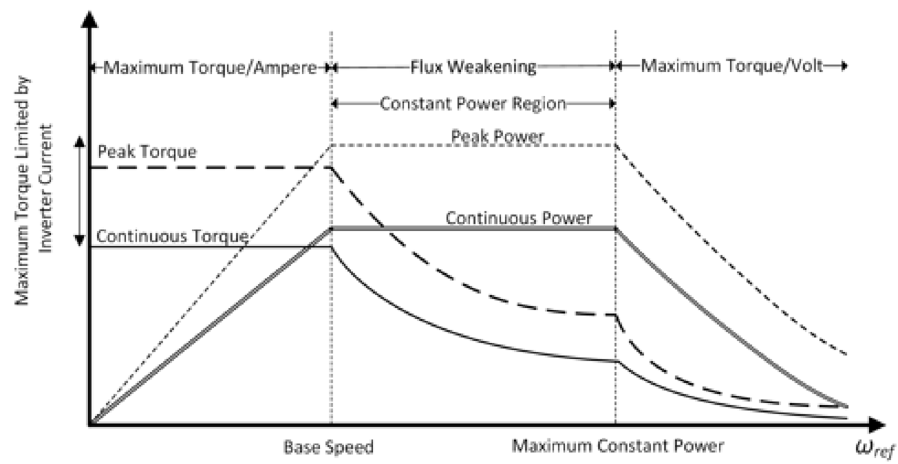

(a)

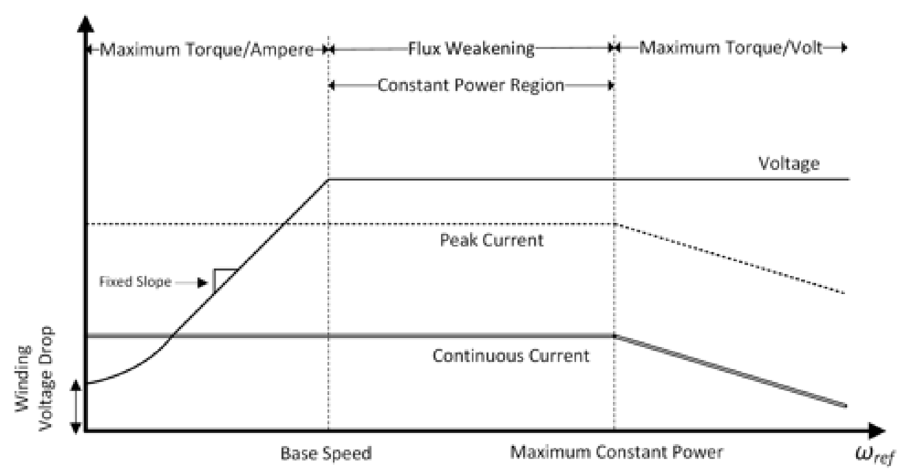

(b)

Fig. B.2 Operation map (a) torque vs speed (b) voltage vs speed [8].

B.1.1 Maximum Torque Per Ampere (MTPA)

When the electric motor is operating below base speed, ω_B, its back-EMF has not matched the terminal winding voltage. This means that the input voltage has not been constrained by (B.7). Referring to Fig. B.3, this condition occurs for the voltage ellipses of ω_1 and ω_B. All dq currents within the **current limit circle** in (B.2) are feasible. Hence, the MTPA control strategy defined in (B.10) for fixed I_S is applied to minimize the motor's copper

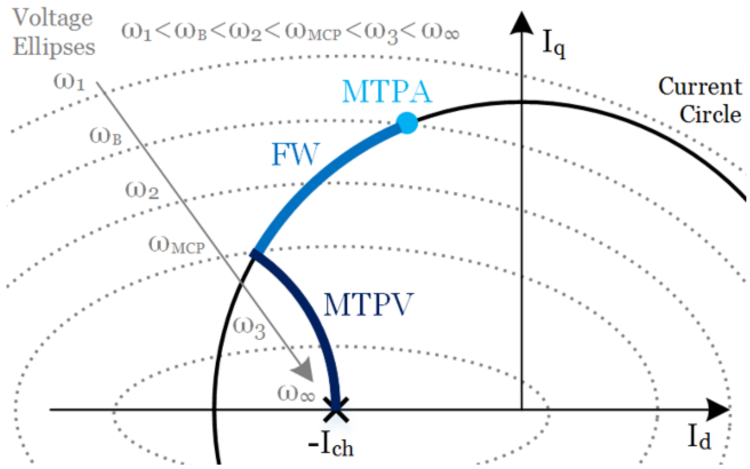

Fig. B.3 Mode diagram: trajectory of control strategies in current plane [9]

losses. For a given I_S, T_{em} is maximized to find an optimal γ. From zero to base speed, commonly known as the Constant Torque or MTPA region, the corresponding T_{em} values are computed at every speed using a fixed dq current as shown in Fig. B.3.

$$\frac{dT_{em}}{d\gamma} = 0 \tag{B.10}$$

B.1.2 Flux Weakening (FW)

Above base speed operation, the motor's back EMF has exceeded the maximum terminal winding voltage so the MTPA strategy cannot be employed anymore. In Fig. B.3, this case corresponds for the voltage ellipses of ω_B, ω_2 and ω_{MCP}. Thus, the FW strategy in (B.11) ensures that I_S is maintained while the voltage limit in (B.7) is satisfied. The machine's flux is weakened by reducing I_d or varying for different speeds. In practice, injecting large amounts of negative I_d increases the risk of demagnetization. From base to max speed, known as the Constant Power range, this FW equation is solved for every speed to find the trajectory of dq currents as shown in Fig. B.3.

$$\mathbf{I}_s \cap \mathbf{V}_s \tag{B.11}$$

B.1.3 Maximum Torque Per Volt (MTPV)

Beyond the maximum constant power speed, ω_{MCP}, the FW strategy can no longer produce a nonzero $\mathrm{T_{em}}$ and a constant power. For an infinite-speed machine, the center of the voltage limit ellipse is located at -$\mathrm{I_{ch}}$ inside the current limit circle which suggests that both $\mathrm{I_S}$ and γ must be varied. This corresponds for the voltage ellipses of ω_{MCP}, ω_3, and ω_∞ in Fig. B.3. Hence, the MTPV strategy in (B.12) maximizes $\mathrm{T_{em}}$ for a fixed DC bus voltage or λ_{S} to find optimal trajectory of dq currents. During MTPV operation, negative $\mathrm{I_d}$ values are much more significant than in FW control so particular attention must be placed to avoid irreversible PM demagnetization.

$$\frac{\mathrm{dT_{em}}}{\mathrm{d}\delta} = 0 \tag{B.12}$$

B.2 Space Vector Pulse-Width Modulation (SVPWM)

The reference dq0 currents obtained from the control strategies are converted to the dq0 voltages ($\mathrm{V_{dref}}$ and $\mathrm{V_{qref}}$) using another pair of PI controllers. These quantities are then used to generate the phase voltages through the PWM and inverter modules. In this section, the SVPWM technique is investigated due to its common use to drive two-level inverters (Fig. B.4). A balanced star-connected three-phase inverter with bi-directional switches is discussed. To this aim, the space vector transformation from ABC-to-$\alpha\beta$0-to-dq0 and reverse dq0-to-$\alpha\beta$0-to-ABC frames are explained, as shown in Fig. 3.5. For a balanced three-phase system, the sum of the phase voltages ($\mathrm{V_{An}}$,$\mathrm{V_{Bn}}$ and $\mathrm{V_{Cn}}$) should be equal to zero as in (B.13). Hence, three-phase quantities are represented by two-phase quantities called space vectors.

$$\mathrm{V_{Cn}} + \mathrm{V_{Bn}} + \mathrm{V_{Cn}} = 0 \tag{B.13}$$

The space vector transformation of the time-variant three-phase voltages is derived as follows:

$$\mathbf{V} = \mathrm{V}_\alpha + j\mathrm{V}_\beta = \frac{2}{3}(\mathrm{V_{An}}a^0 + \mathrm{V_{Bn}}a^1 + \mathrm{V_{Cn}}a^2) \text{ where } a = e^{j\frac{2\pi}{3}} \tag{B.14}$$

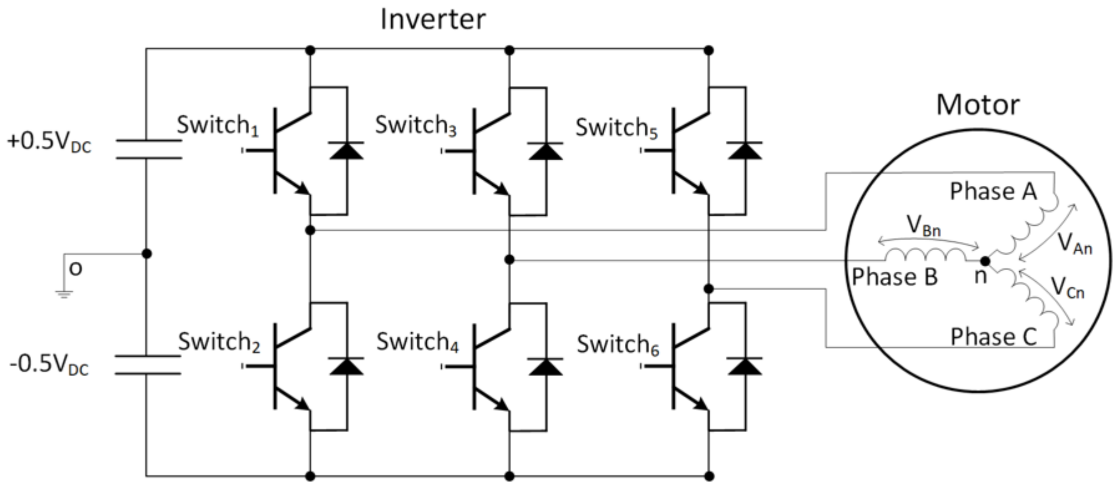

Fig. B.4 A two-level three-phase inverter [8]

$$\begin{bmatrix} V_\alpha \\ V_\beta \\ V_o \end{bmatrix} = \underbrace{\begin{bmatrix} \frac{2}{3} & -\frac{1}{3} & -\frac{1}{3} \\ 0 & \frac{1}{\sqrt{3}} & \frac{1}{\sqrt{3}} \\ \frac{1}{3} & \frac{1}{3} & \frac{1}{3} \end{bmatrix}}_{\text{Clark Transform}} \begin{bmatrix} V_{An} \\ V_{Bn} \\ V_{Cn} \end{bmatrix} \tag{B.15}$$

$$|\mathbf{V}| = \sqrt{V_\alpha^2 + V_\beta^2}, \quad \theta = \arctan\left(\frac{V_\beta}{V_\alpha}\right) = \omega_{st} = 2\pi f_{st} \tag{B.16}$$

$$\begin{bmatrix} V_d \\ V_q \end{bmatrix} = \begin{bmatrix} \cos(\theta) & \sin(\theta) \\ -\sin(\theta) & \cos(\theta) \end{bmatrix} \begin{bmatrix} V_\alpha \\ V_\beta \end{bmatrix} \tag{B.17}$$

Boldface signals are vectors. $|\mathbf{V}|\angle\theta$ is the space vector with the magnitude and angle of $|\mathbf{V}|$ and θ, respectively, and t is time. On the other hand, $|\mathbf{V}|\angle\theta$ must be produced by the possible combinations of the six inverter switches, which are limited to the switching states listed in Table B.1. All the eight states can be represented in the 0 frame by following the procedure explained in (B.14) to (B.17), and the corresponding vectors are shown in Fig. B.5 using V_1, V_2, V_3, V_4, V_5, and V_6. The V_0 and V_7 vectors have a magnitude of zero. Therefore, they are not shown in the figure. The magnitude of active vectors equal to kV_{DC}, where k is defined by the ABC-to-$\alpha\beta 0$ transformation convention [141].

According to Fig. B.5, there are six sectors which are shifted by 60 degrees in counter-clockwise direction. Now, consider a small interval of time (T_{sw}), at which the reference

Table B.1 SVPWM switching states (**S** stands for **switch**)

Vector	S_1	S_3	S_5	S_2	S_4	S_6	V_{AB}	V_{BC}	V_{CA}	
$V_0 = \{000\}$	OFF	OFF	OFF	ON	ON	ON	0	0	0	Zero
$V_1 = \{100\}$	ON	OFF	OFF	OFF	ON	ON	$+V_{dc}$	0	$-V_{dc}$	Active
$V_2 = \{110\}$	ON	ON	OFF	OFF	OFF	ON	0	$+V_{dc}$	$-V_{dc}$	Active
$V_3 = \{010\}$	OFF	ON	OFF	ON	OFF	ON	$-V_{dc}$	$+V_{dc}$	0	Active
$V_4 = \{011\}$	OFF	ON	ON	ON	OFF	OFF	$-V_{dc}$	0	$+V_{dc}$	Active
$V_5 = \{001\}$	OFF	OFF	ON	ON	ON	OFF	0	$-V_{dc}$	$+V_{dc}$	Active
$V_6 = \{101\}$	ON	OFF	ON	OFF	ON	OFF	$+V_{dc}$	$-V_{dc}$	0	Active
$V_7 = \{111\}$	ON	ON	ON	OFF	OFF	OFF	0	0	0	Zero

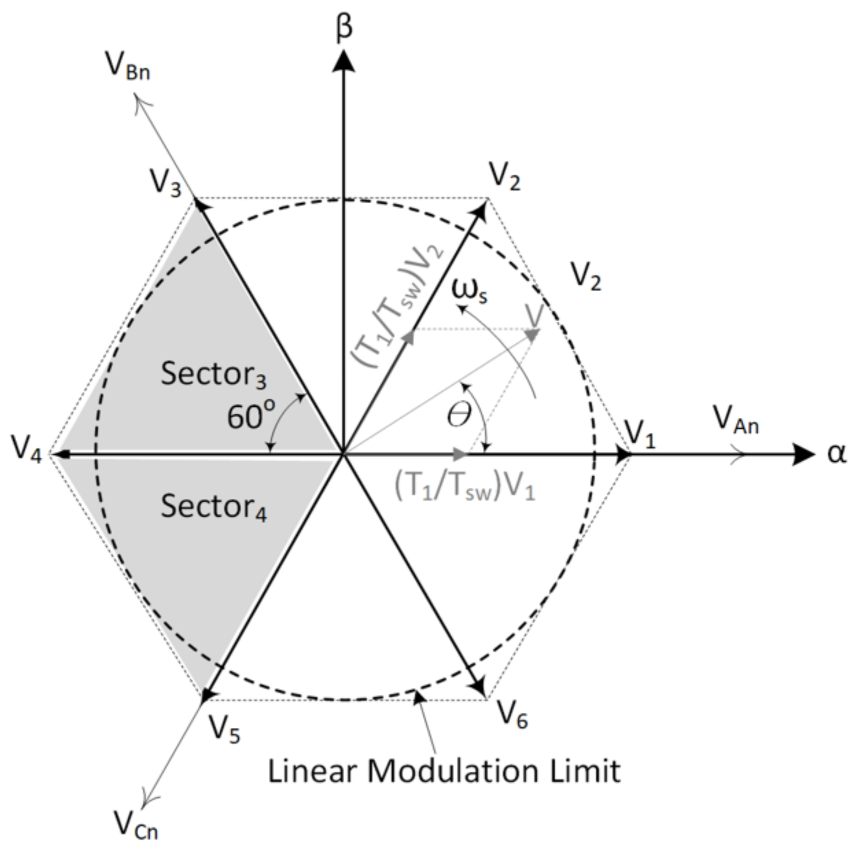

Fig. B.5 Vector representation for stator and inverter voltages [8].

vector, **V**, is located in the first sector, as shown in Fig. B.5. Can we produce the reference vector using the inverter switching states? The answer is yes, and the solution is the "average voltage vector over a sub-cycle" method. T_{sw} is the sub-cycle and is inferred as the switching cycle ($T_{sw}=\frac{1}{f_{sw}}$), where f_{sw} is the switching frequency of the IGBT module. The underlying idea of average voltage vectors is as follows:

- Apply the active vector $\mathbf{V}_1$ for an interval of T_1 over the sub-cycle T_{sw} (Fig. B.5).
- Apply the active vector $\mathbf{V}_2$ for an interval of T_2 over the sub-cycle T_{sw}.
- For the remaining time ($T_0 = T_{sw}$ - T_1 - T_2), apply one of the zero vectors ($\mathbf{V}_0$, $\mathbf{V}_7$).

The above explanation is formulated as (B.18) and (B.19). Then, the time intervals can be calculated using (B.20), (B.21) and (B.22).

$$\mathbf{VT}_{sw} = V_{\mathbf{1}}T_1 + V_{\mathbf{2}}T_2 + V_{\mathbf{0,7}}T_0 \tag{B.18}$$

$$\mathbf{T}_{sw} = T_1 + T_2 + T_0 \tag{B.19}$$

$$\mathbf{T}_1 = \frac{|V| \sin(60^\circ - \theta)}{kD_{DC} \sin(60^\circ)} T_{sw} \tag{B.20}$$

$$\mathbf{T}_1 = \frac{|V| \sin(\theta)}{kD_{DC} \sin(60^\circ)} T_{sw} \tag{B.21}$$

$$\mathbf{T}_0 = T_{sw} - T_1 - T_2 \tag{B.22}$$

The average vector of the sectors other than sector_1 are calculated in the same fashion, but with a phase shift corresponding to the sector number. Using SVPWM, the time period that every switch needs to be ON/OFF is determined, and the associated voltage is applied to the motor phase winding.

Appendix C

Thermal Losses, Insulation System & Sampling Techniques

C.1 Loss calculation

Motor performance is determined by a combination of electromagnetic and thermal design [70]. According to Hussain et al. [142], the magnetic properties of ferromagnetic cores, the resistance of conductors, and the electrical insulation of the windings are severely affected by high operating temperatures. For example, the magnetic behavior of the ferromagnetic core is a complex function of temperature, which means that the magnetic properties measured at room temperature cannot predict accurately the magnetic behavior of the ferromagnetic material at elevated temperatures. The resistivity of a conductor increases with temperature. In the case of copper, the relationship between resistivity and temperature is approximately linear over a wide range of temperatures. Therefore, the FEA-based electric machine design process must account for these temperature variations and their effects on the magnetic behavior of the material to optimize the performance of the machines. An improved thermal design can be used with an existing electromagnetic design to achieve this, while extending the motor's operational lifetime.

The rise in temperature of an electric machine is mainly due to the inherent power losses dissipated in the form of heat. In motoring operation, for example, electrical input, $\mathrm{P_{in}}$, in Watts, is fed by the polyphase stator winding excitation given in (C.1a), where $\mathrm{V_s}$ is the RMS line voltage, $\mathrm{I_s}$ is the RMS line current, and ϕ is the phase angle between $\mathrm{V_s}$ and

$\mathrm{I_s}$. However, not all the $\mathrm{P_{in}}$ is converted into useful power, $\mathrm{P_{out}}$, due to the inherent motor losses. As a result, $\mathrm{P_{out}}$ is always less than $\mathrm{P_{in}}$. Lower losses result in a smaller temperature rise across motor components, which means that less heat is produced and dissipated. A lower motor temperature also places less strain on the required cooling system. Fig. C.6 identifies the motor components and associated losses. The power flow or conservation is represented in (C.1b), where $\mathrm{P_{loss}}$ corresponds to the motor losses, $\mathrm{P_{Cu}}$ is the conductor or copper loss in the stator windings, $\mathrm{P_{Fe}}$ is the iron loss in the silicon steel material, $\mathrm{P_{mn}}$ is the PM eddy current loss and $\mathrm{P_{mech}}$ is the mechanical loss on the rotor shaft.

Iron loss, sourced from eddy current and hysteresis effect, is due to changing magnetic field in the magnetic core. When a motor core is rotated in a magnetic field, a voltage, or emf, is induced in the coils. This induced EMF causes circulating loops of currents to flow, referred to as eddy currents. The power loss caused by these currents is known as eddy current loss, $\mathrm{P_e}$. Hysteresis loss, $\mathrm{P_h}$, on the other hand, is a consequence of the energy required to change the direction of the domains in a ferromagnetic material. $\mathrm{P_e}$ and $\mathrm{P_h}$ are generally calculated by using a posteriori approach, that is, iron loss is estimated by post-processing. There are several empirical methods to calculate $\mathrm{P_h}$ and $\mathrm{P_e}$, but the most commonly used approach (Steinmetz method) is presented in (C.1f) and (C.1g). Here, $\mathrm{K_h}$ is a constant whose value depends on the ferromagnetic material and the volume of the core, $\mathrm{B_{max}}$ is the maximum flux density, n varies in the range 1.5 to 2.5, and f is the frequency of variation of the applied current. Additionally, $\mathrm{K_e}$ is also a proportionality constant whose value depends on the type of material and its lamination thickness, δ.

$$\mathrm{P_{in}} = \sqrt{3}\mathrm{V_s I_s}\cos\phi = \mathrm{P_{out}} + \mathrm{P_{loss}} \tag{C.1a}$$

$$\mathrm{P_{loss}} = \mathrm{P_{Cu}} + \mathrm{P_{Fe}} + \mathrm{P_{mn}} + \mathrm{P_{mech}} \tag{C.1b}$$

$$\mathrm{P_{Cu}} = 3\mathrm{I_s^2 R_s} \tag{C.1c}$$

$$\mathrm{R_s} = \rho\frac{l}{A} \tag{C.1d}$$

$$\rho = \rho_0\left[1 + \alpha(\mathrm{T} - \mathrm{T_0})\right] \tag{C.1e}$$

$$\mathrm{P_h} = K_\mathrm{h}\mathrm{B}_\mathrm{max}^n f \tag{C.1f}$$

$$\mathrm{P_e} = K_\mathrm{e}(\mathrm{B_{max}} f\delta)^2 \tag{C.1g}$$

In addition to the iron losses, there is another loss which is due to the electrical resistance of the conductors in the windings of an electromagnetic device. This is referred to as

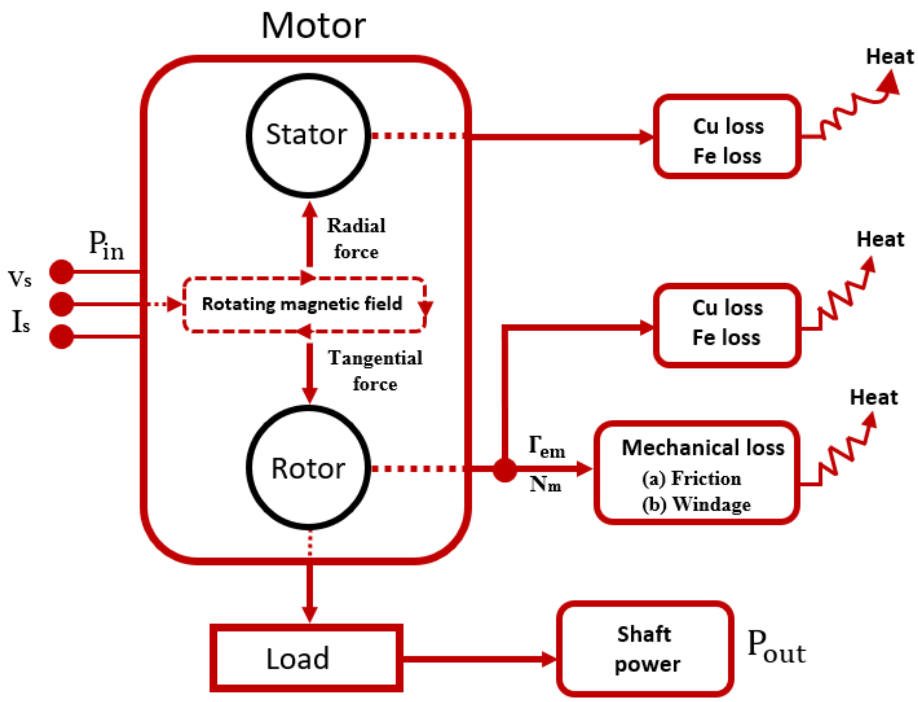

Fig. C.1 Power flow in an induction motor.

the copper loss, or Joule loss or Ohmic loss. The copper loss is calculated from (C.1c), where R_s is assumed to be the AC phase resistance for a Y-connected winding, ρ is the electrical resistivity, A is the conductor's cross-sectional area, l is the winding length, α is the temperature coefficient, and T is the winding temperature. The 0 subscript corresponds to the ambient temperature condition. For copper, α=0.00386 and $\rho = 1.733 \times 10^{-8}\ \Omega$ m at 20°C. A couple of observations can be made from (C.1c). First, P_{Cu} exhibits a quadratic growth when the excitation is increased. Second, P_{Cu} linearly relates to R_s which itself is a linear function of T. If the copper windings operate at a higher temperature, R_s and P_{Cu} increase linearly.

The mechanical loss comprises friction and windage loss due to the motion of the moving components. These losses are ignored in the electromagnetic design since P_{mech} loss component captures only the mechanical coupling. There is also the stray load loss which accounts for residual losses in the electric motor. While P_{Cu} and P_{Fe} are more straightforward to locate inside the machine, the last two losses are not so clear.

The stator winding is the major source of heat production in the electric motor. Therefore, to prevent overheating and motor breakdown, the coils must be properly insulated.

The insulation materials used to wrap the coils are classified in the order of A, B, F and H, with Class F being the most commonly used. These insulation classes were established to meet motor temperature requirements found in industrial applications. For example, the maximum operating temperature which a Class A insulation material can withstand without damage or degradation is 105°C. Hence, a Class A rated electric motor must not be operated beyond this value. Appendix C.2 provides a table of the insulation class for different materials and their permissible temperature range [NEMA, 2001] to help select the proper insulation to ensure long dependable insulation life.

C.2 Insulation Classification and Temperature

Understanding motor insulation class is essential. You must ensure that a motor being installed in a particular application has insulation designed to withstand the temperatures developed under full load and the effects of the ambient. Failure to do so may significantly reduce motor longevity. A well-accepted rule of thumb is that for every 10°C that the motor temperature exceeds its rated insulation temperature, the insulation life is reduced by half, likewise for every 10°C cooler, the insulation life is doubled.

NEMA specifies letter designations for motor insulation temperature ratings. There are four insulation temperature ratings denoted as Class A=105°C, Class B=130°C, Class F=155°C and Class H=180°C. Class A is an older form of insulation utilizing organic varnishes and resins available many years ago. Today, it would only be seen in very old motors and would not be used for new or re-manufactured motors. Class B is the most common insulation class used in most 60 Hz US motors. Class F is the most common for international and 50 Hz motors. In general, a motor should not operate above its insulation temperature rating. It is important to be aware that insulation classes are directly related to motor life. For example, a motor operating at 180°C will have an estimated life of:

- 300 hours with Class A insulation
- 1800 hours with Class B insulation
- 8500 hours with Class F insulation
- above 10k hours with Class H insulation

The motor's ambient temperature, internal temperature rise, the altitude and the service factor (S.F) are the determining factors in choosing the class of insulation. The ambient temperature is determined by measuring the ambient air surrounding the motor. The higher the temperature rise permitted, the higher the insulation class. The higher the insulation class, the greater temperature the insulation can withstand without degradation. Further, NEMA specifies allowable temperature rises for motors at full load (and at service factor, if applicable). These allowable temperature rises are based upon a reference ambient temperature of 40°C. Figure C.2 presents NEMA's allowable temperature rises at full load for 1.0 S.F and 1.15 S.F motors respectively.

Adding the NEMA allowable temperature rise of 105°C (for a Class F insulated, 1.0 S.F. motor), to the reference ambient temperature of 40°C, results in a total operating temperature for the motor of (105+40)=145°C. The 10°C temperature differential between the Class F insulation maximum temperature rating (155°C) and the allowable maximum temperature (145°C) provides an allowance for the hotspot temperature of the interior of the winding, which is difficult to measure directly.

NEMA Motor Insulation Temperature Ratings		**1.0 Service Factor Motors**			**1.15 Service Factor Motors**
Class	Temp. [°C]	Ambient [°C]	Hotspot [°C]	Temp. rise, ΔT	Temp. rise, ΔT
A	105	+ 40	+ 40	60	70
B	130	+ 40	+ 10	80	90
F	155	+ 40	+ 10	105	115
H	180	+ 40	+ 15	125	undefined

Fig. C.2 Electrical insulation system rating by NEMA [3]

Note: Do not confuse the NEMA insulation classes with the NEMA motor design codes which are also given by letters.

C.3 Sampling Plans

A sampling plan, also called design of experiment, is a strategy for allocating samples in the design space that aims at maximizing the amount of information acquired. The proper choice of a sampling plan usually involves an assessment of the intended utilization of the results, prior knowledge one has about problem to be analyzed (such as presence of noise and function structure) and other additional restrictions related to the availability of samples and time.

In a surrogate-based optimization framework, sampling plans are basically used for (i) screening of variables and (ii) to generate the points which will be the basis for the surrogate model. Assuming that the problem is already parametrized, the goal of screening is to measure the contribution of an independent variable to the response value. It is intuitively clear that the higher the number variables the higher the number of samples must be in order to build an accurate predictor. For the reason, in some cases, it is interesting to spend some of the computational budget in screening so as to minimize the number of variables. Some of the sampling plans often used for screening include, full factorial designs, fractional factorial designs, Plackett-Burman designs and central composite designs.

As we will see, these methods tend to spread the sample points around the boundaries of the design space and leave a few in the center. Although this features can be interesting if the region of interest is small or in preliminary experiments for screening of variables (in which there is a very limited computational budget), this is not the case when the purpose is to build a global model of an unknown landscape [Jin et al., 2001]. Specially when working with deterministic computer experiments, there seems to be a consensus among researchers that the sampling plan should be space-filling [Wang and Shan, 2007]. Space-filling sampling plans include Latin Hypercubes, Hammersley Sequences and Uniform Designs, etc. In the following sections a brief description of the aforementioned sampling plans/designs is presented with the aim of showing some of their main strengths and weaknesses. The intention of this section is to provide some insight on how to choose a suitable plan for a given problem.

C.3.1 Latin Hypercube Sampling

Latin hypercube is the most utilized sampling plan for deterministic computer experiments. In its most simple implementation, a Latin Hypercube [Park, 1994] can be built by splitting the design space into equal sized hypercubes and placing the available samples in them. Care is taken to guarantee that from each occupied hypercube we can leave the design space along any direction parallel to any of the coordinate axis without encountering any other occupied hypercube. Fig. C.5 illustrates this sampling plan.

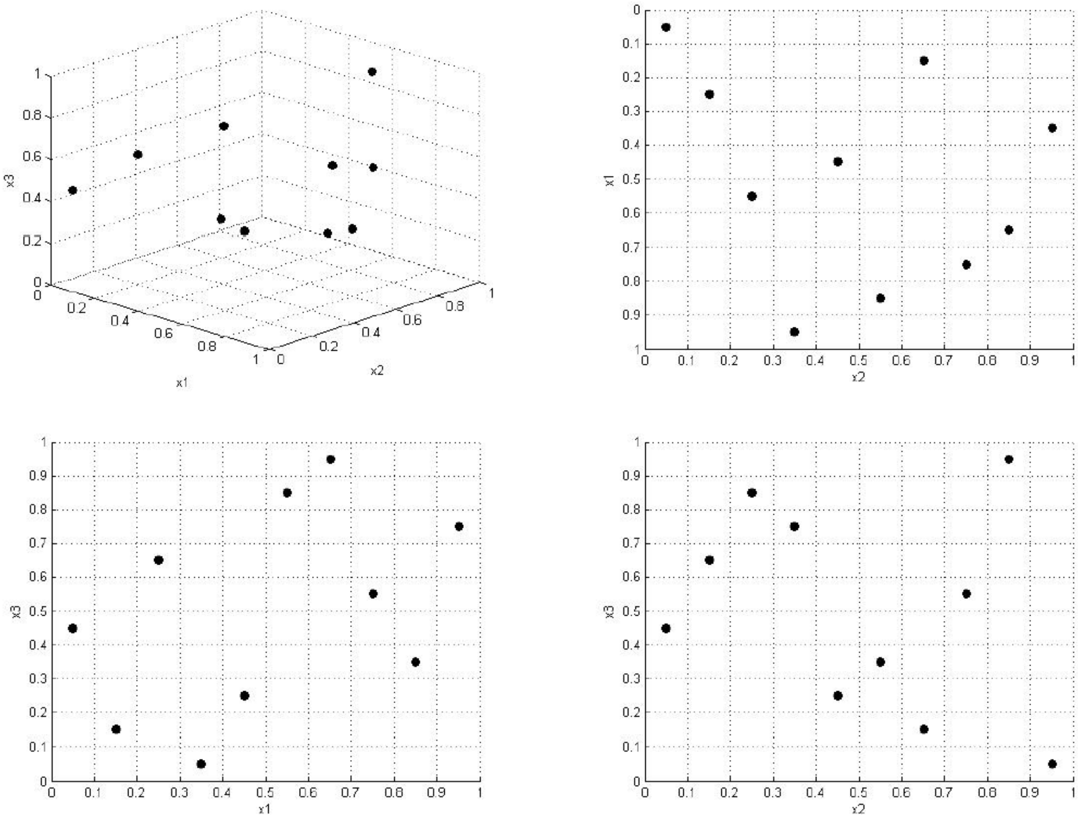

Fig. C.3 Three-variable, ten-point Latin Hypercube sampling plan, along with its two-dimensional projections [10].

As we can see, the projections on the axes are uniformly spread (multidimensional stratification), what is important when gathering information about an unknown function landscape. Besides if any of the variables is removed the features of a Latin hypercube maintained. Thus, if the designer, after gaining more knowledge about the problem, decides to remove some variables from it there is no need to perform another sampling. Although the presented recipe has some good features it does not guarantee that the plan will be space filling.

To avoid situations like that, some measure of uniformity is needed in order to evaluate

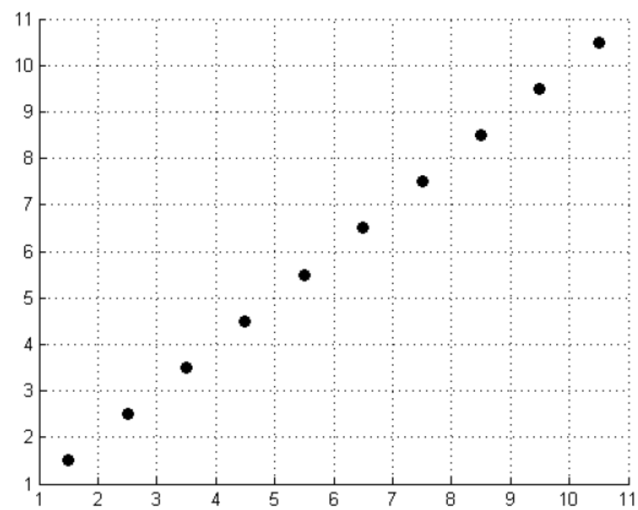

Fig. C.4 A non-space filling Latin Hypercube [10].

a Latin hypercube. The most widely-used metric to evaluate the "space-fillingness" of a sampling plan is probably the maximin metric introduced by [Johnson et al., 1990] defined as follows: Let $D = \{d_1, d_2, ... d_{\mathrm{m}}\}$ be the list of unique values of distances (usually Euclidian) between all possible pairs of points in a sampling plan $\mathbf{X}$, sorted in ascending order. Further, let $J = \{j_1, j_2, ..., j_{\mathrm{m}}\}$ be defined such that j_k is the number of pairs in $\mathbf{X}$ separated by the distance d_{k}.

Definition 1 $\mathbf{X}$ is a maximin plan among all available plans, if it maximizes d_1 and minimizes j_1.

Besides the pairwise distance, the pairwise correlations and even a combination of correlation and distance [Joseph and Hung, 2008] can be used as metrics for "space-fillingness". Nevertheless, in a surrogate-based optimization framework, normally, the set of sampling points is augmented during the optimization process and for these reason an initial space-feeling property is not a critical concern. In this context, not much time should be spent on trying to find the optimal Latin hypercube. Figure 6 illustrates the utilization of def.1 in the generation of Latin hypercubes.

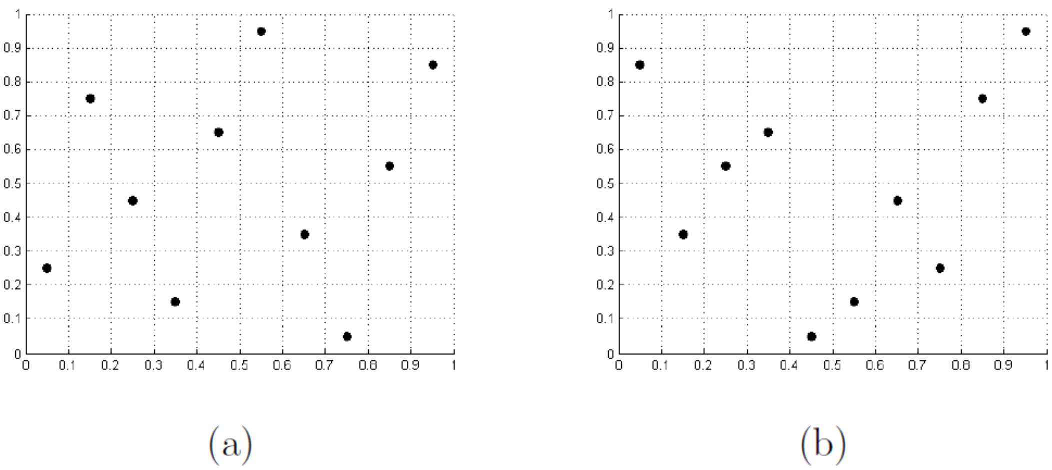

Fig. C.5 Two-variable, ten-point Latin Hypercube sampling plan improved by maximin criterion (a) and random (b) [10].

C.4 4Pole 12Slot IPM Motor: Sound Power Levels

The following histograms represent the sound power level distribution of all the 5000 motors used to build the design space of the 4Pole 12Slot interior permanent magnet synchronous motor. Four (4) operating speeds, i.e., 1000 RPM, 2000 RPM, 3000 RPM and 4000 RPM, have been investigated for the different motor designs. It is demonstrated that regardless of the operating speed, sound power levels increase as the temperature of the electric motor rises. This has been observed in all the samples.

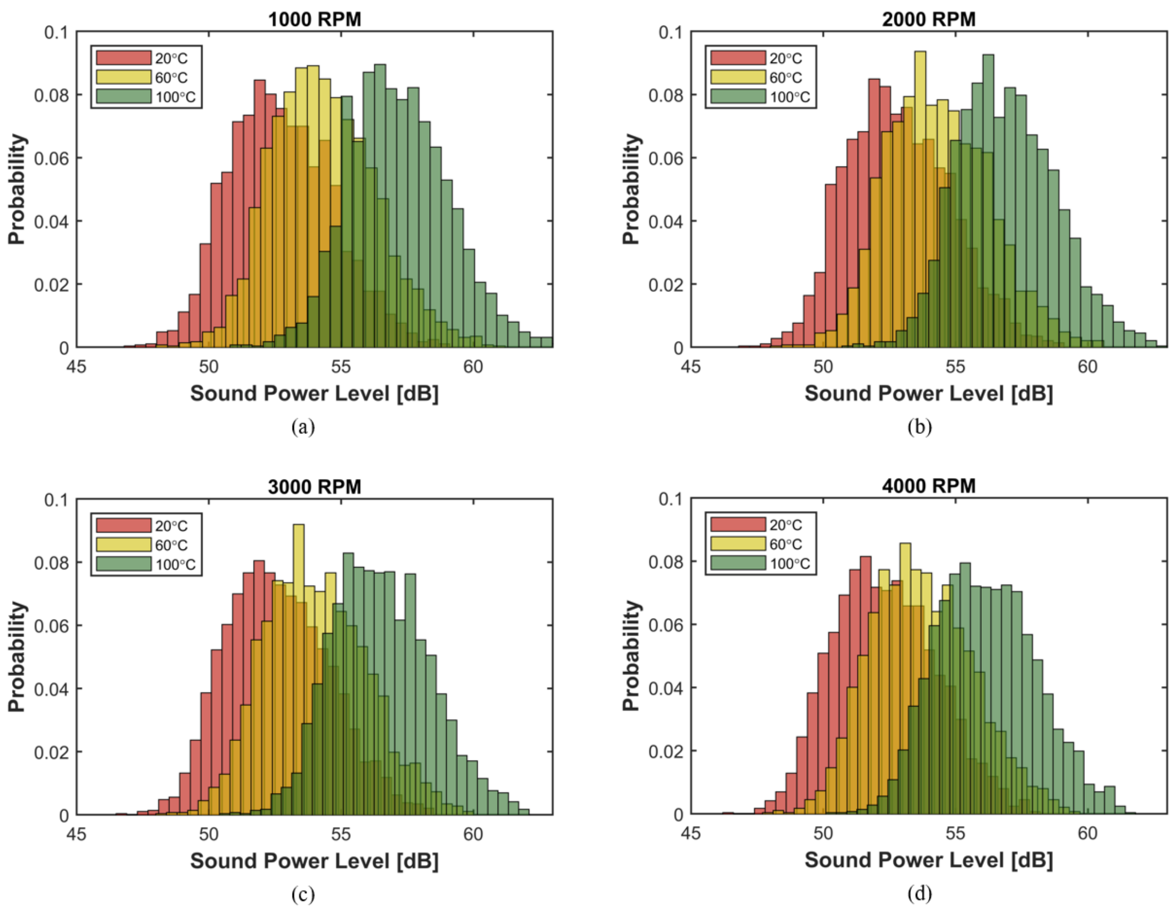

Fig. C.6 Statistical distribution of sound power at different speeds for 5000 samples in the acoustic design space of a 4Pole 12Slot IPM Motor (a) P_{SL} at 1000 RPM (b) P_{SL} at 2000 RPM (c) P_{SL} at 3 kRPM (d) P_{SL} at 4 kRPM.

References

[1] K. Johnson, *Acoustic and auditory phonetics*. John Wiley & Sons Inc., 2011.

[2] S. Yang, *Low-noise electrical motors*. Oxford University Press, USA, 1981.

[3] J. F. Gieras, C. Wang, and J. C. Lai, *Noise of polyphase electric motors*. CRC press, 2005.

[4] https://www.onlinebiologynotes.com/human-ear-structure-anatomy/.

[5] https://jameselectric.ca/help/motors-exploded view/.

[6] Mentor Graphics Corporation, "Motorsolve, and MAGNET," 2018.

[7] G. He, Z. Huang, R. Qin, and D. Chen, "Numerical prediction of electromagnetic vibration and noise of permanent-magnet direct current commutator motors with rotor eccentricities and glue effects," *IEEE Transactions on Magnetics*, vol. 48, no. 5, pp. 1924–1931, 2011.

[8] V. Ghorbanian, *An HPC-based Data-driven Approach to System-level Design Process for Integrated Motor-Drive Systems*. PhD dissertation, McGill University, Montreal, QC, Canada, 2018.

[9] M. H. Mohammadi, *A data-driven design process including multiphysics for synchronous AC machines using high-performance computing*. PhD thesis, Department of Electrical & Computer Engineering, McGill University, Montreal, QC, Canada, 2019.

[10] R. C. P. Silva, *Surrogate problem evaluation and selection for optimization with expensive function evaluations*. PhD dissertation, McGill University, Montreal, QC, Canada, 2018.

[11] P. R. Jones, "What's the quietest sound a human can hear?(aka "why omega-3 fatty acids might not cure dyslexia")," 2014.

[12] I. L. Ver and L. L. Beranek, *Noise and Vibration Control Engineering-Principles and Applications*, vol. 1. Bukupedia, 2006.

[13] J. S. Durch, L. M. Joellenbeck, L. E. Humes, *et al.*, *Noise and military service: Implications for hearing loss and tinnitus.* National Academies Press, 2006.

[14] N. Oishi and J. Schacht, "Emerging treatments for noise-induced hearing loss," *Expert opinion on emerging drugs*, vol. 16, no. 2, pp. 235–245, 2011.

[15] International Organization for Standardization, "ISO/R1680-1970, Test Code for the measurement of the airborne noise emitted by rotating electrical machinery," *ISO Standards Handbook 4, Acoustics, Vibrations and Shock*, no. 1, pp. 150–166, 1985.

[16] Electroacoustics—Sound Level Meters, IEC Std. 61 672, 2013.

[17] M. Dabrowski, "Construction of electrical machines," *Warsaw: WNT*, 1977.

[18] Z. Zhu and Y. Chen, "On the calculation of acoustic power radiated by an electrical machine," in *IEE Conference Publication on Electrical Machines and Drives*, no. 282, pp. 118–121, 1987.

[19] P. L. Timar, A. Fazekas, J. Kiss, A. Miklos, and S. Vang, "Noise and vibration of electrical machines," *Studies in electrical and electronic engineering*, vol. 34, 1989.

[20] S. Verma and A. Balan, "Determination of radial-forces in relation to noise and vibration problems of squirrel-cage induction motors," *IEEE Transactions on Energy Conversion*, vol. 9, no. 2, pp. 404–412, 1994.

[21] H. Jordan, "Electric motor silencer-formation and elimination of the noises in the electric motors," *W. Giradet-Essen editor*, vol. 14, p. 50, 1950.

[22] H. Jordan, "Approximate calculation of the noise produced by squirrel cage motors," *Engineers: Digest*, vol. 10, p. 222, 1949.

[23] J. Le Besnerais, V. Lanfranchi, M. Hecquet, P. Brochet, and G. Friedrich, "Prediction of audible magnetic noise radiated by adjustable-speed drive induction machines," *IEEE Transactions on Industry Applications*, vol. 46, no. 4, pp. 1367–1373, 2010.

[24] R. Islam and I. Husain, "Analytical model for predicting noise and vibration in permanent magnet synchronous motors," in *IEEE Energy Conversion Congress and Exposition*, pp. 3461–3468, 2009.

[25] D. Torregrossa, F. Peyraut, B. Fahimi, J. M'Boua, and A. Miraoui, "Multiphysics finite-element modeling for vibration and acoustic analysis of permanent magnet synchronous machine," *IEEE Transactions on Energy Conversion*, vol. 26, no. 2, pp. 490–500, 2010.

[26] V. Lanfranchi, A. Aït-Hammouda, G. Friedrich, M. Hecquet, and A. Randria, "Vibratory and acoustic behavior of induction traction motors, machine design improvement," in *Conference Record of the 2006 IEEE Industry Applications Conference Forty-First IAS Annual Meeting*, vol. 2, pp. 843–848, 2006.

[27] C. Martis, D. Fodorean, P. C. Irimia, and C. I. Husar, "Vibroacoustic behaviour analysis of a permanent magnet synchronous machine for automotive applications," in *49th International Universities Power Engineering Conference*, pp. 1–6, 2014.

[28] F. L. Dos Santos, J. Anthonis, F. Naclerio, J. J. Gyselinck, H. Van der Auweraer, and L. C. Góes, "Multiphysics nvh modeling: Simulation of a switched reluctance motor for an electric vehicle," *IEEE Transactions on Industrial Electronics*, vol. 61, no. 1, pp. 469–476, 2013.

[29] M. Furlan, A. Cernigoj, and M. Boltezar, "A coupled electromagnetic-mechanical-acoustic model of a dc electric motor," *COMPEL-The international journal for computation and mathematics in electrical and electronic engineering*, vol. 22, no. 4, pp. 1155–1165, 2003.

[30] C. Wang, J. Lai, and A. Astfalck, "Sound power radiated from an inverter driven induction motor ii: Numerical analysis," *IEEE Proceedings-electric power applications*, vol. 151, no. 3, pp. 341–348, 2004.

[31] C. Wang and J. Lai, "Vibration analysis of an induction motor," *Journal of sound and vibration*, vol. 224, no. 4, pp. 733–756, 1999.

[32] J. Daesuk, D.-K. Hong, and B.-C. Woo, "Numerical analysis of sound pressure level from permanent-magnet machine by electromagnetic vibration," in *2013 International Conference on Electrical Machines and Systems*, pp. 1425–1430, 2013.

[33] S. Park, S. Kim, W. Kim, J. Cho, and S. T. Lim, "A numerical model for predicting vibration and acoustic noise of ipmsm," in *2012 IEEE Vehicle Power and Propulsion Conference*, pp. 1054–1058, 2012.

[34] J. Le Besnerais, A. Fasquelle, M. Hecquet, J. Pelle, V. Lanfranchi, S. Harmand, P. Brochet, and A. Randria, "Multiphysics modeling: Electro-vibro-acoustics and heat transfer of pwm-fed induction machines," *IEEE Transactions on Industrial Electronics*, vol. 57, no. 4, pp. 1279–1287, 2009.

[35] I.-S. Jang, S.-H. Ham, W.-H. Kim, C.-S. Jin, S.-Y. Cho, K.-D. Lee, J.-J. Lee, D. Kang, and J. Lee, "Method for analyzing vibrations due to electromagnetic force in electric motors," *IEEE Transactions on Magnetics*, vol. 50, no. 2, pp. 297–300, 2014.

[36] M. Al Nahlaoui, D. Braunisch, B. Eichinger, S. Kulig, B. Ponick, and U. Werner, "Calculation methods for electromagnetically excited noise in induction motors," in *1st International Electric Drives Production Conference*, pp. 124–131, 2011.

[37] D. Torregrossa, F. Peyraut, C. Espanet, A. Cassat, and A. Miraoui, "New estimation of electromagnetic sound power radiated by a pm machine: An active and passive control guideline," in *IEEE Industry Applications Society Annual Meeting*, pp. 1–4, 2009.

[38] D. Braunisch, B. Ponick, and G. Bramerdorfer, "Combined analytical–numerical noise calculation of electrical machines considering nonsinusoidal mode shapes," *IEEE Transactions on Magnetics*, vol. 49, no. 4, pp. 1407–1415, 2012.

[39] M. Anwar and O. Husain, "Radial force calculation and acoustic noise prediction in switched reluctance machines," *IEEE Transactions on Industry Applications*, vol. 36, no. 6, pp. 1589–1597, 2000.

[40] A. Saito, H. Suzuki, M. Kuroishi, and H. Nakai, "Efficient forced vibration reanalysis method for rotating electric machines," *Journal of Sound and Vibration*, vol. 334, pp. 388–403, 2015.

[41] H.-J. Shin, J.-Y. Choi, Y.-S. Park, M.-M. Koo, S.-M. Jang, and H. Han, "Electromagnetic vibration analysis and measurements of double-sided axial-flux permanent magnet generator with slotless stator," *IEEE Transactions on Magnetics*, vol. 50, no. 11, pp. 1–4, 2014.

[42] S. Park, W. Kim, and S.-I. Kim, "A numerical prediction model for vibration and noise of axial flux motors," *IEEE Transactions on Industrial Electronics*, vol. 61, no. 10, pp. 5757–5762, 2014.

[43] M. Valavi, J. Le Besnerais, and A. Nysveen, "An investigation of zeroth-order radial magnetic forces in low-speed surface-mounted permanent magnet machines," *IEEE Transactions on Magnetics*, vol. 52, no. 8, pp. 1–6, 2016.

[44] B. Cassoret, J. Lecointe, and J. Brudny, "Power electronics and motor drives," *Boca Raton, FL, USA: CRC*, 2011.

[45] T. E. McDevitt, R. L. Campbell, and D. M. Jenkins, "An investigation of induction motor zeroth-order magnetic stresses, vibration, and sound radiation," *IEEE Transactions on Magnetics*, vol. 40, no. 2, pp. 774–777, 2004.

[46] S. Garvey and G. Le Flem, "Tangential forces matter," *9th International Conference on Electrical Machines and Drives*, no. 468, pp. 174–178.

[47] W. Wang, Q. Li, Z. Song, S. Yu, J. Chen, and R. Tang, "Three-dimensional field calculation and analysis of electromagnetic vibration and noise for disk permanent magnet synchronous machines," in *2008 International Conference on Electrical Machines and Systems*, pp. 631–634, 2008.

[48] Q. Li and Y. Wang, "The analysis of finite element for the noise of axial flux surface mounted permanent magnet synchronous machine's system," in *2010 International Conference on E-Product E-Service and E-Entertainment*, pp. 1–4, 2010.

[49] S. Zhihuan, T. Renyuan, Y. Shenbo, and Z. Hongyang, "The influence of vibration and acoustic noise of axial flux permanent magnet machines by inverter," in *2010 International Conference on Mechanic Automation and Control Engineering*, pp. 2423–2426, 2010.

[50] H. Ennassiri, M. Dhifli, F. Chabour, G. Barakat, Y. Amara, and F. Zidat, "Magneto-vibro-acoustic analysis of a discoidal switching flux permanent magnet machine dedicated to wind turbine application," in *2016 Eleventh International Conference on Ecological Vehicles and Renewable Energies (EVER)*, pp. 1–6, 2016.

[51] M. Dhifli, H. Ennassiri, and G. Barakat, "Study of the mechanical behaviour of a disc type flux switching machine for wind application," in *2016 IEEE 16th International Conference on Environment and Electrical Engineering (EEEIC)*, pp. 1–6, 2016.

[52] X. Liang, G. Li, J. Ojeda, M. Gabsi, and Z. Ren, "Comparative study of classical and mutually coupled switched reluctance motors using multiphysics finite-element modeling," *IEEE Transactions on Industrial Electronics*, vol. 61, no. 9, pp. 5066–5074, 2013.

[53] J. Li, X. Song, and Y. Cho, "Comparison of 12/8 and 6/4 switched reluctance motor: Noise and vibration aspects," *IEEE Transactions on Magnetics*, vol. 44, no. 11, pp. 4131–4134, 2008.

[54] G. Dajaku and D. Gerling, "The influence of permeance effect on the magnetic radial forces of permanent magnet synchronous machines," *IEEE Transactions on Magnetics*, vol. 49, no. 6, pp. 2953–2966, 2013.

[55] G. Dajaku and D. Gerling, "Magnetic radial force density of the pm machine with 12-teeth/10-poles winding topology," in *2009 IEEE International Electric Machines and Drives Conference*, pp. 1715–1720, 2009.

[56] H. Mai, R. Bernard, P. Bigot, F. Dubas, D. Chamagne, and C. Espanet, "Consideration of radial magnetic forces in brushless dc motors," in *2010 International Conference on Electrical Machines and Systems*, pp. 1–6, 2010.

[57] J. Wang, Z. P. Xia, D. Howe, and S. A. Long, “Vibration characteristics of modular permanent magnet brushless ac machines,” in *Conference Record of the 2006 IEEE Industry Applications Conference Forty-First IAS Annual Meeting*, vol. 3, pp. 1501–1506, 2006.

[58] J. Wang, Z. Xia, S. Long, and D. Howe, “Radial force density and vibration characteristics of modular permanent magnet brushless ac machine,” *IEE Proceedings-Electric Power Applications*, vol. 153, no. 6, pp. 793–801, 2006.

[59] J. Wang, Z. Xia, D. Howe, and S. Long, “Comparative study of 3-phase permanent magnet brushless machines with concentrated, distributed and modular windings,” *3rd IET International Conference on Power Electronics, Machines and Drives*, 2006.

[60] Y. Chen, Z. Zhu, and D. Howe, “Vibration of pm brushless machines having a fractional number of slots per pole,” *IEEE Transactions on Magnetics*, vol. 42, no. 10, pp. 3395–3397, 2006.

[61] D. Fodorean, M. M. Sarrazin, C. S. Marţiş, J. Anthonis, and H. Van der Auweraer, “Electromagnetic and structural analysis for a surface-mounted pmsm used for light-ev,” *IEEE Transactions on Industry Applications*, vol. 52, no. 4, pp. 2892–2899, 2016.

[62] H. Yang and Y. Chen, “Influence of radial force harmonics with low mode number on electromagnetic vibration of pmsm,” *IEEE Transactions on Energy Conversion*, vol. 29, no. 1, pp. 38–45, 2013.

[63] S. M. Castano, B. Bilgin, E. Fairall, and A. Emadi, “Acoustic noise analysis of a high-speed high-power switched reluctance machine: Frame effects,” *IEEE Transactions on Energy Conversion*, vol. 31, no. 1, pp. 69–77, 2015.

[64] W. Lo, C. C. Chan, Z.-Q. Zhu, L. Xu, D. Howe, and K. Chau, “Acoustic noise radiated by pwm-controllel induction machine drives,” *IEEE Transactions on Industrial Electronics*, vol. 47, no. 4, pp. 880–889, 2000.

[65] A. Binojkumar, B. Saritha, and G. Narayanan, “Acoustic noise characterization of space-vector modulated induction motor drives—an experimental approach,” *IEEE Transactions on Industrial Electronics*, vol. 62, no. 6, pp. 3362–3371, 2014.

[66] J. Roivainen and A. Mäkinen, “Unit-wave response-based computation of magnetic noise of electric machines,” in *IEEE International Conference on Industrial Technology*, pp. 439–444, 2010.

[67] C. Lin and B. Fahimi, “Prediction of acoustic noise in switched reluctance motor drives,” *IEEE Transactions on Energy Conversion*, vol. 29, no. 1, pp. 250–258, 2013.

[68] D. Torregrossa, B. Fahimi, F. Peyraut, and A. Miraoui, "Fast computation of electromagnetic vibrations in electrical machines via field reconstruction method and knowledge of mechanical impulse response," *IEEE Transactions on Industrial Electronics*, vol. 59, no. 2, pp. 839–847, 2011.

[69] M. Chari and P. Silvester, "Finite-element analysis of magnetically saturated dc machines," *IEEE Transactions on Power Apparatus and Systems*, no. 5, pp. 2362–2372, 1971.

[70] H. Li, K. W. Klontz, V. E. Ferrell, and D. Barber, "Thermal models and electrical machine performance improvement using encapsulation material," *IEEE Transactions on Industry Applications*, vol. 53, no. 2, pp. 1063–1069, 2016.

[71] I. Ibrahim, M. Mohammadi, V. Ghorbanian, and D. A. Lowther, "Effect of pulsewidth modulation on electromagnetic noise of interior permanent magnet synchronous motor drives," *IEEE Transactions on Magnetics*, vol. 55, no. 10, pp. 1–5, 2019.

[72] I. Ibrahim, R. Silva, M. Mohammadi, V. Ghorbanian, and D. A. Lowther, "Surrogate-based acoustic noise prediction of electric motors," *IEEE Transactions on Magnetics*, vol. 56, no. 2, pp. 1–4, 2020.

[73] W. Zhu, S. Pekarek, B. Fahimi, and B. J. Deken, "Investigation of force generation in a permanent magnet synchronous machine," *IEEE Transactions on Energy conversion*, vol. 22, no. 3, pp. 557–565, 2007.

[74] J. Besnerais, A. Fasquelle, M. Hecquet, V. Lanfranchi, and P. Brochet, "A fast noise-predictive multiphysical model of the pwm-controlled asynchronous machine," in *17^{th} International Conference on Electrical Machines*, pp. 1–6, 2006.

[75] J. Le Besnerais, V. Lanfranchi, M. Hecquet, and P. Brochet, "Characterization and reduction of audible magnetic noise due to pwm supply in induction machines," *IEEE Transactions on Industrial Electronics*, vol. 57, no. 4, pp. 1288–1295, 2009.

[76] B. Weilharter, O. Biro, H. Lang, G. Ofner, and S. Rainer, "Validation of a comprehensive analytic noise computation method for induction machines," *IEEE Transactions on Industrial Electronics*, vol. 59, no. 5, pp. 2248–2257, 2011.

[77] B. Cassoret, R. Corton, D. Roger, and J.-F. Brudny, "Magnetic noise reduction of induction machines," *IEEE Transactions on power electronics*, vol. 18, no. 2, pp. 570–579, 2003.

[78] J. Le Besnerais, V. Lanfranchi, M. Hecquet, G. Lemaire, E. Augis, and P. Brochet, "Characterization and reduction of magnetic noise due to saturation in induction machines," *IEEE Transactions on Magnetics*, vol. 45, no. 4, pp. 2003–2008, 2009.

[79] A. Tan-Kim, V. Lanfranchi, S. Vivier, J. Legranger, and F. Palleschi, "Vibro-acoustic simulation and optimization of a claw-pole alternator," *IEEE Transactions on Industry Applications*, vol. 52, no. 5, pp. 3878–3885, 2016.

[80] Siemens PLM Software Inc., *NX Nastran.* Siemens PLM Software Inc., 2018.

[81] D. Kim, G. Jang, and J. Nam, "Magnetically induced vibrations in an ipm motor due to distorted magnetic forces arising from flux weakening control," *IEEE transactions on magnetics*, vol. 49, no. 7, pp. 3929–3932, 2013.

[82] A. Tan-Kim, V. Lanfranchi, J. Legranger, F. Palleschi, and M. Redon, "Influence of temperature on the vibro-acoustic behavior of claw-pole alternators," in *IEEE International Conference on Electrical Machines*, pp. 1628–1634, 2014.

[83] S. Zuo, F. Lin, and X. Wu, "Noise analysis, calculation, and reduction of external rotor permanent-magnet synchronous motor," *IEEE Transactions on Industrial Electronics*, vol. 62, no. 10, pp. 6204–6212, 2015.

[84] M. Hombu, S. Ueda, A. Ueda, and Y. Matsuda, "A new current source gto inverter with sinusoidal output voltage and current," *IEEE Transactions on Industry Applications*, no. 5, pp. 1192–1198, 1985.

[85] Y. Fang and T. Zhang, "Vibroacoustic characterization of a permanent magnet synchronous motor powertrain for electric vehicles," *IEEE Transactions on Energy Conversion*, vol. 33, no. 1, pp. 272–280, 2017.

[86] Z. Zhu, L. Xu, and D. Howe, "Influence of mounting and coupling on the natural frequencies and acoustic noise radiated by a pwm controlled induction machine," 1999.

[87] http://www.compem.ece.mcgill.ca.

[88] S. N. Ali, A. Hanif, and Q. Ahmed, "Review in thermal effects on the performance of electric motors," in *2016 International Conference on Intelligent Systems Engineering*, pp. 83–88, 2016.

[89] J. Le Besnerais, V. Lanfranchi, M. Hecquet, and P. Brochet, "Multiobjective optimization of induction machines including mixed variables and noise minimization," *IEEE Transactions on Magnetics*, vol. 44, no. 6, pp. 1102–1105, 2008.

[90] F. Jurecka, *Robust design optimization based on metamodeling techniques.* PhD thesis, Technische Universität München, 2007.

[91] M. Valavi, A. Nysveen, and R. Nilssen, “Magnetic forces and vibration in permanent magnet machines with non-overlapping concentrated windings: A review,” in *2012 IEEE International Conference on Industrial Technology*, pp. 977–984, 2012.

[92] J. D. Ede, Z. Zhu, and D. Howe, “Rotor resonances of high-speed permanent-magnet brushless machines,” *IEEE Transactions on Industry Applications*, vol. 38, no. 6, pp. 1542–1548, 2002.

[93] X. Guo, Y. Yang, and X. Wang, “Optimal space vector modulation of current-source converter for dc-link current ripple reduction,” *IEEE Transactions on Industrial Electronics*, vol. 66, no. 3, pp. 1671–1680, 2018.

[94] N. Mohan, T. M. Undeland, and W. P. Robbins, *Power electronics: converters, applications, and design.* John Wiley & Sons, 2003.

[95] V. Ghorbanian and D. A. Lowther, “A statistical solution to efficiently optimize the design of an inverter-fed permanent-magnet motor,” *IEEE Transactions on Industry Applications*, vol. 53, no. 6, pp. 5315–5326, 2017.

[96] M. Mohammadi, V. Ghorbanian, and D. Lowther, “A data-driven approach for design knowledge extraction of synchronous reluctance machines using multi-physical analysis,” in *13th International Conference on Electrical Machines*, pp. 479–485, 2018.

[97] M. Mohammadi, T. Rahman, R. Silva, B. Wang, K. Chang, and D. Lowther, “Effect of acoustic noise on optimal SynRM design regions,” *IEEE Transactions on Magnetics*, vol. 54, no. 3, pp. 1–4, 2017.

[98] S. Watanabe, S. Kenjo, K. Ide, F. Sato, and M. Yamamoto, “Natural frequencies and vibration behavior of motor stators,” *IEEE Transactions on Power Apparatus and Systems*, vol. 102, no. 4, pp. 949–956, 1983.

[99] N. Bracikowski, M. Hecquet, P. Brochet, and S. V. Shirinskii, “Multiphysics modeling of a permanent magnet synchronous machine by using lumped models,” *IEEE Transactions on Industrial Electronics*, vol. 59, no. 6, pp. 2426–2437, 2011.

[100] V. Ghorbanian, S. Hussain, S. Hamidizadeh, R. Chromik, and D. Lowther, “Demagnetization proximity considerations of inverter-fed permanent magnet motors,” in *2017 IEEE International Electric Machines and Drives Conference*, pp. 1–7, 2017.

[101] S. Ruoho and A. Arkkio, “Partial demagnetization of permanent magnets in electrical machines caused by an inclined field,” *IEEE Transactions on Magnetics*, vol. 44, no. 7, pp. 1773–1778, 2008.

[102] V. Ghorbanian, M. H. Mohammadi, I. Ibrahim, D. A. Lowther, and J. Hendershot, "An hpc-based data-driven process for design exploration and optimization of motor drives," in *IEEE International Electric Machines & Drives Conference*, pp. 597–602, 2019.

[103] B. Wang, T. Rahman, K. Chang, M. H. Mohammadi, and D. A. Lowther, "A neural network based surrogate model for predicting noise in synchronous reluctance motors," in *2016 IEEE Conference on Electromagnetic Field Computation*, pp. 1–1, 2016.

[104] M. Redhead, "Models in physics," *The British Journal for the Philosophy of Science*, vol. 31, no. 2, pp. 145–163, 1980.

[105] M. Amrhein and P. T. Krein, "Magnetic equivalent circuit modeling of induction machines design-oriented approach with extension to 3-d," in *IEEE International Electric Machines & Drives Conference*, vol. 2, pp. 1557–1563, 2007.

[106] R. H. Myers, D. C. Montgomery, and C. M. Anderson-Cook, "Response surface methodology: Process and product optimization using designed experiments, john wiley& sons," *Inc., New York, NY*, pp. 134–174, 1995.

[107] J. P. Kleijnen, "Simulation and optimization in production planning: a case study," *Decision Support Systems*, vol. 9, no. 3, pp. 269–280, 1993.

[108] B. Yu and K. Popplewell, "Metamodels in manufacturing: a review," *The International Journal of Production Research*, vol. 32, no. 4, pp. 787–796, 1994.

[109] A. Forrester, A. Sobester, and A. Keane, *Engineering design via surrogate modelling: a practical guide.* John Wiley & Sons, 2008.

[110] D. S. Broomhead and D. Lowe, "Radial basis functions, multi-variable functional interpolation and adaptive networks," tech. rep., Royal Signals and Radar Establishment, Malvern (United Kingdom), 1988.

[111] L. Lebensztajn, C. A. R. Marretto, M. C. Costa, and J.-L. Coulomb, "Kriging: A useful tool for electromagnetic device optimization," *IEEE Transactions on Magnetics*, vol. 40, no. 2, pp. 1196–1199, 2004.

[112] Y. Jin, "A comprehensive survey of fitness approximation in evolutionary computation," *Soft computing*, vol. 9, no. 1, pp. 3–12, 2005.

[113] M. Papadrakakis, N. D. Lagaros, and Y. Tsompanakis, "Structural optimization using evolution strategies and neural networks," *Computer methods in applied mechanics and engineering*, vol. 156, no. 1-4, pp. 309–333, 1998.

[114] M. H. Mendes, G. L. Soares, J.-L. Coulomb, and J. A. Vasconcelos, "A surrogate genetic programming based model to facilitate robust multi-objective optimization: A case study in magnetostatics," *IEEE Transactions on Magnetics*, vol. 49, no. 5, pp. 2065–2068, 2013.

[115] J. H. Friedman, "Multivariate adaptive regression splines," *The annals of statistics*, pp. 1–67, 1991.

[116] W.-Y. Loh, "Regression tress with unbiased variable selection and interaction detection," *Statistica sinica*, pp. 361–386, 2002.

[117] T. Chai and R. R. Draxler, "Root mean square error (rmse) or mean absolute error (mae)?–arguments against avoiding rmse in the literature," *Geoscientific model development*, vol. 7, no. 3, pp. 1247–1250, 2014.

[118] C. J. Willmott and K. Matsuura, "Advantages of the mean absolute error (mae) over the root mean square error (rmse) in assessing average model performance," *Climate research*, vol. 30, no. 1, pp. 79–82, 2005.

[119] N. J. Nagelkerke *et al.*, "A note on a general definition of the coefficient of determination," *Biometrika*, vol. 78, no. 3, pp. 691–692, 1991.

[120] C. Cortes and V. Vapnik, "Support-vector networks," *Machine learning*, vol. 20, no. 3, pp. 273–297, 1995.

[121] D. Meyer and F. T. Wien, "Support vector machines," *The Interface to libsvm in package e1071*, vol. 28, 2015.

[122] I. Ibrahim, R. Silva, M. Mohammadi, V. Ghorbanian, and D. A. Lowther, "Surrogate models for design and optimization of inverter-fed synchronous motor drives," *IEEE Transactions on Magnetics*, vol. 57, no. 6, pp. 1–5, 2021.

[123] I. Ibrahim and D. A. Lowther, "Effects of stator laminations on acoustic noise of electrical machines," in *2021 IEEE Energy Conversion Congress and Exposition (ECCE)*, pp. 3902–3908, IEEE, 2021.

[124] D. Warfield, "The study of hearing in animals," *Methods of animal experimentation, IV*, pp. 43–143, 2012.

[125] A. Peterson and E. Gross, *Handbook of Noise Measurement.* 7th ed. Concord, MA: General ny, 1972.

[126] J. P. Cowan, *Handbook of Environmental Acoustics.* John Wiley & Sons, Inc., 1994.

[127] M. E. El-Hawary, *Principles of electric machines with power electronics applications.* John Wiley & Sons Inc., 2002.

[128] K. Chau, C. C. Chan, and C. Liu, "Overview of permanent-magnet brushless drives for electric and hybrid electric vehicles," *IEEE Transactions on Industrial Electronics*, vol. 55, no. 6, pp. 2246–2257, 2008.

[129] S. Nasar, "DC-switched reluctance motor," in *Proceedings of the institution of electrical engineers*, vol. 116, pp. 1048–1049, 1969.

[130] A. Hughes and B. Drury, *Electric motors and drives: fundamentals, types and applications.* Newnes, 2019.

[131] S. Huang, M. Aydin, and T. A. Lipo, "Electromagnetic vibration and noise assessment for surface mounted pm machines," in *Power Engineering Society Summer Meeting*, vol. 3, pp. 1417–1426, 2001.

[132] H. Jordan and H. Frohne, "Determination of resonance frequencies of stators of polyphase motors," *Larmbekampfung*, vol. 1, pp. 137–140, 1957.

[133] P. L. Alger, *The nature of induction machines.* Gordon and Breach, 1965.

[134] F. Carter, "Magnetic noise in dynamo-electric machines," *Engineering*, vol. 134, pp. 548–581, 1932.

[135] A. Ellison and C. Moore, "Calculation of acoustic power radiated by short electric machines," *Acta Acustica united with Acustica*, vol. 21, no. 1, pp. 10–15, 1969.

[136] D. Wu, S. D. Pekarek, and B. Fahimi, "A field reconstruction technique for efficient modeling of the fields and forces within induction machines," *IEEE Transactions on Energy Conversion*, vol. 24, no. 2, pp. 366–374, 2009.

[137] M. Fakam, M. Hecquet, V. Lanfranchi, and A. Randria, "Design and magnetic noise reduction of the surface permanent magnet synchronous machine using complex air-gap permeance," *IEEE Transactions on Magnetics*, vol. 51, no. 4, pp. 1–9, 2015.

[138] J. Dong, J. W. Jiang, B. Howey, H. Li, B. Bilgin, and A. Emadi, "Hybrid acoustic noise analysis approach of conventional and mutually coupled switched reluctance motors," *IEEE Transactions on Energy Conversion*, vol. 32, no. 3, pp. 1042–1051, 2017.

[139] P. Krause, O. Wasynczuk, and S. D. Pekarek, *Electromechanical motion devices*, vol. 90. John Wiley & Sons, 2012.

[140] M. H. Mohammadi and D. A. Lowther, “A computational study of efficiency map calculation for synchronous ac motor drives including cross-coupling and saturation effects,” *IEEE Transactions on Magnetics*, vol. 53, no. 6, pp. 1–4, 2017.

[141] B. K. Bose *et al.*, *Modern power electronics and AC drives*, vol. 123. Prentice hall Upper Saddle River, NJ, 2002.

[142] S. Hussain, V. Ghorbanian, A. Benabou, S. Clénet, and D. A. Lowther, “A study of the effects of temperature on magnetic and copper losses in electrical machines,” in *22nd International Conference on Electrical Machines*, pp. 1277–1283, 2016.